Development of a silicon pixel tracker for the measurement of the differential charm cross section of 400 GeV/c proton collisions on a SHiP-like thick target

DISSERTATION
zur Erlangung des Grades eines Doktors
der Naturwissenschaften

vorgelegt von
Nikolaus G. G. Owtscharenko
aus Hamburg

Eingereicht bei der Naturwissenschaftlich-Technischen Fakultät
der Universität Siegen

2023

Betreuer und erster Gutachter: Prof. Dr. Markus Cristinziani
Zweiter Gutachter: Prof. Dr. Markus Risse
Tag der mündlichen Prüfung: 24.08.2023

Abstract

The Search for Hidden Particles (SHiP) experiment is proposed to search for weakly interacting particles in a beam-dump setup with a 400 GeV proton beam of unprecedented intensity at the CERN SPS. An important parameter in modeling signal and background is the charm production cross section in the SHiP target, which is not known with sufficient precision and has in fact never been measured for cascade production.

The SHiP−charm experiment is designed to measure the charm cross section in a thick target, where cascade production dominates. The experiment is proposed for the same SPS beam as SHiP. The experiment has a moving target, instrumented with nuclear emulsions for direct observation of production and decay of charmed hadrons, followed by a spectrometer. It is crucial for the experiment to timestamp tracks and vertices in the nuclear emulsion for accurate event reconstruction.

Within the scope of this work, a pixel tracker, placed directly downstream of the target as part of the spectrometer, has been built and operated in an optimisation testbeam for SHiP−charm. As first electronic detector in the setup the pixel tracker is connecting observed tracks and vertices in the emulsion with electronic, timestamped events in the spectrometer. The detector setup is presented, the performance of the pixel tracker is discussed, and the matching of pixel tracker events with tracks and vertices detected in the emulsion target is presented in this thesis.

Zusammenfassung

Die SHiP-Kollaboration schlägt ein Beam-Dump Experiment mit dem 400 GeV Protonenstrahl des CERN SPS vor. Mit bisher unerreichter Intensität soll das SHiP-Experiment nach extrem schwach wechselwirkenden Teilchen suchen. Ein wichtiger Parameter zur Modellierung von Signal und Hintergrund dieser Messung ist der Wirkungsquerschnitt für die Produktion von Charm Quarks im SHiP-Target. Dieser Wirkungsquerschnitt ist bisher nur mit unzureichender Genauigkeit bekannt und wurde darüber hinaus für die Kaskadenproduktion von Charm Quarks noch nie gemessen.

Für die Messung dieses Wikungsquerschnittes in Kaskadenproduktion wurde das SHiP–charm-Experiment entworfen. Das Experiment wird für den gleichen SPS Protonenstrahl vorgeschlagen wie SHiP und verfügt über ein dickes Target in dem die Kaskadenproduktion von Charm Quarks dominiert. Das Target in SHiP−charm bewegt sich durch den Protonenstrahl und ist mit Kernemulsionsplatten ausgestattet, die eine direkte Beobachtung von Produktion und Zerfall der Hadronen mit Charm Quarks ermöglichen. Dieses Target wird durch ein Spektrometer ergänzt. Für das Experiment ist es von entscheidender Bedeutung, die Teilchenspuren und Interaktionsvertices in der Emulsion den Ereignissen im Spektrometer zeitlich und räumlich zuzuordnen.

Im Rahmen dieser Arbeit wurde ein Pixeldetektor zur Spurrekonstruktion als Teil des Spektrometers direkt hinter dem Target gebaut und in einem Vorexperiment zur Integration der verschiedenen Detektoren von SHiP−charm betrieben. Als erster elektronischer Detektor des Spektrometeraufbaus verbindet der Pixeldetektor die beobachteten Teilchenspuren und Interaktionsvertices in der Emulsion mit den elektronisch aufgezeichneten Ereignissen des Spektrometers. In dieser Arbeit werden Aufbau und Funktionsprinzip des Pixeldetektors erklärt, die Betriebseigenschaften des Detektors diskutiert und die Zuordnung der Ereignisse im Pixeldetektor zu den Teilchenspuren und Interaktionsvertices in der Emulsion vorgestellt.

Contents

1 Introduction

Particle physics aims to explain the workings of nature, from microscopic phenomena up to astrophysical observations in our universe. The Standard Model of elementary particle physics (SM) describes the electromagnetic, the weak and the strong force. With the Higgs mechanism even the origin of elementary particle masses is explained in the SM. One decade after the discovery of the Higgs boson and after an even longer period of extensive testing, the SM is very successful, and also very precise in describing our universe.

The SM, however, can not explain certain observations and phenomena, e.g. how neutrinos obtain their mass, and why it is so small. Also, the fourth fundamental interaction, gravity, is not part of the SM and the cosmological observations of dark matter and dark energy can not be explained by the SM. Some of the most promising theories explaining these open questions become more and more unlikely with the continuous validation of the SM and the probing of the TeV energy range at the Large Hadron Collider (LHC). The search for dark matter at the LHC multipurpose experiments continues with no candidate so far. Alternative access to new physics might be provided by feebly interacting particles, with SM cross sections so small, that not even the intensity at the LHC multipurpose experiments is large enough for a significant observation. The Search for Hidden Particles (SHiP) experiment is proposed to search for dark matter candidates at the *intensity frontier* and aims for the collection of 2×10^{20} events in a zero background environment. A long fixed target is used as a beam-dump for the 400 GeV proton beam of the CERN Super Proton Synchrotron (SPS). Without background, SHiP is able to directly detect dark matter by recoil interaction and is theory agnostic, i.e. also new physics which are not proposed yet could be detected by observation of the decay of the associated particles. A more conservative part of the physics programme for SHiP includes the study of tau-neutrinos. The first observation of $\overline{\nu}_\tau$ and precise neutrino interaction measurements are possible with SHiP.

For these measurements, the production of secondary particles in the target has to be understood to a high level of precision. This includes the charm-production cross section. At the centre-of-mass energy in SHiP, charmed interactions dominate the hard and secondary interactions, and also in tau-neutrino production, charmed hadrons play a major role.

Due to the length of the SHiP target, secondary production is expected to dominate the charm-production cross section. This *cascade effect* however has never been measured so far. A dedicated experiment, SHiP−charm, is proposed to measure this cross section as input for SHiP. The SHiP−charm experiment employs an emulsion cloud chamber (ECC) and a spectrometer for event reconstruction. The ECC is able to reconstruct interaction vertices and tracks in unmatched precision, but without electronic readout. It is therefore crucial to connect the information in the ECC with data from the spectrometer.

Within the scope of this work, a pixel tracker was developed and built as first detector in the SHiP−charm spectrometer with the main task of reconstructing tracks leaving the ECC, thus enabling full event reconstruction in the experiment. This work presents results from an optimisation run for SHiP−charm, where $\sim 3\,\%$ of the planned final dataset were taken. The pixel tracker setup is discussed and the performance in the optimisation run is investigated. Track reconstruction resolution and detection efficiency are evaluated and the crucial procedure of connecting tracks in the ECC with the pixel tracker data is presented. Finally, an algorithm developed for vertex reconstruction in pixel tracker data is presented, and reconstructed vertices are evaluated.

2 Physics beyond the Standard Model

Since the finalisation of the current formulation in the 1970s, the SM was very successful in explaining experimental results and in the prediction of interactions and properties of elementary particles. These elementary particles, quarks and leptons, are found in three generations, and are subject to three fundamental forces: the strong, weak, and electromagnetic interactions. The interactions are mediated by *gauge bosons*: gluons, Z^0, $W^{\pm}$ and photon; while gravity, the fourth fundamental force, is not explained in the SM. The discovery of the Higgs boson in 2012 [1; 2] completed the SM. Based on the coupling strengths and the corresponding charges of the elementary particles in the SM, interactions and bound states can be predicted and are confirmed in unprecedented precision by experiments.

There are however observations which can not be explained within the SM, indicating that the SM does not describe the full picture of particle physics. The search for new physics, explaining the inconsistencies, drives the particle physics community today, and is also motivating the SHiP experiment. This chapter gives an introduction to the physics models investigated by SHiP and how these models can consistently extend the SM and explain the above-mentioned observations. The structure follows a comprehensive study on the SHiP physics case [3] as well as the benchmark cases in the Physics Beyond Colliders report [4].

2.1 The Standard Model of elementary particle physics

The SM is a quantum field theory (QFT) based gauge theory, introduced to describe the elementary particles and their interactions. The elementary particles are split into two categories in the SM: Twelve spin-$\frac{1}{2}$ particles, called fermions, which constitute matter, and three types of spin-1 particles, bosons, which mediate the three interactions.

An overview of the elementary particles is shown in Figure 2.1. Based on whether the fermions carry colour charge, i.e. are receptive to the strong interaction, they are categorised in quarks and leptons. All fermions are susceptive to the weak interaction, the charged leptons and the quarks also interact electromagnetically. The fermions are separated in three generations of significantly different masses, introducing additional flavour quantum numbers with each generation. From these 12 fermions, all matter is built, although the baryonic matter observed in the universe today consists only of fermions from the first generation, namely up- and down quarks as valence quarks of protons and neutrons, which, together with electrons, form atoms.

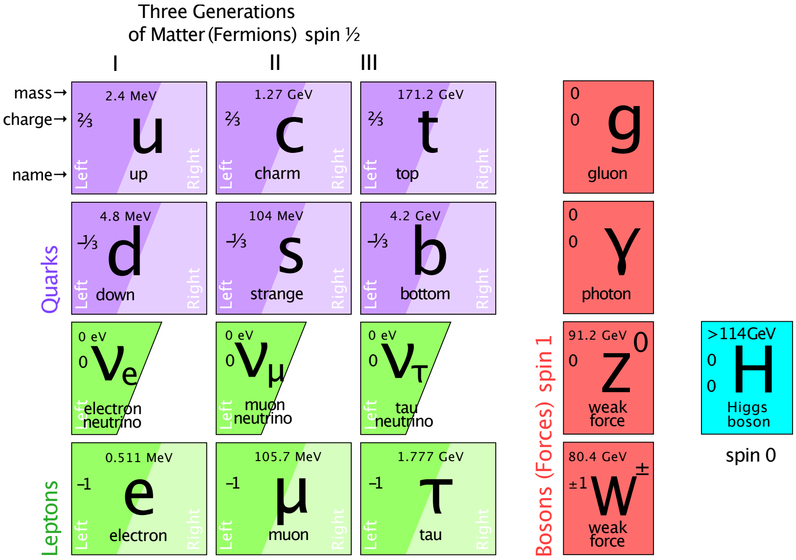

Figure 2.1: Particle content of the SM. Left are the fermions in three generations of quarks and leptons. The neutrinos are the only exclusively left-handed fermions. On the right are the bosons mediating the fundamental interactions, and the Higgs boson [5, p. 2].

The fundamental interactions are mediated by gauge, or vector bosons of spin 1: γ for the electromagnetic, $W^{\pm}$ and Z for the weak, and eight gluons of different colour charges for the strong interaction. Finally, the Higgs boson with spin 0 is added by the Brout-Englert-Higgs (BEH) mechanism [6–8], which describes the generation of elementary particle masses, except the masses of neutrinos, by coupling of the particles to the BEH field.

2.1.1 Gauge theories of fundamental interaction

The three fundamental interactions in the SM can be described by a Lagrangian field density $\mathcal{L}$ each, requiring local gauge invariance. Each interaction follows a different gauge symmetry, as is briefly discussed in the following. Numerous detailed discussions and derivations of the theories are available in literature. This section is written with reference to [9–11].

The electromagnetic interaction is described by a $U(1)$ symmetry, and the corresponding Lagrangian is [12, p. 78]:

$$\begin{aligned} \mathcal{L}_{\mathrm{QED}} &= \overline{\psi}(i\gamma^{\mu}D_{\mu} - m)\psi - \frac{1}{4}F^{\mu\nu}F_{\mu\nu}, \text{ with} \\ F_{\mu\nu} &= \partial_{\mu}A_{\nu} - \partial_{\nu}A_{\mu} \ . \end{aligned} \tag{2.1}$$

Here $D_{\mu} = \partial_{\mu} - igA_{\mu}$ is the gauge covariant derivative with the coupling strength $g = e$. F is the electromagnetic field tensor with the corresponding field A, and ψ is the fermion field, here representing any charged fermion. To explain the experimentally observed parity violation in weak interactions [13; 14], chirality, i.e. the distinction between left-handed and right-handed fermion fields was introduced [15; 16]:

$$\begin{aligned} \psi_{\mathrm{L}} &= \frac{1}{2}(1 - \gamma^{5})\psi \ , \\ \psi_{\mathrm{R}} &= \frac{1}{2}(1 + \gamma^{5})\psi \ . \end{aligned} \tag{2.2}$$

By convention, left-handed fields correspond to particles and right-handed fields to antiparticles. With chirality as a particle feature, it is possible to formulate a unified *electroweak theory* [17–19]. While the electromagnetic interaction is invariant to chirality, and the $U(1)$ transformation remains unchanged, the weak interaction only couples to left-handed particles and right-handed antiparticles, introducing an $SU(2)$ group [10, p. 415 ff.]:

$$\begin{aligned} \psi_{\mathrm{L/R}} &\xrightarrow{U(1)} e^{i\alpha(x)\frac{Y}{2}}\psi_{\mathrm{L/R}} \ , \\ \psi_{\mathrm{L}} &\xrightarrow{SU(2)} e^{i\beta(x)\frac{\sigma_i}{2}}\psi_{\mathrm{L}} \ , \end{aligned} \tag{2.3}$$

with hypercharge Y and Pauli matrices σ_i with $i = 1, 2, 3$. The combination of the two gauge groups $U(1)_Y \times SU(2)_{\mathrm{L}}$ produces four gauge fields, and the Lagrangian for electroweak interaction can be expressed as follows [20, p. 1]:

$$\begin{aligned} \mathcal{L}_{\mathrm{EW}} &= \overline{\psi}(i\gamma^{\mu}D_{\mu} - m)\psi - \frac{1}{4}W_i^{\mu\nu}W^i_{\mu\nu} - \frac{1}{4}B^{\mu\nu}B_{\mu\nu}, \text{ with} \\ W^i_{\mu\nu} &= \partial_{\mu}W^i_{\nu} - \partial_{\nu}W^i_{\mu} - g_{\mathrm{W}}\epsilon^{ijk}W^j_{\mu}W^k_{\nu} \ , \text{ and} \\ B_{\mu\nu} &= \partial_{\mu}B_{\nu} - \partial_{\nu}B_{\mu} \ . \end{aligned} \tag{2.4}$$

The four field tensors $W^i_{\mu\nu}$ and $B_{\mu\nu}$ represent the four gauge fields, and g_{W} is the weak coupling constant and ϵ^{ijk} are structure constants. Moreover, the field tensors $W^i_{\mu\nu}$ contain a self-coupling term.

The electroweak theory described so far can only work with massless particles. Introducing a mass term would break gauge invariance [10, p. 469]. However, the gauge bosons $W^{\pm}$ and Z^0 are massive, as are the observed fermions. This is addressed by the BEH mechanism: Particles obtain mass via interaction with the *Higgs field*, spontaneously breaking the electroweak symmetry. The corresponding Lagrangian writes [11, p. 7]:

$$\begin{aligned}\mathcal{L}_{\text{Higgs}} &= (D_\mu\phi^\dagger)(D^\mu\phi) - V(\phi)\text{, with}\\ \phi &= \begin{pmatrix}\phi^+\\ \phi^0\end{pmatrix}\text{ and}\\ V(\phi) &= \mu^2\phi^\dagger\phi + \lambda(\phi^\dagger\phi)^2 = \mu^2\phi^2 + \lambda\phi^4\,.\end{aligned} \tag{2.5}$$

Here ϕ is a complex scalar field and a doublet of $SU(2)$, $\mu^2 < 0$ and $\lambda > 0$. For $\mu^2 < 0$ $\langle\phi\rangle = 0$ is not a minimum, but an unstable local maximum, the minimum is at $\phi = \left(0, \sqrt{-\frac{\mu^2}{2\lambda}} = \frac{v}{\sqrt{2}}\right)$ [11, p. 7], with the vacuum expectation value v. Occupation of any state in the minimum breaks the electroweak symmetry. Introducing a small perturbation h, such that the field

$$\phi = \frac{1}{\sqrt{2}}\begin{pmatrix}0\\ v+h\end{pmatrix}\,, \tag{2.6}$$

changes the first term of the Lagrangian to [10, 480 ff.]:

$$\mathcal{L}^{\text{kin}}_{\text{Higgs}} = \frac{1}{2}\partial_\mu h\partial^\mu h + \frac{1}{8}(v+h)^2\left(g_{\text{W}}^2\left|W_\mu^{(1,2)}\right|^2 + (g_{\text{W}}W_\mu^{(3)} - gB_\mu)^2\right)\,. \tag{2.7}$$

The massive electroweak gauge bosons can be written as mixed states [11, p. 9]

$$W^{\pm} = \frac{1}{\sqrt{2}}(W_\mu^{(1)} \mp iW_\mu^{(2)}) \tag{2.8}$$

for the $W^{\pm}$ bosons, and

$$\begin{pmatrix}Z_\mu\\ A_\mu\end{pmatrix} = \begin{pmatrix}-\sin\theta_{\text{W}} & \cos\theta_{\text{W}}\\ \cos\theta_{\text{W}} & \sin\theta_{\text{W}}\end{pmatrix}\begin{pmatrix}B_\mu\\ W_\mu^{(3)}\end{pmatrix} \tag{2.9}$$

for the Z boson and the photon (A). θ_{W} is the Weinberg angle [17, p. 584], and $g_{\text{W}} = \frac{g}{\tan\theta_{\text{W}}}$. The masses of the W and Z bosons are related to v:

$$m_{\text{W}} = \frac{g_{\text{W}}v}{2}\quad,\quad m_{\text{Z}} = \frac{v}{2}\sqrt{g^2 + g_{\text{W}}^2}\,. \tag{2.10}$$

Since B_μ only couples to ϕ^+, the photon is massless [10, p. 482; 11, p. 9]. The fermions obtain mass due to Yukawa couplings with the Higgs field. The Lagrangian for the first generation of fermions computes to [11, p. 9; 21, p. 19]:

$$\mathcal{L}_{\text{Yukawa}} = -\frac{v+h}{\sqrt{2}} \left(\overline{\ell}_{\text{L}} \lambda_\ell \ell_{\text{R}} + \overline{u}_{\text{L}} \lambda_u u_{\text{R}} + \overline{d}_{\text{L}} \lambda_d d_{\text{R}}\right) + h.c., \tag{2.11}$$

where the subscripts L and R stand for the chirality: left-handed fields are $SU(2)$ doublets and right-handed fields are singlets. Leptons, and up and down quarks, are represented by ℓ, u, d, and $\lambda_{\ell,u,d}$ are the respective coupling constants. The mass of fermions is hence created by coupling of both, left- and right-handed states to the Higgs field. The single fermion terms in the Lagrangian $\overline{\psi} m \psi$ (with $\psi = \ell, u, d$) are also known as *Dirac masses*. With the introduction of the other fermion generations the scalar representations become matrices and mixing of quarks has to be considered, described by the CKM matrix [22]. The neutrino does not have electromagnetic charge and only interacts weakly, thus there is no right-handed neutrino state, leaving the neutrino without mass in the SM.

The SM is completed by quantum chromodynamics (QCD), describing the strong interaction between quarks and gluons, the latter being the QCD gauge boson. Colour-charged particles are confined to states of colour-neutral hadrons by the strong force. Each quark has one of three colours, hence the theory follows an $SU(3)$ gauge symmetry. The gluons are colour-charged themselves, thus they are able to self interact [23]. The Lagrangian for the strong interaction can be written as [24, p. 5]:

$$\begin{aligned} \mathcal{L}_{\text{QCD}} &= \overline{\psi}(i\gamma^\mu D_\mu - m)\psi - \frac{1}{4} G^{\text{A}}_{\mu\nu} G^{\mu\nu}_{\text{A}}, \text{with} \\ G^{\mu\nu}_{\text{A}} &= \partial_\mu G^\nu_{\text{A}} - \partial_\nu G^\mu_{\text{A}} - g_{\text{s}} \epsilon^{ijk} G^\mu_j G^\nu_k \ . \end{aligned} \tag{2.12}$$

Similar to the other formulations, $G^{\mu\nu}$ is the field tensor for the gluon, with the self-interaction term containing the structure constants ϵ^{ijk}, and g_{s} is the coupling constant of the strong interaction. Combining the three Lagrangians of fundamental interactions, the SM is described by a gauge theory G_{SM}:

$$G_{\text{SM}} = U(1) \times SU(2) \times SU(3) \ . \tag{2.13}$$

2.2 Observations inconsistent with the Standard Model

After the discovery of the Higgs boson, no strong evidence of new physics beyond the SM was found at the LHC, despite intensive probing of the available phase space. In fact, the absence of new physics suggests the SM to hold up to energies $\sim 10^5$ TeV, well beyond the electroweak scale: The measured values for the Higgs mass and the top-quark mass are found to be at a magnitude where no new particles are required for consistency of the

SM, possibly up to the Planck scale [25, p. 31; 4, p. 4; 26]. While these findings are in agreement with the SM, observations in astrophysics and cosmology can currently not be explained within this theory, especially:

Dark matter and dark energy

The cosmological standard model, known as the Λ_{CDM} model, supported by measurements of the cosmic microwave background [27], predicts around 27 % of the total energy in the universe to be present in the form of dark matter, matter which today is measured indirectly, by its gravitational deformation of spacetime [28, p. 387, 389; 29, p. 5] as well as its influence on galaxy dynamics [30].

Besides dark matter, an even larger fraction of the total energy in the universe does not have gravitational effects, but seems to influence the universe and its expansion as a whole. Due to lack of a more accurate description, it is called dark energy, making up around 68 % of the energy in the universe [31, p. 16]. This leaves only approximately 5 % for baryonic matter, making up the directly observable universe.

The SM has no candidates for dark-matter particles, that could explain either of the observed, opening the floor for new theories yet to be confirmed by experiments.

Neutrino masses

In the SM the three neutrinos are massless. However, the observation of neutrino oscillations shows that neutrinos have non-zero mass. Neutrino masses are however very small. Recently an upper bound for the mass of the electron neutrino of $m_\nu < 0.8\,\mathrm{eV}/c^2$ was established by KATRIN in a direct measurement [32].

In the simplest approach to explain neutrino masses it is possible to introduce a Dirac mass term for neutrinos to the SM, similar to the other fermions [10, p. 494]. This would however require the existence of right-handed neutrinos. Also, a Dirac mass would not explain the large difference in the masses of the neutrinos compared to other fermions. In another model, under the assumption that neutrinos are their own antiparticles, i.e. *Majorana particles* [33], a Majorana-mass term is introduced:

$$\mathcal{L}_{\mathrm{M}} = \frac{1}{2} M \left(\overline{\nu}^{c}_{\mathrm{R}} \nu_{\mathrm{R}} + \overline{\nu}_{\mathrm{R}} \nu^{c}_{\mathrm{R}} \right) \,, \tag{2.14}$$

where ν^c is the charge conjugated neutrino, and $\nu^{c}_{\mathrm{R}} = \nu_{\mathrm{L}}$ corresponds to the left-handed antineutrino [10, p. 495]. Majorana neutrinos, however, violate lepton number conservation. In an approach to integrate both models, the *seesaw mechanism* was developed [34–36], which computes the Lagrangian for neutrino masses to [10, 495 ff.]:

$$\mathcal{L}_{\text{seesaw}} = -\frac{1}{2}\begin{pmatrix}\overline{\nu}_{\text{L}} & \overline{\nu}^{c}_{\text{R}}\end{pmatrix}\begin{pmatrix}0 & m_{\text{D}} \\ m_{\text{D}} & M\end{pmatrix}\begin{pmatrix}\nu^{c}_{\text{L}} \\ \nu_{\text{R}}\end{pmatrix} + h.c. \tag{2.15}$$

Here m_{D} is the Dirac mass and M is the Majorana mass. The neutrino masses m_ν are the eigenvalues of the mass matrix in Equation (2.15) and assuming $M \gg m_{\text{D}}$:

$$\begin{aligned} m_{\pm} &\approx \frac{1}{2}M \pm \frac{1}{2}\left(M + \frac{2m_{\text{D}}^2}{M}\right), \text{ with} \\ |m_\nu| &\approx \frac{m_{\text{D}}^2}{M} \quad \text{and} \quad m_N \approx M\ . \end{aligned} \tag{2.16}$$

Thus, two mass states are predicted for every neutrino generation, the light state m_ν which is observed, and a much heavier state m_N. With a Dirac mass m_{D} of $\mathcal{O}(1\,\text{GeV})$, similar to other fermion masses, and $M \gg m_{\text{D}}$, the observed m_ν could be explained. The two masses are inversely proportional to each other, hence the name seesaw mechanism.

So far, neither the Dirac nor the Majorana model could be verified, and the origin of neutrino masses remains unclear. Furthermore, the magnitude and hierarchy of the neutrino masses is subject of current research, favouring normal hierarchy and mass splittings $\Delta m_{ij}^2 = m_i^2 - m_j^2$ around $7.4 \times 10^{-5}\,\text{eV}^2/c^4$ for Δm_{21}^2 and around $2.43 \times 10^{-3}\,\text{eV}^2/c^4$ for Δm_{32}^2 [37, p. 303].

Baryon asymmetry of the universe

The state-of-the-art model in cosmology is the Big Bang model, where matter and anti-matter were produced in equal amount. In the universe, however, only baryonic matter is observed. Consequently, an asymmetry during the cooling of the universe after the Big Bang had to produce more matter than anti-matter, leading to the observed quantity of matter. This observation is generally referred to as baryon asymmetry of the universe (BAU). Any theory explaining the BAU has to meet the Sakharov conditions [38]:

- Baryon number violation;
- CP violation;
- interaction out of thermal equilibrium.

A baryon number violation can be motivated within some grand unifying theories and even within the SM, although only for extreme cases and in rates not sufficient for the observed asymmetry. CP violation is also observed in SM decays, however, the observed rate of violation is orders of magnitude too small to explain BAU. Finally, the thermal equilibrium criterion states that the rate at which any reaction generates a baryon-asymmetry needs to be lower than the expansion rate of the universe, inhibiting pair-annihilation [39, p. 46]. Baryogenesis could also be explained by leptogenesis in a neutrino minimal Standard Model (νMSM), introducing right-handed neutrinos (see Section 2.3.3).

Altogether, the SM's inadequate description of the universe led to the development of numerous models addressing the shortcomings, forming the field of physics beyond the Standard Model (BSM). So far though, no significant deviation from the SM, explaining any BSM physics model, could be observed.

2.3 Hidden sector portals

The missing observation of BSM physics can have two possible reasons: The new physics to be discovered could be mediated by particles heavier than the TeV energy scale investigated by the LHC, which would require even higher centre-of-mass energies in collider experiments. This is called the *high-energy frontier*.

Another reason could be, that the new physics is part of a hidden sector (HS), with particles only feebly interacting with SM particles. To discover particles with such exceptionally low couplings, high-intensity sources are necessary. This *high-intensity frontier*, can be explored in beam-dump experiments, where the number of interactions is maximised, and ultra-rare processes can be investigated. The SHiP experiment is trying to push the high-intensity frontier.

If the HS particles couple to the SM, new Lagrangian terms need to be introduced [4, p. 8], also referred to as portals:

$$\mathcal{L}_{portal} = \sum O_{SM} \times O_{HS} \ . \tag{2.17}$$

Here, O_{SM} is an operator composed of the SM fields, and O_{HS} the operator composed of HS fields. Any possible portal operator involves the SM fields by definition and thus needs to result in gauge invariant Lagrangian terms, limiting the number of possible terms. In the following, portals with renormalisable interactions and small dimensionless coupling constants are introduced, as these are considered promising in the physics beyond colliders community [3; 4; 40]. Another promising portal is provided by axions and axion-like particles (ALPs), discussed in Section 2.3.4. Every portal presented respects all the SM gauge symmetries.

Portal	**Interaction term**
vector (dark photon)	$\frac{\epsilon}{2}F'_{\mu\nu}F^{\mu\nu}$
scalar (dark Higgs)	$(\alpha_1 S + \alpha S^2)H^\dagger H$
HNL (neutrino)	$H^\dagger N\overline{L}$
pseudo-scalar (axion)	$aF^{\mu\nu}\widetilde{F}^{\mu\nu}$

Table 2.1: Couplings of possible HS portals to the SM. The single terms are introduced in the following sections.

2.3.1 Vector portal

For the vector portal, a U(1) gauge group in addition to the existing U(1) × SU(2) × SU(3) gauge symmetry of the SM is proposed. Experiments at the LHC on the high-energy frontier have placed strong bounds on possible new vector states, excluding masses in the TeV range [41; 42]. However, the (sub)GeV range is only poorly constrained by the ATLAS and CMS experiments. A minimal interaction with a light but massive new vector particle can be written as

$$\mathcal{L} = \mathcal{L}_{\text{SM}} - \frac{1}{4}F'_{\mu\nu}F'^{\mu\nu} + \frac{\epsilon}{2}F'_{\mu\nu}F^{\mu\nu} + \frac{m^2_{\gamma'}}{2}A'_\mu A'^\mu \ , \tag{2.18}$$

analogously to the photon in quantum electrodynamics [43, p. 3]. The factor ϵ is the coupling strength of the new vector particle (gauge boson) A' to the electromagnetic current, and is assumed to be rather small. Furthermore, $F'_{\mu\nu} = \partial_\mu A'_\nu - \partial_\nu A'_\mu$ is the field strength tensor. The coupling to the electromagnetic current suggests the name *dark photon* for the proposed gauge boson. Of the numerous scenarios for BSM physics with a dark photon, three are shortly introduced here, following the physics beyond colliders report [4]:

> **Minimal dark photon:** A single state A' is predicted, and the dark photon decays to SM particles, since the dark matter is either too heavy, or in a different sector.
>
> **Light dark matter candidate coupled to dark photon:** The dark photon A' predominantly decays to light dark matter states $\chi\chi^*$ of feebly interacting particles or WIMPs[1] [44]. The dark matter states could scatter on electrons and nuclei due to the coupling to the electromagnetic current according to ϵ.

---

[1] WIMPs is short for "weakly interacting massive particles" which does not necessarily refer to the weak force.

Millicharged particles: For the case of $m_{A'} \to 0$ the dark matter state χ has an effective electrical charge $|Q_\chi| = |\epsilon e|$. A possible interaction for this scenario is shown in Figure 2.2.

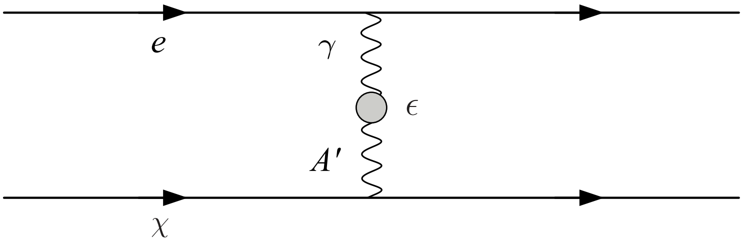

Figure 2.2: Scattering of a dark matter candidate off a SM electron. In the limit $m_{\mathrm{A}'} \to 0$, the charge Q_χ is proportional to ϵe. Adapted from [3].

With high-intensity experiments using a proton beam on a fixed target, the three dominant production processes for dark photons are:

Meson decays: A proton beam-dump experiment produces mesons in abundance. The most important contribution to the vector portal is provided by the process $\pi^0 \to \gamma A$, suppressed by the coupling ϵ^2. Contribution from η^0 should also be considered, while the vector mesons can be neglected due to the rater small branching ratios for production [45, p. 3]. This channel is open for $m_{A'} \leq 0.9\,\mathrm{GeV}/c^2$ [46, p. 3].

Proton bremsstrahlung: Incident protons scatter quasi-elastically on nucleons in the target, and vector states can be produced via bremsstrahlung: $pN \to p'NA'$ with N being a nucleon [47]. Dark photon production via bremsstrahlung is relevant for $m_{A'} \leq 2\,\mathrm{GeV}/c^2$ but heavily suppressed for $m_{A'} > m_p$ [46, p. 3].

Direct QCD production: For higher masses of the dark photon ($m_{A'} \gtrsim 1\,\mathrm{GeV}/c^2$) direct partonic production is the dominant process [40, p. 6]. Dark photons are produced via $q\bar{q} \to A'$. For higher orders of perturbation also partonic final states $qg \to qA'$ are possible [43, p. 6]. The direct production is relevant for dark photon masses $1.4 < m_{A'} < 10\,\mathrm{GeV}/c^2$ [46, p. 6].

In addition to hadronic interactions and despite lower rates, decays of dark photons via lepton-induced processes should also be considered, since this could play a role in scenarios where new physics does not couple to coloured particles [48].

2.3.2 Scalar portal

With the discovery of the Higgs boson the existence of scalar bosons was proven, motivating searches for a scalar boson coupling to the HS, referred to as *dark Higgs*. A minimal scalar portal is realised by a heavy scalar singlet S, coupling to the SM via the Higgs field H:

$$\mathcal{L} = \mathcal{L}_{\text{SM}} + \frac{1}{2}\partial_\mu S \partial^\mu S + (\alpha_1 S + \alpha S^2)(H^\dagger H) + \lambda_2 S^2 + \lambda_3 S^3 + \lambda_4 S^4 \,, \tag{2.19}$$

where the portal couplings α_1 and α mediate between the HS and the SM and $\lambda_{2,3,4}$ are the self couplings of the dark Higgs [3, p. 17]. Two scenarios for a scalar portal to the HS are distinguished in literature:

> **Higgs-scalar mixing:** The new scalar S mixes with the Higgs boson, breaking electroweak symmetry. In this case, S can couple to all SM states except neutrinos, including linear mixing between S and the Higgs. In this model a vacuum expectation value for S can be developed: Assuming $m_S \ll m_h$ and a small α_1, the mixing angle
>
> $$g_* = \sin\theta \simeq \theta \simeq \frac{\alpha_1 v^2}{m_h^2}, \tag{2.20}$$
>
> with $v = 246\,\text{GeV}$ the electroweak vacuum expectation value and the Higgs mass m_h [3, p. 21]. Production and decay of S would be the same as for the Higgs boson of a mass m_S. In other words, production and decay of the hidden scalar are suppressed by a factor g_* compared to the Higgs boson.
>
> **$\mathcal{Z}_2$ symmetry with pair production:** If the coupling $\alpha_1 = 0$ and the scalar S does not mix with the Higgs, electroweak symmetry is not broken and thus no vacuum expectation value for the dark Higgs is developed. In this model the Higgs boson is a heavy mediator and decays to pairs of low mass HS states, as in $h \to SS$, $B \to K^{(*)}SS$ or $B^0 \to SS$ [49; 4, p. 10]. The pair-production scenario is a minimal *hidden-valley* scenario, where one or more long-lived particles of low mass and zero charge (and spin or parity) are predicted in the MeV range up to a few GeV [3, p. 18].

In a beam-dump experiment like SHiP, for an off-shell Higgs, the dominant production mechanism for S are meson decays like

$$B \to S + K, \qquad K \to S + \pi, \qquad D \to S + \pi,$$

as illustrated in Figure 2.3. The most interesting channel is the B decay, since D decay is strongly suppressed [50, p. 1], and Kaons are stopped in the SHiP target (see Section 3.1.2). If the Higgs is on-shell, the direct production $h \to SS$ dominates [51].

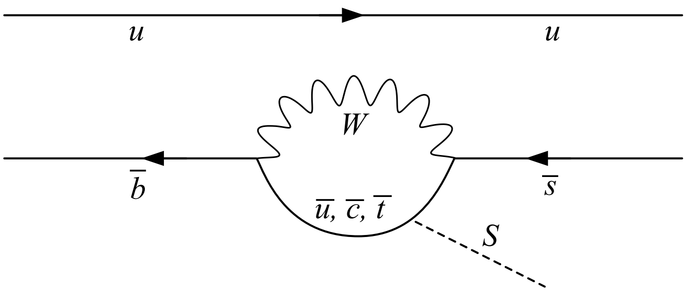

Figure 2.3: Penguin diagram for $B \to K + S$. The dark scalar S is radiated off in the flavour changing process. Adapted from [52, p. 6]

Depending on the mass, different decay channels are possible for S. If $2m_{\mathrm{e}} < m_{\mathrm{S}} < 2m_{\pi}$ lepton pairs e^+e^- or $\mu^+\mu^-$ are produced. For $m_{\mathrm{S}} > 2m_{\pi}$ also hadronic states $\pi^+\pi^-$, K^+K^- are possible. An overview of the branching ratios is plotted in Figure 2.4. The ratios are almost exclusive up to $m_S \approx 1\,\mathrm{GeV}/c^2$, while in the hadronic regime from $2.5\,\mathrm{GeV}/c^2$ on, several decays compete. The appearance of numerous hadronic resonances around $2\,\mathrm{GeV}/c^2$ makes calculation of single branching ratios difficult, hence the gap.

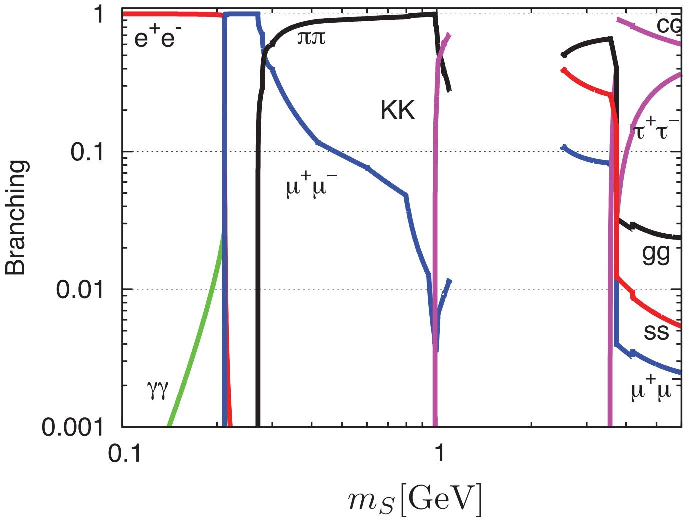

Figure 2.4: Decay branching ratio as a function of m_S, from [3, p. 22]. Below $1\,\mathrm{GeV}/c^2$ the branching is rather exclusive. Around $2\,\mathrm{GeV}/c^2$ many hadronic resonances appear, making calculation of single branching ratios complex, thus the section is omitted. In the hadronic regime no distinct decay is dominant.

2.3.3 Heavy neutral lepton portal

It is possible to formulate a SM extension with one or more dark fermions N, also called heavy neutral leptons (HNLs), to allow coupling with neutrinos, giving it the name *neutrino portal.* The Lagrangian with the neutrino portal computes to [3, p. 39]:

$$\mathcal{L} = \mathcal{L}_{\text{SM}} + i\overline{N}_I \partial N_I - F_{\alpha I}(\overline{L}_\alpha H) N_I - \frac{M_I}{2} \overline{N}_I^c N_I - h.c. \tag{2.21}$$

Here

- N is the HNL field,
- the index I counts the number of HNLs,
- $F_{\alpha I}$ is the Yukawa coupling matrix with $\alpha = e, \mu, \tau$,
- H is the Higgs field, thus $F_{\alpha I} H$ realises Dirac masses of the HNLs,
- L_α are the left-handed SM neutrinos,
- and M_I are the Majorana masses.

The HNLs are also called *sterile neutrinos* since the proposed particles are missing any SM charge. Also, any HNL has to be exclusively right-handed, in order to couple to the SM sector.

The neutrino portal is interesting since it introduces a mass generation formalism, explaining neutrino oscillation. However, depending on whether the HNL mass (and also the SM neutrino mass) is of *Dirac* ($F_{\alpha I} H \neq 0$) or *Majorana* ($M_I \neq 0$) type, there are different models [53]. Models with Majorana mass neutrinos are often preferred over Dirac type neutrinos, since Dirac neutrinos would be realised by the same mass coupling as the other fermions, without an explanation for the large mass difference [37, p. 286].

A complete SM extension, explaining neutrino oscillation is provided by the νMSM [53]. Three additional right-handed HNLs N_1, N_2, N_3 are introduced, according to the three generations of SM neutrinos. Assuming the Dirac masses $M^{\text{D}}_{I,\alpha} \ll M_I$, the seesaw mechanism [34–36] can be applied and the *flavour eigenstates* of neutrinos are different from the *mass eigenstates* [3, p. 39]. In the νMSM the Majorana mass is smaller than the electroweak scale and the Yukawa coupling constants

$$f_I^2 \sim \mathcal{O}(m_\nu M_I)/v^2 \ , \tag{2.22}$$

with the SM neutrino mass m_ν and the vacuum expectation value v of the Higgs field, enforces very weak Yukawa couplings f_I, in the order of 5×10^{-8} to 6×10^{-13} [54, p. 19].

Bounds on the HNL masses can be derived from cosmology. Observation of the cosmic microwave background restricts the lightest sterile neutrino to a few keV [53, p. 153], and the successful nucleosynthesis after the Big Bang requires $M_{2,3} > 1\,\mathrm{GeV}$ for the second and third HNL generation [54, p. 19].

The νMSM could explain the baryon asymmetry of the universe [55], massive neutrinos, and, with a stable N_1, provide a dark-matter candidate at the same time.

At a beam-dump experiment like SHiP, HNL production is possible in 2-body (lepton and HNL) or 3-body (lepton, HNL, light pseudoscalar or vector meson) meson decays as depicted in Figure 2.5. The HNL would be detected indirectly by its decay due to mixing with SM neutrinos. The final state would either be a lepton–anti-lepton pair with a SM neutrino, or contain a meson ($\pi^\pm, K^\pm$), a lepton ($\mu^\pm, e^\pm$) and possibly a neutrino [3, p. 51].

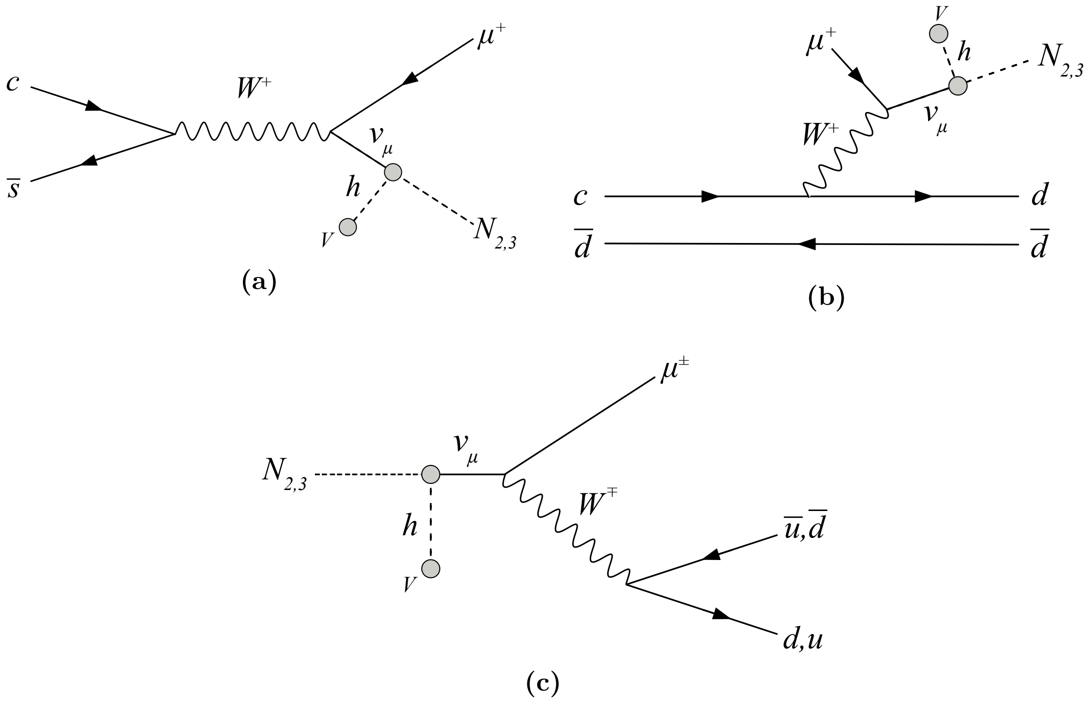

Figure 2.5: Production and decay of HNLs. A D_s meson decays to lepton and neutrino (a), the neutrino is mixing with the HNL, coupling to the Higgs with vacuum expectation value V. The 3-body production (b) is similar, with an additional π^0 produced in the D meson decay. In the decay (c) the HNL mixes with a neutrino which subsequently decays to $\pi^\pm$ and $\mu^\pm$. Also, a 3-body decay $N_{2,3} \to \mu\, e\, \nu$ is possible. Adapted from [56, p. 5; 57]

2.3.4 Axion portal

To describe what is known as the $U(1)_a$ problem in QCD [58], the Lagrangian has to be extended by a phase term $\mathcal{L}_\theta$ which introduces spontaneous symmetry breaking [59]. The SM QCD Lagrangian in Equation (2.12) is then extended to [60, p. 6]:

$$\mathcal{L}_{\mathrm{QCD}} = \sum_n \overline{q}_n(i\gamma^\mu D_\mu - m_n)q_n - \frac{1}{4}G^a_{\mu\nu}G^{\mu\nu}_a + \underbrace{\theta\frac{g^2}{32\pi^2}G^a_{\mu\nu}\tilde{G}^{\mu\nu}_a}_{\mathcal{L}_\theta} . \tag{2.23}$$

Where

- q_n are the quark fields for the flavours n,
- m_n are the quark masses,
- the gauge covariant derivative D_μ couples gluons and quarks,
- γ^μ are the Dirac matrices,
- G is the gluon field strength tensor and a indexes the colours,
- $\theta = \theta_{QCD} + \theta_{weak}$ is a free phase parameter, known as the vacuum angle.

The phase term introduces CP violation to QCD, which is, up to now, not observed experimentally. The theory for example predicts an electric dipole moment of the neutron $d_n \neq 0$, measurements however could not confirm a d_n different from zero [61, p. 5]. A CP invariance of QCD would require $\theta = 0$ or to be very small, although there is no natural reason for such a small θ. This is known as the strong CP problem.

The strong CP problem has three possible solutions: One of the quarks could have a mass compatible with 0, the vacuum angle $\theta \approx 0$, or the vacuum angle is replaced by a dynamic and CP-conserving field [60, p. 6].

The masses of all quarks are observed to be different from zero, and a $\theta = 0$ is incompatible with CP violation in weak interactions. The field introduced by the Peccei-Quinn mechanism [62], known as axion [63], however is a possible solution. The axion term for the Lagrangian is [60, p. 8]

$$\mathcal{L}_a = \xi\frac{a}{f_a}\frac{g_s^2}{32\pi^2}G^b_{\mu\nu}\tilde{G}^{\mu\nu}_b . \tag{2.24}$$

Here ξ is a free parameter, g is the coupling constant of strong interaction and a the axion field with

$$\langle a \rangle = -\frac{f_a}{\xi}\theta . \tag{2.25}$$

The axion acquires mass which is bound to its coupling strength f_a:

$$m_a^2 = -\frac{\xi}{f_a}\frac{g_s^2}{32\pi^2}\frac{\partial}{\partial a}\langle G^b_{\mu\nu}\tilde{G}^{\mu\nu}_b\rangle\Big|_{\langle a\rangle = -\theta f_a/\xi} . \tag{2.26}$$

The axion would couple to the SM via gauge-boson interaction, either with two photons, or with two gluons. The respective couplings $g_{a\gamma}, g_{a\mathrm{G}}$ are however suppressed by f_a. This *visible axion* is predicted with a $f_a = v_{\mathrm{F}} \approx 250\,\mathrm{GeV}$ and was ruled out in experiments [60, p. 12].

The Peccei-Quinn mechanism can be modified to models of *invisible axions* with very large scaling f_a, containing lepton and nucleon coupling [64, p. 200]. The mass for invisible axions is limited to sub eV values from cosmological observations and due to the d_n measurements [65, p. 408; 60, p. 14 ff].

Furthermore, models with less restricted masses (up to the GeV range) for the new particle were introduced [65, p. 407 ff. 4, p. 11]. The different models are from here on summarised as axion-like particles (ALPs). The ALPs share two properties:

Small coupling: The interaction with SM particles is strongly suppressed by the coupling f_a,

Small mass: The ALP mass is small in a sense that it is inversely proportional to the coupling $m_a \sim \Lambda^2/f_a$, with Λ the scale of spontaneous symmetry breaking.

With new states $\mathcal{L}_{\mathrm{HS}}$ in the HS that provide UV completion, a Lagrangian coupling ALPs to the SM can be written as follows [4, p. 11]:

$$\mathcal{L} = \mathcal{L}_{\mathrm{SM}} + \mathcal{L}_{\mathrm{HS}} + \frac{1}{4}g_{a\gamma}F_{\mu\nu}\overline{F}_{\mu\nu} + \frac{1}{4}g_{a\mathrm{G}}\mathrm{Tr}G_{\mu\nu}\overline{G}_{\mu\nu} + \partial_\mu g_{a\mathrm{l}}\sum_\alpha \bar{l}_\alpha\gamma_\mu\gamma_5 l_\alpha + \partial_\mu g_{a\mathrm{q}}\sum_\beta \overline{q}_\beta\gamma_\mu\gamma_5 q_\beta , \tag{2.27}$$

with the couplings $g_{\mathrm{ai}} \propto \frac{a}{f_i}$, where ALPs mediate between dark matter and SM states. The first term describes the di-photon coupling, the second term the coupling to two gluons and the last two terms formulate the fermion coupling of the ALP.

At a beam-dump experiment, production of ALPs is dominated by di-photon coupling via the Primakoff effect [66], see Figure 2.6. The two gauge bosons mediating the scattering of a proton and a target nucleus convert to an ALP which is emitted with a very small transverse momentum, close to the beam direction. The ALP decay is again dominated by the photon channel, $a \to \gamma\gamma$, with a decay time proportional to the axion mass: $\tau \propto \frac{1}{m_a g_{\gamma a}}$. Coupling to fermions would be observed in a signal $a \to \mu^+\mu^-$ [67, p. 20].

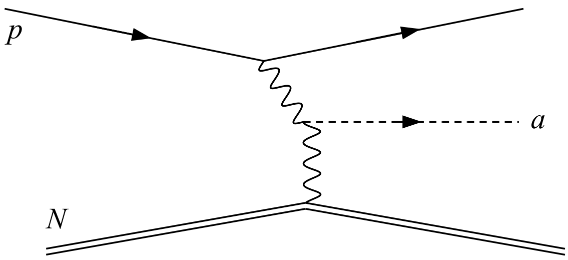

Figure 2.6: Primakoff production of an ALP in a beam-dump experiment. The incoming proton p scatters off a nucleus N. Two photons mediating the scattering process are converted to an axion with small transverse momentum. Adapted from [67, p. 6].

2.4 High-energy neutrino physics

The neutrinos observed differ fundamentally from the ones in the SM. Neutrino oscillations introduce lepton flavour violation, which is not observed for charged leptons, as well as neutrino mass eigenstates which are mixing to the observed flavour eigenstates, as described by the PNMS matrix [68; 69], extending the SM. Thus, neutrinos open a window to BSM physics and studying neutrino properties has become more and more interesting.

Only subject to weak interaction, neutrinos are not deflected in magnetic fields and only scarcely absorbed or scattered, hence rarely detected. In general, two neutrino origins are distinguished: Man-made neutrinos from reactors, accelerators and beam or target interactions with energies up to the GeV range, and cosmic neutrinos with energies up to the PeV range (or higher). While cosmic ultra-high energy neutrinos are important in multi-messenger astronomy, and can also probe energy ranges not accessible otherwise, intensity and distribution of man-made neutrinos can be controlled by the experiment.

Man-made neutrinos are therefore an important instrument to investigate BSM physics, and the production rates at high intensity beam-dump experiments, like SHiP, offer new possibilities to study neutrinos of all three flavours in unprecedented accuracy and up to energies of several hundred GeV.

2.4.1 Tau-neutrino cross section

While the other two neutrino flavours, ν_e and ν_μ, were first observed long ago [70; 71] and are since subject of research, the first observation of the tau neutrino, ν_τ, was made in 2000 by the DONuT experiment with 9 observed events and a background of 1.5 events [72]. DONuT however could not distinguish ν_τ from $\overline{\nu}_\tau$. Years later, Super–Kamiokande observed 338 ± 75 tau-neutrino events, also without distinguishing between ν_τ and $\overline{\nu}_\tau$ [73, p. 12].

Both experiments report cross-section measurements for charged current (CC) ν_τ interactions with large uncertainties. DONuT measured the constant slope σ_{const} of the cross section [72, p. 18], to be multiplied with the particle energy, with a statistical and systematic uncertainty of 33 % each, while Super–Kamiokande measured a flux-averaged cross section for low-energy tau neutrinos with 22 % uncertainty, not compatible with the expected value [73, p. 14]. The OPERA experiment observed and identified 10 ν_τ and is the first experiment to measure the ν_τ cross section in a lead target, although with 50 % uncertainty [74, p. 5].

Altogether, the knowledge about the tau neutrino is scarce and larger datasets with identification of ν_τ and $\overline{\nu}_\tau$ are necessary to measure individual cross sections and learn about tau-neutrino physics.

In an experiment like SHiP, tau-neutrino production is dominated by D_{s} meson decays, as shown in Figure 2.7, with a branching fraction $BR(D_{\mathrm{s}}^{\pm} \to \tau^{\pm}\nu_\tau) = 0.0532 \pm 0.0011$ [37, p. 50]. The $\tau^{\pm}$ again decays to a $\overline{\nu}_\tau$ or ν_τ, and in total the decay chain $D_{\mathrm{s}} \to \tau + \nu_\tau \to \nu_\tau \overline{\nu}_\tau X$ delivers two tau neutrinos, with an equal number of neutrinos and antineutrinos.

Given the similar masses $m_D = 1.968\,\mathrm{GeV}/c^2$ and $m_\tau = 1.777\,\mathrm{GeV}/c^2$, the directly produced (anti-) neutrino is typically less energetic than the second one [75, p. 12; 3, p. 94]. In addition to the branching ratio, the tau neutrino flux for a proton beam-dump experiment depends on the charm quark fragmentation function f_D for $c \to D_{\mathrm{s}}$, and on the charm-production cross section, which is only known with large uncertainty and for thin absorbers (see Section 4.1).

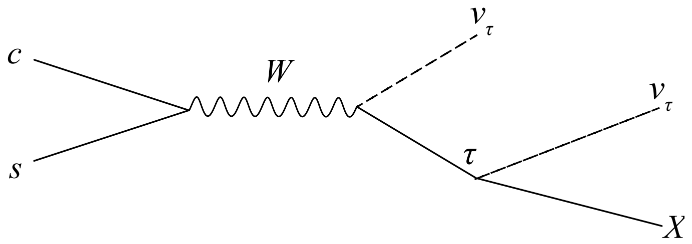

Figure 2.7: Feynman diagram for $D_{\mathrm{s}}^{\pm}$ decay with two neutrinos in the final state. One of the neutrinos is an anti neutrino. Adapted from [3, p. 95].

Assuming 2×10^{20} primary protons and given the centre-of-mass energy $\sqrt{s} \simeq 27.4\,\mathrm{GeV}$ (see Section 3.1.1), a total flux of 5.7×10^{15} $\nu_\tau + \overline{\nu}_\tau$ with a total uncertainty of $\sim 20\,\%$ is predicted for the SHiP experiment, thereof 1.8×10^{15} tau neutrinos of energies $E_\nu \geq 4\,\mathrm{GeV}$ [3, p. 97].

The number of observed tau neutrinos is expected to be large enough for precise physics [76, 21 ff.]. The individual cross sections for ν_τ and $\overline{\nu}_\tau$ can thus be measured (assuming a precise knowledge of the flux), and the neutrino-nucleon charged-current deep-inelastic scattering (CCDIS) will be measured in a dedicated detector (see Section 3.2.1). Knowledge of the neutrino flux is essential for the tau-neutrino cross-section measurement since only a fraction of neutrinos will interact with the detector, reducing the observed number of neutrinos considerably. A crucial input parameter for flux predictions is the number of produced $D_\mathrm{s}^{\pm}$, and hence the charm-production cross section in the target.

Finally, the limit on the tau neutrino magnetic moment is expected to be improved, probing the Dirac nature of neutrinos [3, p. 107].

2.4.2 Neutrino-induced charm production

The first charmed-hadron production in high-energy neutrino interaction was observed by an opposite-sign two-muon final state [77]. It was established since, that high-energy neutrino interactions produce charmed hadrons in the order of a few percent. In a beam-dump experiment this production happens via CCDIS, enabling exclusive charm studies [78, p. 229]. In Figure 2.8 a Feynman diagram for charm production via neutrino-nucleon CCDIS is shown. While electron (anti-) neutrinos scattering would also allow for charmed-hadron production, such events were never observed [79, p. 190]. For ν_μ scattering the Cabibbo matrix clearly favours $s \to c$ conversion, while $d \to c$ is suppressed. Being a valence quark, however, d contributes with $\approx 50\,\%$ to charmed-hadron production. The case for $\overline{\nu}_\mu$ is different. As both, $\overline{s}$ and $\overline{d}$ are sea quarks, the $\overline{s} \to \overline{c}$ conversion dominates with approximately $90\,\%$ [80, p. 191]. Thus, the production of $\overline{c}$ is sensitive to the anti-strange quark content of the nucleon. The strangeness of the nucleon is an important parameter for SM and BSM physics at the LHC [79, p. 190], an example being precise measurements of the W mass.

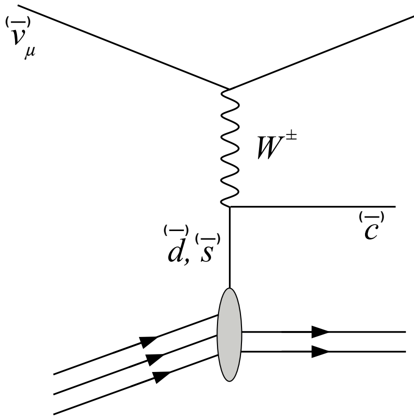

Figure 2.8: Charm production induced by neutrino-nucleon DIS. In c production the s quark is favoured in the Cabibbo matrix, but, being a valence quark, d contributes equally. $\overline{c}$ production is dominated by $\overline{s}$ since both antiquarks are sea quarks. Adapted from [81, p. 144].

The charm quark produced in neutrino-nucleon CCDIS can also be a handle to investigate pentaquarks. Production and detection of the anti-charmed Θ_c^0 pentaquark state in a beam-dump experiment were investigated earlier [82] and seem more promising since the observation of the hidden-charm pentaquark states in LHCb [83].

3 The SHiP experiment

The portals to the HS presented in Section 2.3 show a very weak coupling to the SM. This low interaction probability manifests not only in rare production of hidden particles but also inhibits direct or indirect detection. Consequently, for a statistically significant observation, large numbers of hidden particles have to be produced. Furthermore, the coupling of portals to SM particles complicates identification of a HS signal. The final states of all portals presented are at the same time possible final states for SM interactions. Thus, an experiment to search for the HS must establish a zero background environment, to distinguish HS from SM final states.

SHiP is such a proposed experiment. SHiP is a general-purpose beam-dump experiment to push the high-intensity frontier at the CERN SPS, and sensitive to generic models of feebly interacting particles in an energy range not accessible by other experiments [76].

In the original proposal, a dedicated beam line with a new target complex and an experimental hall was planned for SHiP and the associated beam-dump facility (BDF) [79; 84]. A setup at the ECN3 area is now proposed, with only little impact on the designs of BDF and the experiment [76]. The experimental facility is of twofold structure: First, a BDF with beam extraction, target and shielding, and second the SHiP detector, optimised for HS particle decays and neutrino physics. Both elements are introduced in this chapter with a focus on the features essential for the physics programme.

3.1 Beam-dump facility

The high-energy collider experiments at the LHC aim at a 4π coverage and full event reconstruction. Both goals imply detectors as close to the interaction point as possible. While this is a successful setup for SM event reconstruction, it bears striking disadvantages for HS searches.

Due to the weak interaction with SM matter the detection probability is vanishingly low. On the other hand, the expected decay lengths of portal mediators to SM particles are longer than the detectors radial extent, making the parameter space of HS particles practically inaccessible to collider experiments. Thus, to be sensitive to HS particle decays

or interactions a different setup is necessary.
The beam-dump configuration of SHiP is optimised towards production and direct detection of HS events. The target maximises heavy-hadron production and a long decay spectrometer ensures decay of HS particles in the observable volume. An overview of the experimental complex is shown in Figure 3.1. The proton beam enters the target complex from the right; following the target is a hadron absorber, shielding the experiment. Following downstream is an active muon shield for background reduction. The muon shield is followed by the Scattering and Neutrino Detector (SND) with an ECC. Downstream of the SND the Hidden Sector Decay Spectrometer (HSDS) is located. It features a decay volume, surrounded by a background tagger, followed by detectors for particle identification and event reconstruction.

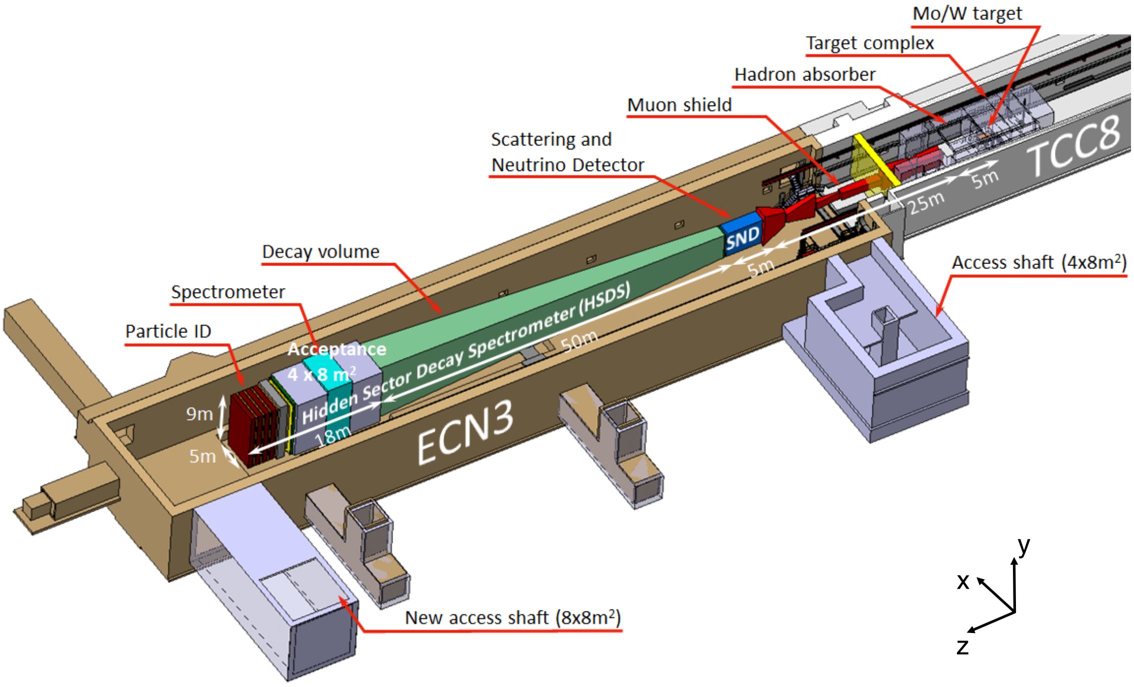

Figure 3.1: Overview of the BDF facility including the SHiP experiment in the existing ECN3 area [76, p. 5]. z follows the beam axis, y points upwards and x forms a right-handed coordinate system with the incident proton beam from the upper right. The target is surrounded by the target complex, followed by the hadron absorber and a dedicated confinement wall to shield the experimental area from the target. The first part of the experiment is a muon shield, followed by the SND and HSDS detectors.

3.1.1 Beam

The facility is proposed for the ECN3 area, a beam line of the SPS where its 400 GeV proton beam is accessible. For SHiP, a total of 2×10^{20} protons on target (PoT) in five years are anticipated, to be delivered by slow extraction in 1 s spills of 4×10^{13} protons with a cycle length of 7.2 s. The slow extraction is chosen to reduce combinatorial background and to stay within the limit of possible beam power deposition in the target [85, p. 7].

As discussed in Sections 2.3 and 2.4, the production of HS states, especially HNLs, and tau neutrinos is mostly associated with charm and bottom hadrons. The 400 GeV proton beam is chosen for the resulting centre-of-mass energy $\sqrt{s} = 27.4\,\text{GeV}$ favouring charm and b-hadron production over lighter quarks. Lower energies are too close to the production threshold for b, and below 25 GeV there is a heavy drop in cross section for charm production (see Section 4.1).

While higher beam energies could be beneficial in terms of the available phase space, such beams are not only hardly available, but the kinematics would result in larger opening angles of the produced particles. To profit from the increased energy, a substantially larger solid angle needs to be covered, drastically increasing detector and decay volume sizes and cost [79, p. 12].

To reduce local maxima of temperature and radiation load in the target, a beam dilution pattern is implemented [86, p. 29]. After iterative optimisation, the beam is now swept in a circular pattern with respect to the x–y plane (the z axis follows the beam). The sweep frequency is 4 Hz and the circle radius is 50 mm [84, p. 116]. The distance between the last active element of the beam line and the target is $\sim 130\,\text{m}$ which is long enough for an effective dilution [76, p. 4].

3.1.2 Proton target

The proton target has to meet several requirements: The beam needs to be fully and safely absorbed by the target, so that no primary particles enter the experiment. At the same time, the charm and beauty hadron production is to be maximised, with as little background for the experiment as possible. Furthermore, the target needs to withstand the extreme thermal and structural loads of the full experiment intensity of 2×10^{20} PoT in five years. These requirements make the target design most challenging, and extensive research and development resulted in an optimised layout with sophisticated cooling and shielding concepts to cope with the high-energy densities and the extreme radiation environment [87–89].

The target layout is shown in Figure 3.2. It is a cylindrical structure of approximately 145 cm length and 25 cm diameter. In the longitudinal direction the target is split in segments of different thicknesses which are interleaved with 5 mm cooling slits. The lengths of single segments have been iteratively adjusted on simulation results to balance physics and lifetime requirements of the target. The physics requirement is to maximise heavy-hadron production while at the same time suppressing the background from muons and especially neutrinos produced in K and π decays. These requirements are best met by a long target of high-Z material with short interaction length for reabsorption of the light mesons before their decay. Tungsten has proven good performance under irradiation and offers high Z and short interaction length and would be an optimal target material [90]. However, in the most stressed part of the target, pure tungsten does not meet the lifetime requirement and is replaced with a Titanium–Zirconium–Molybdenum (TZM) alloy. A high water flow and pressure are necessary for cooling. To inhibit corrosion-erosion, all target segments are clad with a tungsten tantalum alloy Ta2.5W, consisting of tantalum with 2.5 % tungsten [87, p. 3]. In this configuration the target has a nuclear interaction length $\lambda \approx 12$.

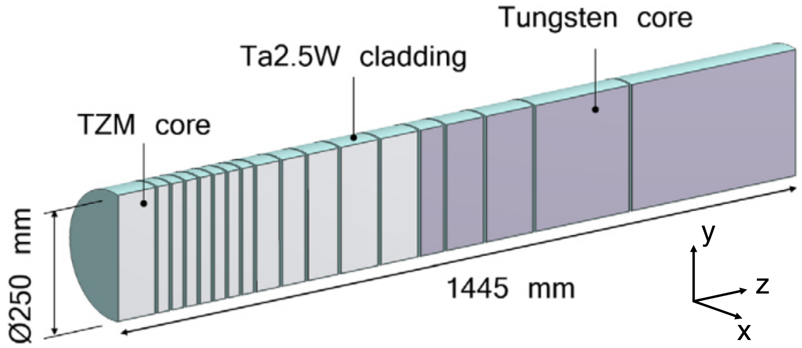

Figure 3.2: Layout of the proton target, with the incident proton beam from the left. The cylindrical target is segmented with cooling slits of 5 mm, to dissipate the thermal load of the beam by water cooling. In the front, a TZM alloy is used, while the second half is from pure Tungsten. From [87, p. 2].

Figure 3.3 shows a simulation of the thermal load in the target after absorption of one spill (~ 1 s). The average power dissipated in the target is 2.56 MW [87, p. 2]. The most energy is deposited in segments 2-8, which consequently are the thinnest segments, to optimise thermal convection. The beam footprint on the target is visible in the temperature distribution. A maximum temperature of 165 °C is reached in the centre of the last TZM segments.

The target is located in a dedicated target complex, optimised towards two objectives: The high levels of prompt and residual radiation make shielding inevitable, therefore proximity shielding blocks of $\sim 5500\,\mathrm{t}$ of cast iron are layered around the target, provided with entry and exit windows of 5 cm steel sheets for the beam and produced particles [84, p. 269].

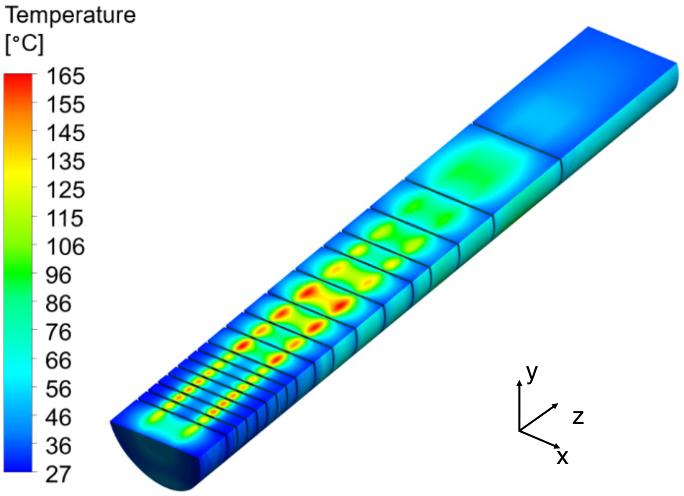

Figure 3.3: Simulated temperature distribution after one spill in the target, the beam follows the z-axis and impinges on the target from the left. The beam dilution pattern is reproduced in the highest temperatures, located where the beam circle hits the target. From [87, p. 11].

The second objective is to reduce background in the experiment, induced by hadrons and electromagnetic radiation. This is achieved by a hadron absorber, placed downstream of the target shielding. The absorber is actively magnetised for more efficient background reduction, and followed by the first part of the muon shield, which is discussed in the following section. For radio-protection, the target complex is hermetically sealed from the experimental area by a confinement wall. A design is shown in Figure A.1 in the Appendix.

3.1.3 Active muon shield

The intense hadronic interaction in the target produces immense amounts of SM final states. In particular after one spill, $\mathcal{O}(10^{11})$ muons above $1\,\mathrm{GeV}/c$ are produced, mainly from K, π, ρ and ω decays in the target and in the following hadron absorber [91, p. 1]. As the detection of HS final states relies on a zero-background environment, the amount of muons entering the detector has to be minimised. The rarely interacting muons are not absorbed, and to reduce the muon flux substantially, magnetic deflection from the fiducial volume of the detector is necessary. A dedicated simulation was performed to gain knowledge about spectrum and flux of muons produced, and it was found that the momentum p ranges from 0 to $350\,\mathrm{GeV}/c$ with a transverse momentum p_T up to $7\,\mathrm{GeV}/c$ [91, Fig. 1]. This large spread in phase space makes the shield design especially challenging. To satisfy the zero background requirement, and for additional background reduction measures (vetoing, track reconstruction, etc.) to work, the initial flux has to be reduced by up to six orders of magnitude. A dedicated measurement of the muon flux was conducted to validate the simulation and further optimise the design [92]. The active muon shield consists of a series of electromagnets and measures about 30 m along the beam axis, as proposed for the dedicated BDF [91, p. 6]. The vertical extent of single magnets can vary from 0.5 to 6 m, while the horizontal extent is approximately half of that. The field strengths range between 1.4 T and 1.7 T.

The basic working principle of the shield is illustrated in Figure 3.4: High energy muons are deflected just outside the fiducial volume, while the deflection radius for lower energy muons is small enough for them to enter the magnets' return fields, sweeping the muons back towards the experiment. Hence, a second deflection is necessary, and the magnetic fields therefore switch polarity halfway down the beam axis.

At the time of writing this thesis the design of the muon shield is being optimised for the ECN3 facility. It will be considerably shorter compared to earlier designs, imposing stronger requirements on the field strength and/or detector systems for vetoing [76, p. 9].

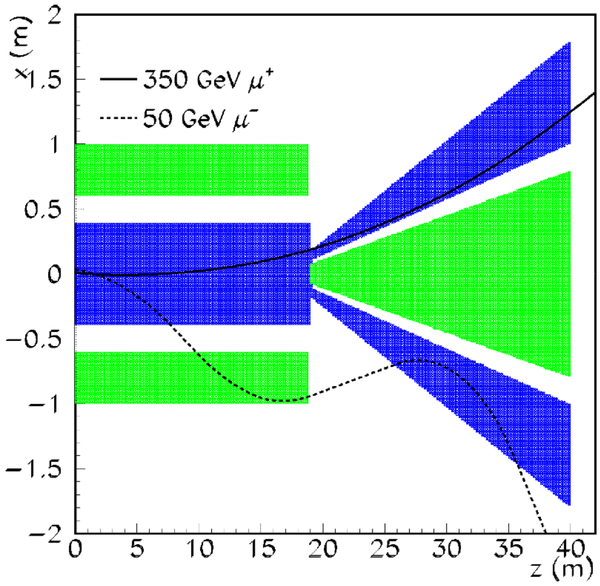

Figure 3.4: Magnetic field polarity in a top view at $y = 0$ to illustrate the deflection principle of the muon shield. The beam impinges from the left. The field is along the y axis, the colours indicate the opposite field polarities with green being the (unwanted) return field. The field strength ranges from 1.4 T to 1.7 T. For high energy muons the deflection is just sufficient, while low energy muons enter the return field and need a second deflection. From [91, p. 3].

3.2 SHiP detectors

The SHiP physics programme is twofold: Detection of long-lived weakly-interacting particles of the HS as well as tau-neutrino physics with the first direct observation of $\overline{\nu}_{\tau}$. These two aspects require different detection approaches best met with a dedicated detector for each measurement. Neutrino detection requires substantial amounts of passive material, which is not expected to impair HS detection capabilities. Furthermore, the low SM coupling of HS particles results in long lifetimes. A HS decay is therefore best detected in a long decay volume distant from the proton target.
A complementary setup is planned for the experiment, with the SND for neutrino physics placed upstream and the active muon shield directly behind. Downstream follows the HSDS with a long decay volume and electronic detectors, as can be seen from Figure 3.1.

3.2.1 Scattering and Neutrino Detector

The full SND setup, as developed for the dedicated BDF facility, is shown in Figure 3.5. A spectrometer is contained in a magnet with a 1.2 T field. Downstream is the muon identification system, build from eight layers of resisitve plate chambers (RPCs) and nine layers of iron filters. The last RPC plane acts as a veto tagger for the following HSDS detector to identify particles produced in the iron filter, marking them as background for the HS search. Together with the other subsystems, the design of the SND is being optimised for the ECN3 setup at the time of writing.

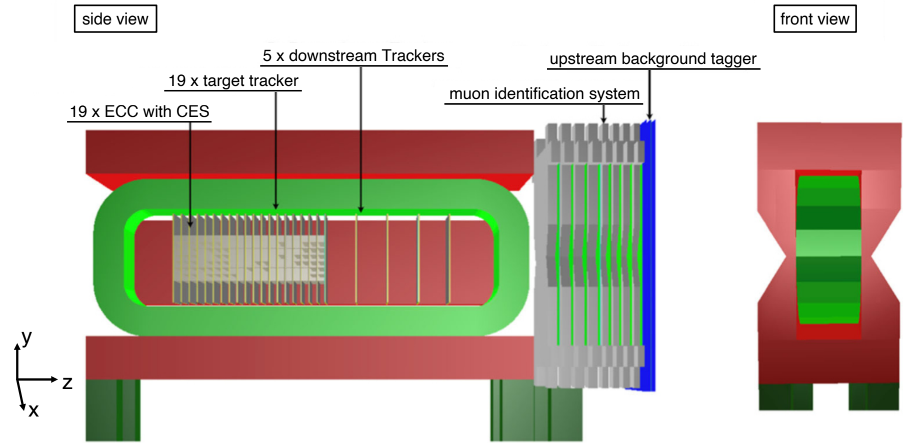

Figure 3.5: Schematic of the SND detector with ECC, CES and SciFi detectors inside the magnet, and muon identification system downstream. Secondary particles from the target impinge from the left. The ECC and CES provide track and vertex reconstruction, particle identification and momentum measurement. The SciFi layers provide each track with a time stamp for electronic event reconstruction. From [93, p. 4]

In the GeV energy regime, neutrinos interact via CC deep-inelastic scattering off nuclei (see Section 2.4). To maximise the interaction probability, a detector needs substantial amounts of material. For tau-neutrino measurements an accuracy in reconstruction of tracks and vertices of $\mathcal{O}(5\,\mu\text{m})$ is required, to resolve the short lifetime of the τ lepton in disentangling production and decay vertices [76, p. 8]. An ECC is able to provide both features by interlacing sheets of passive material and active emulsion in a sandwich-like structure. The SHiP SND consists of 19 layers of ECC bricks with 36 emulsion sheets and 36 tungsten sheets of 1 mm thickness each. The active surface (perpendicular to the beam) is 80 cm × 80 cm per layer [93, p. 4]. A comprehensive discussion on the ECC working principle can be found in Section 4.2.2.

With the ECC technique the three neutrino flavours can be distinguished, based on the different decay vertex topologies of the associated charged lepton. Electrons are identified by the electromagnetic shower, muons by the primary vertex and a signal in the muon detector downstream of the ECC, and tau leptons by the short distance between the production and the decay vertex [79, p. 180 ff]. Each ECC layer is followed by a Compact Emulsion Spectrometer (CES) for momentum measurements as illustrated in Figure 3.6. The CES consists of a volume of low material budget and two emulsion layers. As the whole SND detector is placed in a magnetic field, the sagitta of charged particles can be measured in the CES. The bending radius is proportional to the momentum (see Equation (4.2)), and the direction of deflection depends on the charge polarity.

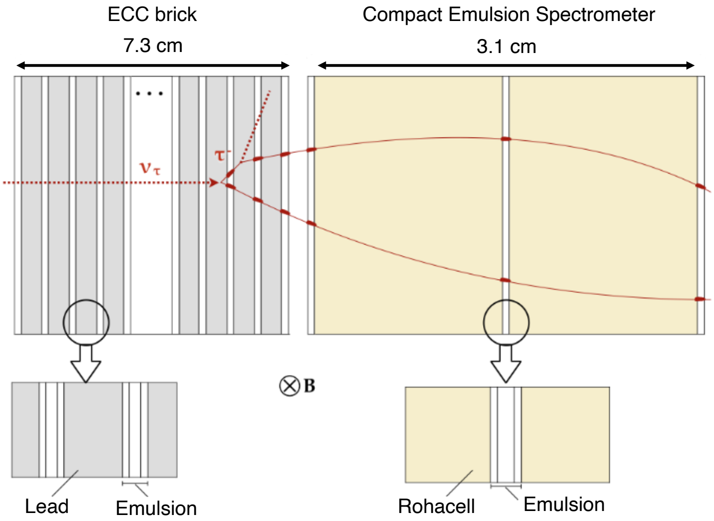

Figure 3.6: Sketch of the ECC and CES layout. Particles produced in the ECC leave the brick and pass a low material-budget volume with two emulsion films to measure the sagitta in the magnetic field. From [94, p. 34].

The high reconstruction accuracy and direct decay observation come with the disadvantage of no electronic event records. To compensate for this, each layer of ECC and CES is followed by a plane of scintillating-fiber (SciFi) detectors, called *target trackers*, for time stamping. An additional target tracker is placed in front of the most upstream ECC layer.

3.2.2 Hidden Sector Decay Spectrometer

The search for HS particle decays to SM final states in the HSDS requires a full event reconstruction, i.e. reconstruction of the decay vertex, reconstruction of the invariant mass of the decayed particle by calorimetric measurement of the final state, and particle identification. The expected rarity of HS events puts special focus on the background. The HSDS can be divided into two parts: The vacuum vessel for background reduction, and the spectrometer for event reconstruction.

The design for the ECN3 area is shown in Figure 3.7. A dedicated vessel is placed downstream of the SND as fiducial decay volume. The structure is $\sim 50\,\mathrm{m}$ long and of pyramidal frustum shape. The length of the vessel is optimised to be sensitive to numerous physics models and resulting particle masses, and the aperture is optimised towards the opening angle of tracks emerging from the proton target.

To identify particles entering from the SND or the associated muon spectrometer the upstream wall of the vessel is instrumented with the upstream background tagger. The tagger is built from two layers of Multigap RPC detectors with $\sim 300\,\mathrm{ps}$ timing resolution. The decay vessel itself is evacuated to minimise neutrino and muon-induced background in the decay volume. The vessel is also completely covered by the surrounding background tagger from liquid scintillator, to identify particles entering the decay volume from outside, or produced by inelastic scattering in the vessel walls.

Downstream of the decay vessel the spectrometer is placed, instrumented with four different detectors and a magnet. The single detectors are briefly introduced in the following:

> **Straw tracker:** To reconstruct the decay vertex and the impact parameter of hidden particles a straw tracker is placed downstream of the decay volume. Four stations of straws build two tracking layers, placed upstream and downstream of a magnet respectively. The homogeneous magnetic field is oriented along the x axis. Each tracking station contains four *views* for unambiguous reconstruction of space points. Two layers with straws along the x-axis for a measurement of the y coordinate, and two layers, tilted by $\pm 5^\circ$ with respect to x, for an x-coordinate measurement. In this setup the straw tracker can measure the momentum of particles, based on the particle deflection (see Equation (4.3)).

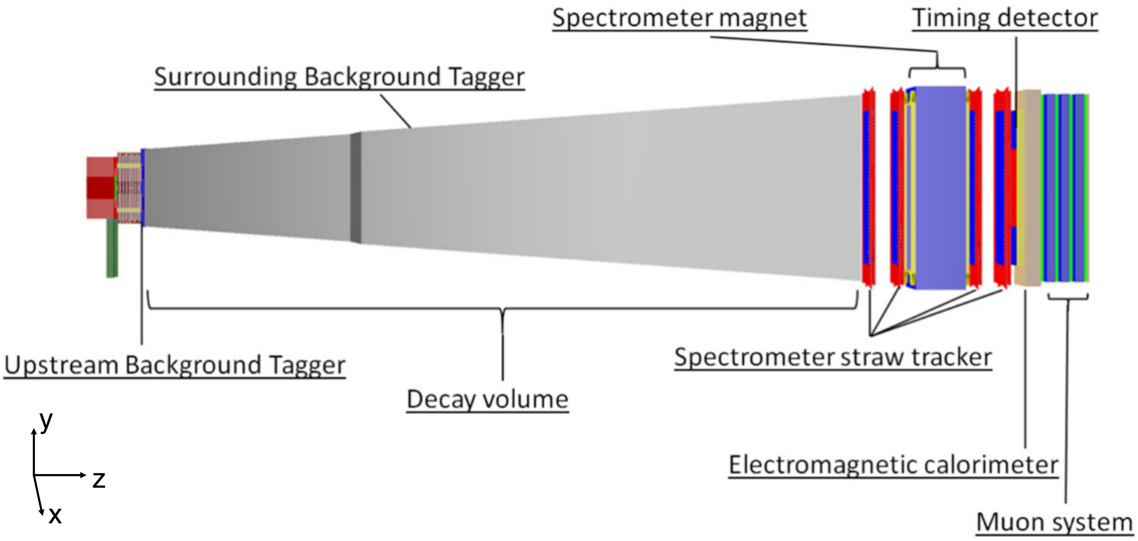

Figure 3.7: Lateral view of the HSDS. Secondary particles from the target impinge from the left. The decay volume is evacuated and surrounded by a background tagger for best possible background suppression. Following are the spectrometer with a straw tracker, the electromagnetic calorimeter and the muon identification system. From [93, p. 8].

Timing detector: Following the straw tracker is a timing layer with a required hit time resolution $< 100\,\mathrm{ps}$ [93, p. 11], placed outside the vacuum vessel. The main purpose of the timing layer is to reject combinatoric events in the decay volume. This is ensured by a coincidence requirement for hits in the timing detector. The registered coincident time is the reference for drift time measurements in the straw tracker [95, p. 35]. There are two options for this detector, plastic scintillating bars and Multigap RPCs, the decision on the technology is part of the ongoing R&D efforts.

Electromagnetic calorimeter: The calorimeter is based on the “SplitCal” concept [96] and built from 40 layers of lead absorbers, interlaced with sampling layers of scintillating plastic. The total sampling depth is 20 X_0. For adequate reconstruction of two-photon final states a resolution for the shower angle of $< 5\,\mathrm{mrad}$ is required. Three sampling layers are equipped with high-resolution detectors to improve angular resolution. The electromagnetic calorimeter aims at identifying electrons and photons, and to discriminate between hadrons and muons [93, p. 12]. A dedicated hadronic calorimeter is not foreseen in the detector design.

Muon system: The muon identification system is the last detector in the experiment, with four stations of scintillating bars and/or tiles, read out by Silicon Photomultipliers. The active layers are interleaved with three iron filters of 60 cm, i.e. 3.4 nuclear interaction lengths λ, each. Together with the calorimeter the total material budget is $\sim 17\,\lambda$ [93, p. 13].

3.2.3 Background and event reconstruction

Because of the low detection probability and the small coupling, the sensitivity of SHiP to HS particles strongly depends on the background. The main sources of background in the experiment are:

> **Neutrino- and muon-induced:** Inelastic scattering of muons produced in the target or the SND with the decay vessel can generate particles, which enter the decay volume and mimic signal events. The upstream and surrounding background taggers identify charged tracks entering the vessel and veto these tracks.
> For neutrinos, either produced in the upstream material, or entering the decay vessel from the experimental cavern, the situation is slightly different. Neutrinos are not detected by the background taggers due to the very small interaction probability. To suppress deep-inelastic scattering of neutrinos, producing any signal-like final states in the fiducial volume, the decay vessel is evacuated.
>
> **Combinatorics:** Tracks from residual muons, not deflected in the muon shield, or backscattered to the decay volume from the walls in the experimental cavern, can combine to a fake decay vertex in the fiducial volume. While the active muon shield reduces the number of muons entering the fiducial volume by six orders of magnitude, $\mathcal{O}(10^4)$ muons per spill are left entering the fiducial volume of the HSDS. The combinatorial background induced by this large number of muon tracks is vetoed by a coincidence requirement for tracks, imposed by the timing detector.

The mitigation measures implemented reduce the expected background to $0.1-0.3$ events over the experiment runtime of five years and 2×10^{20} PoT [95, p. 10].
With the background reduced to a negligible level and with the independence provided by the direct detection of decay vertices and final states, SHiP is sensitive to a variety of physics models. All reconstructed events must contain an isolated vertex in the decay volume, pointing back to the target [95, p. 9]. In Table 3.1 the dominant final states for the physics models discussed in Chapter 2 are summarised, and categorised by the registering detector.
For the HSDS the signal can be discriminated in fully and partially reconstructed final states, the former containing at least two charged particles and no missing mass, and the latter containing two charged particles and at least one invisible particle (missing mass), which is expected to be a neutrino.

Apart from the neutrino identification discussed in Section 3.2.1, the SND detector is also sensitive to light dark-matter particles. The dominant signal would be a recoil electron from elastic scattering of such particles. The recoil electron creates an isolated electromagnetic shower in the ECC, which is effectively acting as a sampling calorimeter.
The charmed hadrons from neutrino-induced charm production in the SND are identified by a *two-vertex topology*, where the first vertex is produced by the neutrino CC interaction and the second one by the decay of the charmed hadron, observed within a few mm [79, p. 190].

	Physics model	**Final state**
	HNL	$\ell^{\pm}\pi^{\mp}, \ell^{\pm}K^{\mp}, \ell^{\pm}\rho^{\mp}(\rho^{\mp} \to \pi^{\mp}\pi^{0})$
	DP, DS, ALP (fermion)	$\ell^{-}\ell^{+}$
HSDS	DP, DS, ALP (gluon)	$\pi^{-}\pi^{+}, K^{-}K^{+}$
	HNL	$\ell^{+}\ell^{-}\nu$
	ALP	$\gamma\gamma$
	LDM	e, p, hadronic shower
SND	$\nu_{\tau}, \overline{\nu}_{\tau}$ measurements	τ
	Neutrino-induced charm production	$D_s^{\pm}, D^{\mp}, D^{0}, \overline{D}^{0}, \Lambda_c^{+}, \overline{\Lambda}_c^{-}$

Table 3.1: Different final states for given physics models in the SND and HSDS detectors. DP=Dark photon, DS=Dark scalar, LDM=Light dark matter, $\ell = e, \mu, \tau$. Adapted from [93, p. 3].

4 Measurement of the charm cross section in a thick target

In the SHiP experiment, hidden sector particles are expected to be predominantly produced in decays of charmed hadrons. Consequently, the SHiP target is designed such, that charmed interactions dominate the hard and secondary interactions. At the same time, these interactions are a major source of background. Therefore, knowledge of the expected number of charmed hadrons produced in the target is an essential parameter for the normalisation of signal and background in the SHiP experiment.

Moreover, the charm cross section is not only important for SHiP, but charm physics in matter is of interest on its own: Never before has secondary charm production in matter been measured, opening the opportunity to probe current models and improve simulations. In the SHiP experiment one field of interest resulting from charmed interaction is the measurement of tau neutrinos: The tau neutrino flux in the experiment is dominated by the decay chain $D_s \to \tau\nu_\tau \to \nu_\tau\overline{\nu}_\tau X$ for the larger part of the SHiP energy range. A precise prediction of the tau neutrino flux is therefore only possible with a precise knowledge of the charm cross section [3, pp. 93–98]. Here, the charmed interaction is again not only source of the signal, but due to the similar lifetime and mass of charmed hadrons and tau leptons, the decay of charmed hadrons from ν_μ CC interaction constitutes a considerable background for tau neutrino studies [79, p. 183].

In this chapter, the SHiP−charm experiment is introduced, an experiment designed to measure the charm cross section of protons in a thick target of up to 1.6 nuclear interaction lengths. The experiment is set up at the SPS H4 beam line and consists of a spectrometer employing an electro-magnet and an ECC. The spectrometer consists of a pixel tracker, being the link between emulsion detector and electronic detectors, SciFi and drift tube detectors for tracking after the magnet, and is concluded by a muon system consisting of RPC chambers and iron filters.

4.1 Production of charmed hadrons

For the three quarks with mass larger than the QCD scale (Λ_{QCD}), namely charm, bottom, and top, it is possible to compute their production cross section in perturbative quantum chromodynamics (pQCD). The calculation is based on the factorisation approach, in which the cross section is written as a convolution of the parton distribution function (pdf), the partonic hard-scattering cross section, and the fragmentation function [97, p. 1]. Given their hadronisation time, charm and bottom quarks can be observed as intermediate states. The intermediate states need to be accounted for through non-perturbative corrections, increasing the uncertainty on the cross-section calculations. Figure 4.1 shows various measurements of the charm production cross section for different centre-of-mass energies $\sqrt{s}$ and the predictions from pQCD calculations.

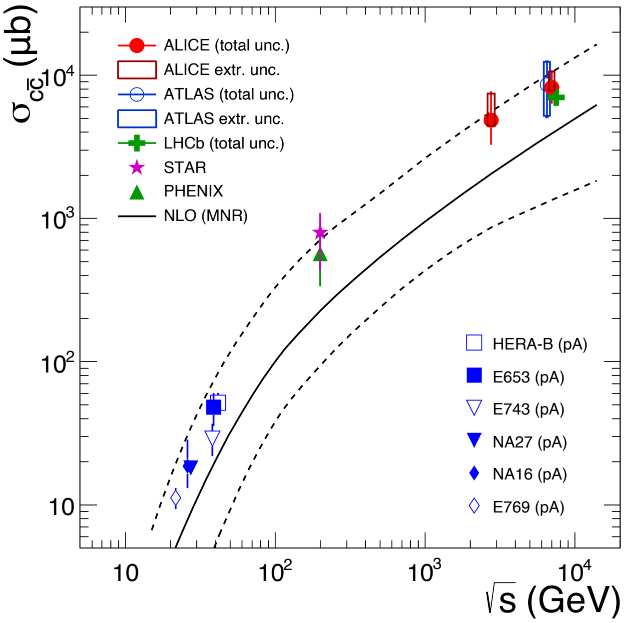

Figure 4.1: Measurements of the total inclusive charm cross section in nucleon–nucleon collisions at different centre-of-mass energies. Next-to-leading order (NLO) pQCD predictions and the corresponding uncertainty are shown as solid and dashed lines, respectively. From [98].

While there is an overall good agreement between experiment and theory, the uncertainties in the theoretical prediction are large. Since the charm-quark mass is relatively close to Λ_{QCD}, a large contribution to the cross section from higher-order corrections is expected, shown also by the next-to-next-to-leading order calculations in [99]. Using the same centre-of-mass energy of $\sqrt{s} = 27.4\,\mathrm{GeV}$ as the SHiP experiment, the NA27 results for a thin target from Figure 4.1 are compared to theoretical predictions for the total charm production cross section in Table 4.1. While the absolute value is strongly depending on the charm quark mass, the uncertainties are dominated by the factorisation and renormalisation scale dependence as well as by the chosen pdf, resulting in a prediction uncertainty of up to one order of magnitude. Altogether, the predictive power of pQCD for the charm production cross section in SHiP is limited by this large uncertainty. For a precise model of the charm background, dedicated experimental measurements are thus necessary.

	exp. NA27	**th. NLO ($m_c = 1.3\,\mathrm{GeV}$)**	**th. NLO ($m_c = 1.5\,\mathrm{GeV}$)**	**th. NLO ($m_c = 1.8\,\mathrm{GeV}$)**
σ in µb	18.1 ± 1.7	$24.3^{+80.1}_{-12.4}$	$10.1^{+22.6}_{-4.8}$	$3.12^{+4.86}_{-1.36}$

Table 4.1: Measured and predicted values for the total charm production cross section in *pp* collisions for different values of the charm quark mass. From [97, p. 2].

As discussed in Section 3.1, the SHiP target has a length of twelve nuclear interactions. At the given centre-of-mass energy, charmed hadrons can not only be produced in primary pN interactions, but also from secondary interaction in the target, leading to a cascade production. Simulations suggest that the production rate in a target with the given thickness is dominated by this cascade effect, increasing the charm yield by a factor of 2.3 compared to primary interaction only [100, p. 2]. The NA27 experiment obtained the cross section in a thin target in which the cascade effect is negligible. Therefore, it is most likely strongly underestimating the charm production cross section in the SHiP target.

4.2 The SHiP–charm experiment

In 2017 the SHiP collaboration proposed to measure the double differential cross section $\mathrm{d}^2\sigma/(\mathrm{d}E\,\mathrm{d}\theta)$ of associated charm production in a thick target [97], and in the following year a first optimisation run was performed, where about 1/10 of the target dataset was collected [46; 101]. The SHiP–charm experiment uses the same $400\,\mathrm{GeV}/c$ proton beam SHiP was originally proposed for, and needs a large magnet for the spectrometer. Therefore, it is set up at the H4 beam line of EHN1 at the CERN SPS north area. It is planned to collect 5×10^7 PoT in several runs, succeeding the optimisation run [97, p. 32]. In the following, the SHiP–charm experiment setup and data acquisition (DAQ), as implemented in the 2018 optimisation run, is introduced.

4.2.1 Experimental setup

Figure 4.2 shows the experimental setup in a lateral view, identifying the different subdetectors. The experiment is divided in target, spectrometer and muon tagger:

Beam counter: Two scintillators are placed most upstream and trigger the experiments DAQ. The DAQ scheme is discussed in Section 4.2.5.

Target: Following the beam counter is the target, which is made of an active and a passive part and is discussed in Section 4.2.2.

Spectrometer: For tracking, a spectrometer consists of three different detectors and the GOLIATH electro-magnet [102]:

- Upstream of the magnet a pixel tracker is placed, which is discussed in detail in Chapter 6.
- Downstream of GOLIATH, a SciFi detector and drift tubes cover inner and outer regions of acceptance.

Muon tagger: To isolate muons in the event, a muon tagger is placed behind the spectrometer, consisting of iron and concrete blocks interleaved with RPCs.

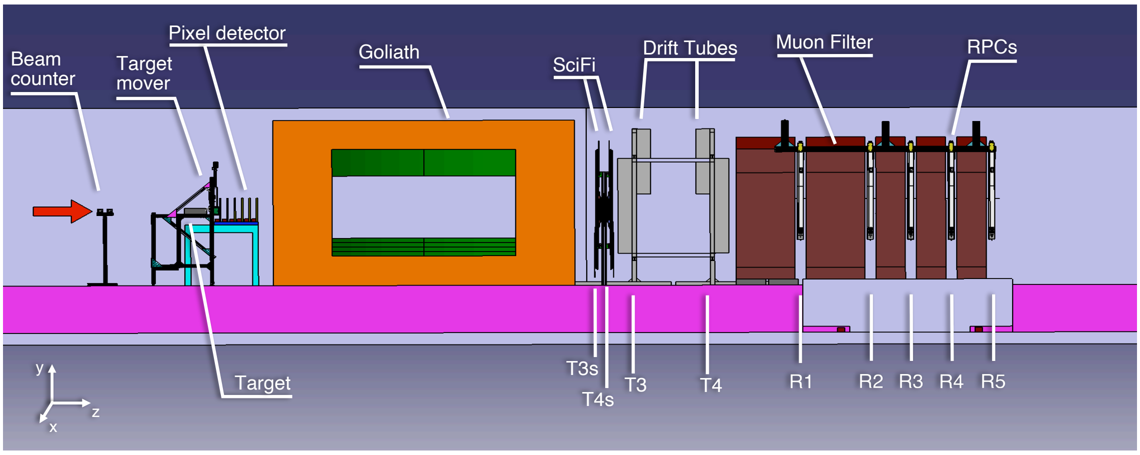

Figure 4.2: Schematic of the SHiP−charm experiment setup. The experiment consists of five sub-detectors. Most upstream, the beam counter is placed followed by the first detector, an active emulsion cloud chamber. The pixel tracker is placed in between emulsion and magnet. The spectrometer is completed by the SciFi detector and a drift tube detector, placed downstream of the magnet. The last detector consists of RPCs and iron/concrete blocks for muon identification.

The sub-detectors are discussed in detail in the following. If not specified otherwise, the coordinate system is defined as follows: The z-axis follows the beam while the y-axis points upwards and the x-axis points to the right looking in the downstream direction.

4.2.2 Target and Emulsion Cloud Chamber

Nuclear emulsions were one of the first detectors employed in high-energy physics [103; 104], and are still used in modern experiments like OPERA and SND@LHC [105–107], providing a spatial resolution which can not be matched by electronic detectors. These photographic films are made from silver halide crystals, bound in a polymer. The emulsion is fixed on a transparent plastic carrier for alignment and setup in the experiment as well as for the readout procedure afterwards. For SHiP– charm, emulsions are produced after a well tested and working recipe [105, p. 10 ff; 108]. Consisting of silver bromide (AgBr) microcrystals bound in gelatine, the emulsion layers with a thickness of 75 µm are fixed on a 180 µm thin transparent sheet of cellulose triacetate. In Figure 4.3 an overview of the features of a nuclear emulsion film is provided. AgBr is a semiconductor with a band gap of 2.6 eV. Once ionising radiation enters the AgBr crystal, electron–hole pairs are created[1], and the electrons are trapped on the crystal surface in positively charged sensitisation centres [109, p. 383 ff]. With the trapped electrons, the now negatively charged sensitisation centre attracts interstitial Ag^+-ions. The silver ion captures the free electron, forming a silver atom which sits at the sensitisation centre. As a result, the silver atom can capture another free electron, and the negatively charged ion attracts another Ag^+ ion, forming a covalent Ag_2-bond. In case this process repeats at least three or four times, the cluster of several silver atoms at the sensitisation centre is large enough for later development, and referred to as latent image centre [110, p. 89]. In the development process, a catalytic redox reaction starts at the small cluster of silver atoms, eventually reducing all silver ions in the AgBr crystal. The crystal is optically identified as a dark grain in the emulsion. The average amplification for this process is in the order of 10^9. The crystals' size and density in the emulsion determine the resolution of the detector [111, p. 1]. For SHiP– charm, the average crystal size is 200 nm and the crystal density is around 230 per 100 µm. With 36 grains per 100 µm for a traversing minimum ionising particle (MIP), the resolution is around 0.8 µm. For a single emulsion film, the plastic carrier is treated with the emulsion on both sides. Thus, a traversing ionising particle will leave a trace of ionised crystals in each of the two active layers on the plastic base. These two traces can easily be connected to one *base track* with an angular resolution in the order of a few mrad [112, p. 3].

---

[1] For a more detailed description of the semiconductor working principle and the interaction of particles with matter the reader is kindly referred to Section 6.1.

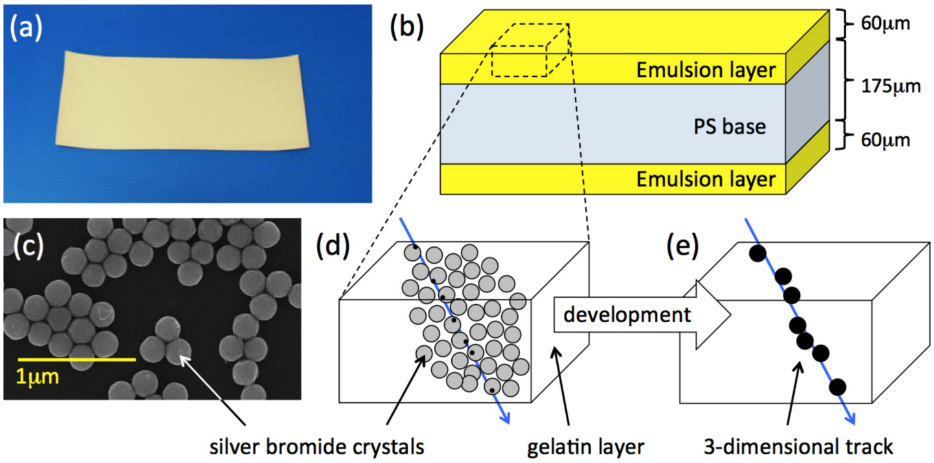

Figure 4.3: Picture of a nuclear emulsion film (a), an illustration of the structure of such a film (b) and an electron microscope image of the crystals in the emulsion (c). The diameter of the crystals is approximately 200 nm. An illustration of the detection principle is shown in (d) and (e). The ionised crystals in (d) are latent image centres, which, after development, form the particle trace. The actual dimensions of emulsion and films in SHiP−charm differ from the ones in this figure. From [113].

To form an ECC, several emulsion films are interleaved with sheets of passive material with short interaction length to increase the interaction rate in the target [114]. Figure 4.4 shows a simplified cross section of such an ECC. For SHiP−charm, the 330 µm thick emulsion films are alternated with 1 mm thick sheets of tungsten or lead, depending on the target configuration. The dimensions of the surface exposed to the particle beam are 12 cm × 10 cm. In total, the ECC contains either 29 or 57 emulsion films, adding up to 0.16 or 0.32 nuclear interaction lengths, respectively. The high resolution, and the capability to observe interactions as they take place in the ECC, is accompanied by the permanence of the ionisation: Once a crystal formed a latent image centre, this crystal is not able to resolve any subsequent ionisation. This attribute inherently restricts the maximum possible density of tracks in the ECC. Additionally, due to the complete lack of electronics in this detector, no time information connected to any of the recorded tracks is provided. At the low interaction rates and track densities of a few tracks per mm^2 of exposed surface area, where emulsion detectors have been employed so far [112, p. 4], these attributes can be easily accounted for. For the amount of data SHiP−charm aims at, this is not possible. The density in electromagnetic showers from secondary electrons is orders of magnitude larger than the OPERA occupancy.

With a fixed beam shape and particle rate, the SHiP−charm experiment uses a different approach: The target is moved through the beam whilst being irradiated, see Figure 4.5. The ECC traverses the elliptically adjusted beam spot in a horizontal path. The time

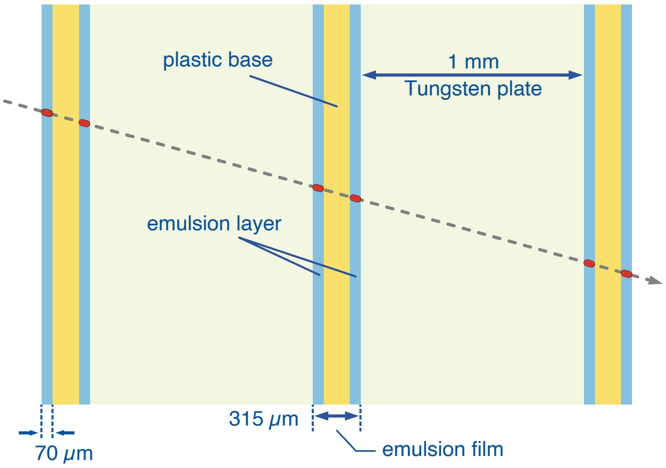

Figure 4.4: Drawing of the ECC cross section. Active layers of nuclear emulsion on a plastic base are separated by tungsten or lead sheets. A MIP traverses the ECC from left to right (dashed line) and ionised crystals create microtracks in the emulsion (red lines).

between spills of particles at the SPS is used to move the ECC vertically, resulting in a snake-like pattern, covering almost the entire brick surface. The ECC is placed on a custom-made target mover, employing two actuators for the x and y movement. To cover the range of 0.16 to 1.6 nuclear interaction lengths, pre-shower bricks of lead with a thickness of 56 mm each are placed approximately 3 cm upstream of the moving ECC[2]. Up to four bricks are used to emulate a target thickness of 280 mm. A summary of all different run configurations is available in Figure A.3 in the Appendix. Figure 4.6 illustrates the moving speed as a function of time:

Acceleration: One second prior to each spill the SPS facility sends a Start of Spill (SoS) signal. This signal triggers the acceleration of the target to a velocity of 2.6 cm/s. To ensure a constant velocity, which is of utmost importance for event reconstruction and matching, the acceleration sequence is completed approximately 0.2 s before the actual spill start.

Lateral movement: The ECC travels through the beam for 4.8 s and approximately 10 cm. The total horizontal distance travelled per spill is 15 cm, approximately 2.5 cm are travelled before and after the spill during the acceleration and deceleration sequences.

---

[2] A sketch of the setup including a pre-shower brick is available in Figure A.2.

[3] An alternative pattern with only 1 cm distance between spills and consequently ten spills on one brick was used for some runs. For information on data taking and run conditions the reader is kindly referred to Section 7.1

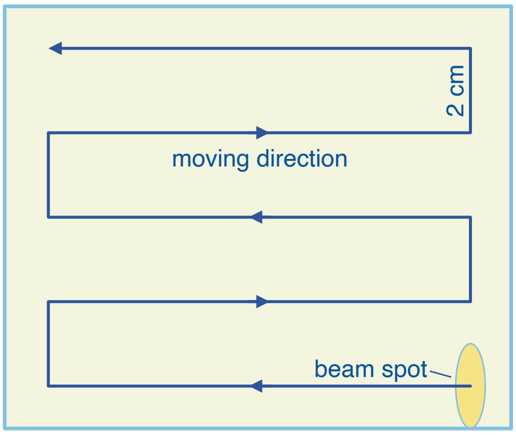

Figure 4.5: Moving pattern from an upstream viewpoint in the ECC rest frame. The beam is tuned to an elliptical shape. During one spill, the detector moves horizontally with a constant velocity. Between spills, the ECC is moved downwards by 2 cm. With this pattern, five spills can be recorded on one brick[3].

Vertical movement: After the spill, the lateral movement of the ECC is stopped, and it is moved downwards by either 1 or 2 cm. For the following spill, the direction of horizontal movement is inverted.

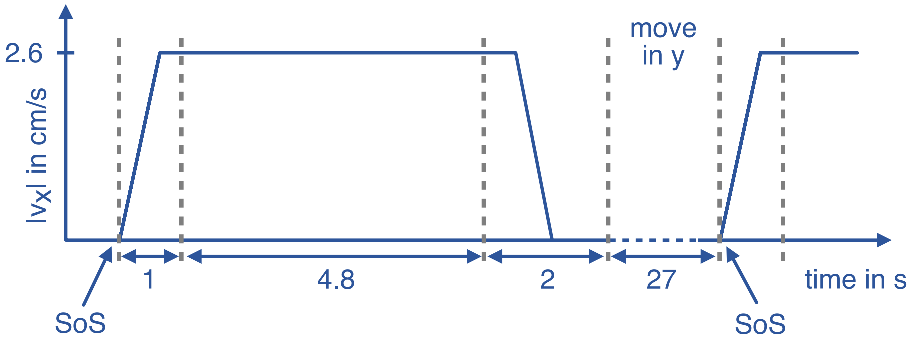

Figure 4.6: Acceleration sequence for the moving target. A constant velocity is reached before the particle spill starts and the target moves uniformly through the beam. After the spill, there is sufficient time to move the target downwards for the next spill.

For an efficient use of beam time and ECC surface, the experiment aims for an occupancy of about 1000 primary protons per cm^2, and a total track density of $\mathcal{O}(10^4/\mathrm{cm}^2)$ is expected. The high occupancy requires a new dedicated reconstruction procedure [115, p. 133 ff].

4.2.3 Spectrometer

For the cross-section measurement, it is important to measure the charge and momentum of the particles exiting the ECC. Both can be extracted from the particle's trajectory in a magnetic field. The Lorentz force deflects the particle according to Equation (4.1), with $\vec{B}$ the magnetic field strength, q the particle's charge and $\vec{v}$ the particle's velocity:

$$\vec{F} = q \cdot (\vec{v} \times \vec{B}) \ . \tag{4.1}$$

Assuming a magnetic field with only one component different from 0, the resulting trajectory is a helix around a cylinder coaxial to the field direction. The projection of this helix on the plane perpendicular to the field is a circle of radius r:

$$\begin{aligned} q \cdot v_{\mathrm{T}} \cdot B &= \frac{m \cdot v_{\mathrm{T}}^2}{r} \\ \Leftrightarrow r &= \frac{p_{\mathrm{T}}}{|q| B} \\ \Leftrightarrow p_{\mathrm{T}} &= |q| \cdot B \cdot r \ , \end{aligned} \tag{4.2}$$

with the transverse momentum given by p_{T} and v_{T} the magnitude of the particle velocity perpendicular to the magnetic field. In the relativistic case $p_{\mathrm{T}} = \gamma m v_{\mathrm{T}}$. For a given charge, the radius solely depends on the momentum. Furthermore, the curvature direction depends on the charge polarity. The magnetic field is parallel to the y-axis, resulting in a deflection of charged particles in the $x - z$ plane. To measure the particle trajectories, SHiP−charm uses a spectrometer made of three detectors and the GOLIATH magnet.

Pixel detector: It is crucial for the event reconstruction and the linking of ECC data with the electronic detectors. For a detailed description, the reader is kindly referred to Chapter 6.

SciFi detector: The SciFi detector is placed downstream of the magnet. It offers four modules of 40 cm × 40 cm size. Each module consists of two planes, where one of the planes is rotated by 2° around the beam axis. The SciFi detector offers 1 D resolution of about 270 µm in the direction perpendicular to the scintillating fibres. Therefore, every second module is rotated by $\pi/2$ to obtain 2 D information about particle trajectories.

Drift tube detector: The drift tube detector in the outer acceptance region is an OPERA prototype and consists of six modules with 48 tubes in four layers [116]. In a former experiment at the same beam line, prior to SHiP−charm, a resolution of

373 µm perpendicular to the tube axes was measured for this arrangement [92, p. 3]. The modules are arranged vertically in two layers, to measure the x coordinate of particle tracks, i.e. resolve the magnetic deflection.

Since the detectors of the spectrometer are not placed inside the magnetic field, the bending radius can not be measured directly. Instead, the deflection from the incident angle $\Delta\theta$ is measured according to Equation (4.3):

$$\sin\left(\frac{\theta}{2}\right) \approx \frac{\Delta\theta}{2} = \frac{d \cdot B \cdot q}{2 \cdot p_{\mathrm{T}}} \,. \tag{4.3}$$

With d being the distance travelled through the uniform magnetic field.

4.2.4 Muon tagger

The most downstream detector in the setup is the muon tagger, consisting of five RPCs interleaved with iron blocks. The purpose of this detector is to tag events from the muon channel of charmed hadroproduction by separating muons from charged hadrons. The passive material in between the RPC modules allows for the separation of charged hadrons, which are stopped in the iron blocks, and rarely interacting muons, which pass the iron. By requiring hits in several RPCs, and especially in the downstream ones, it is possible to achieve a high purity in the muon selection.

4.2.5 Trigger and data acquisition

In order to reconstruct events, data obtained from the individual sub-detectors needs to be combined. Besides the synchronisation of different electronic sub-detectors of the spectrometer, the tracks recorded in the nuclear emulsion have to be assigned to the corresponding spectrometer events. In this section, the integration of the electronic detectors and the target mover is discussed, while the reader is kindly referred to Section 7.4 for a detailed discussion of the ECC detector integration.

To integrate the different detector technologies, a two-stage DAQ was chosen. Each detector system has an independent readout system (local DAQ), sending read-out data to a central DAQ. Figure 4.7 shows a schematic of the DAQ framework. On the local level, the DAQ has to accept SoS, End of Spill (EoS) and Start of Run (SoR) signals, as well as triggers.

The trigger signal is issued by the beam counter in front of the experiment for every primary beam particle coincidentally registered in the two scintillators, and sent to a central trigger logic. The central trigger logic distributes the signal to all local DAQs, which timestamp

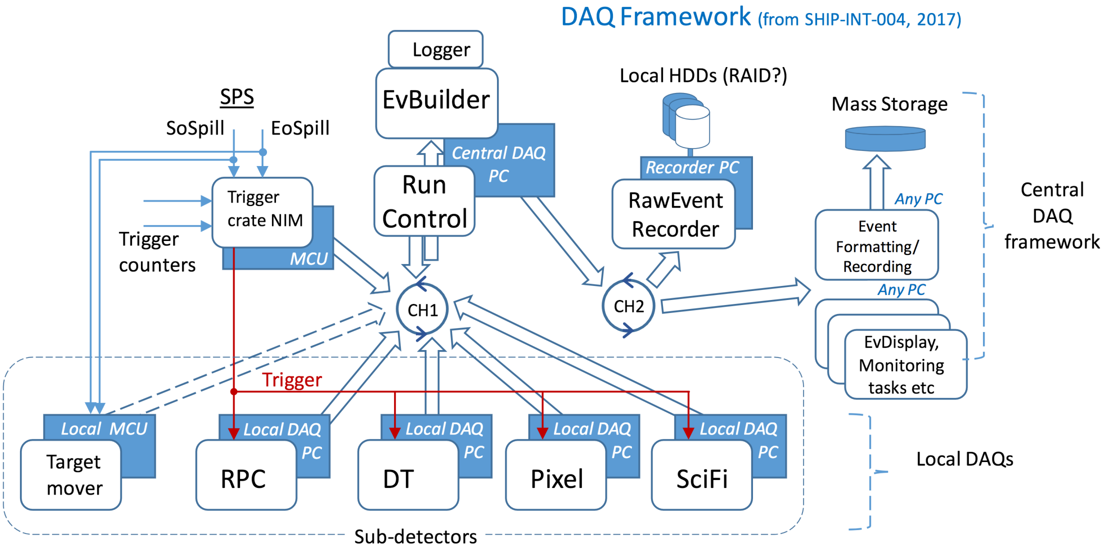

Figure 4.7: DAQ scheme for the SHiP−charm optimisation run. The DAQ is two-staged with independent local DAQs for the sub-detectors, controlled by the run control instance (CH1). The central DAQ can be run independently of run control (CH2) and is also capable of offline data reconstruction. From [117, p. 2].

the arrival of a trigger and buffer registered hits. The sub-detectors do not receive a globally synchronised clock and need to clock in the analogue trigger signal individually. To ensure synchronisation of the sub-detector clocks, the SoS signal is used to reset all local DAQ clocks prior to each spill. The number of readout channels, the complexity of the local DAQ, and the occupancy, vary for the different detector systems, resulting in considerably different dead times for the same event. To account for this, each local DAQ can send a BUSY signal to the central trigger logic. Consequently, the trigger output is suppressed for the time the detector is busy. The EoS signal marks the end of a beam spill and triggers the local DAQs to send out frames with the recorded hit data to the central DAQ, referred to as *run control*.

The run control machine aligns the data frames of the local DAQ instances and builds the global event. The event data is decoded on a separate machine, independently of the data taking, and at the same time saved as raw data for later analysis.

5 Principles of silicon sensors

In silicon sensors, particles are detected by their energy loss due to ionisation. Silicon sensors therefore can detect charged particles and photons, based on their Coulomb interaction with the sensor material. The energy loss creates charge carriers which drift in an electric field, creating a signal to be read out. The following chapter explains the interaction of particles with matter, charge creation and transport in the sensor.

5.1 Interaction of particles with matter

Charged particles predominantly ionise and excite the lattice atoms in numerous single collisions, where with each interaction the particle loses energy. The mean energy loss per path length can be described by the Bethe-Bloch formula [37; 118–120, p. 550] :

$$-\left\langle \frac{\mathrm{d}E}{\mathrm{d}x} \right\rangle = Kz^2 \frac{Z}{A} \frac{1}{\beta^2} \left[\frac{1}{2} \ln \left(\frac{2m_e c^2 \beta^2 \gamma^2 W_{\mathrm{max}}}{I^2} \right) - \beta^2 - \frac{\delta(\beta\gamma)}{2} \right] . \tag{5.1}$$

Here

- $K = 4\pi N_A r_e^2 m_e c^2 = 0.307\,\mathrm{MeV\,cm^2\,mol^{-1}}$ with r_e the classical electron radius and m_e the electron mass,
- z, β are charge and velocity of the particle,
- Z, A are atomic number and atomic mass number of the scattering medium,
- $W_{\mathrm{max}} = \frac{2m_e c^2 \beta^2 \gamma^2}{1+2\gamma m_e/M+(m_e/M)^2}$ is the maximum energy transfer in a single collision,
- I is the mean excitation energy of the scattering medium. For silicon $I = 173\,\mathrm{eV}$ [37],
- $\delta(\beta\gamma)$ is a density correction factor.

The Bethe-Bloch formula is valid for *heavy* particles, i.e. particles of mass $M \gg m_e$. It can predict the energy loss for particles with $0.1 < \beta\gamma < 1000$ with an error of a few percent [37, p. 550]. For electrons, the Bethe-Bloch formula has to be modified to account for the different kinematic situation where incident particle and scatterer have comparable masses, and for the quantum mechanical ambiguity of both scattering partners. A more detailed discussion of the modifications can be obtained from Seltzer and Berger [121] and in the review of particle physics [37, p. 555]. Since the energy loss leads to the particle being stopped in sufficiently thick material eventually, the mean $\mathrm{d}E/\mathrm{d}x$ is also called stopping power. In order to be independent of the scattering material's density it is typically given in units of $\mathrm{MeV\,cm^2/g}$ as *mass stopping power*. The mass stopping power for protons and electrons in silicon is shown in Figure 5.1. For low energies, the relation is dominated by the $1/\beta^2$ term. For $\beta\gamma \approx 3$ the mean energy loss becomes minimal, independent of the particle type. At higher energies the mass stopping power grows slowly, therefore particles with $\beta\gamma \gtrsim 3$ are considered as MIPs. In case of very high energies or low particle mass, the energy loss is dominated by Bremsstrahlung: The interaction of a charged particle with the Coulomb field of a nucleus results in the emission of a photon [122, p. 53 ff]. The

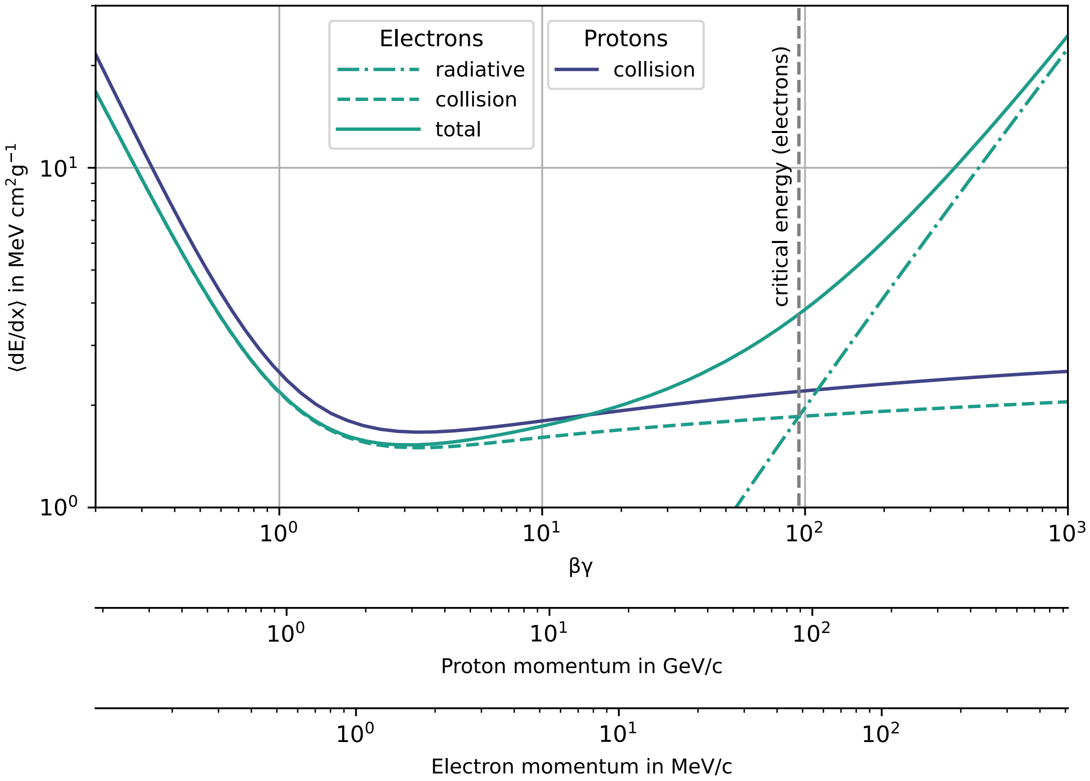

Figure 5.1: Mass stopping power for protons and electrons in silicon. The minimum at $\beta\gamma \approx 3$ can be identified for both particle types. The negligible contribution of nuclear interactions to the energy loss of protons is omitted. For electrons, the losses due to Bremsstrahlung dominate for energies above the critical energy. Values for protons are calculated with Equation (5.1), representative for *heavy* particles with $M \gg m_e$. Values for electrons are taken from the ESTAR database [123].

cross section for this effect is proportional to E/m^2, and considering today's experiments energy ranges it is only relevant for electrons, positrons and high-energetic muons. The particle energy at which the energy loss due to Bremsstrahlung equals the energy loss due to collision is defined as critical energy E_c, in silicon it is 48 MeV for electrons and 580 GeV for muons [123; 124, p. 22]. Above this limit the energy loss can be approximated as [122, p. 61]

$$\left(-\frac{\mathrm{d}E}{\mathrm{d}x}\right)_{rad} = \frac{1}{X_0}E \Rightarrow E(x) = E_0 \exp\left(-\frac{x}{X_0}\right). \tag{5.2}$$

The *radiation length* X_0 is defined as the path length after which the incident particle's energy is reduced to 37 % of its initial energy and depends on the material's density. In silicon, $X_0 = 9.37\,\mathrm{cm}$ [125]. The ratio x/X_0 is commonly referred to as the *material budget* and given in units of %. The energy loss by Bremsstrahlung is realised in a few high-energetic photons which do not contribute to the energy deposition in a thin silicon sensor due to their low interaction probability[1]. In case of collisions with high-energy transfer ($W \gg I$), a *high-energy knock-on electron* or *δ-electron* is created [122, p. 37]. The emission angle of δ-electrons shows a maximum for $\theta = 90°$ with respect to the projectile's incident angle, corresponding to a kinetic energy in the order of some keV. Consequently, the energy deposition of the δ-electron in the material is dominated by the $1/\beta^2$ part of Equation (5.1), creating a high-density ionisation path. If this path can not be resolved by the sensor, it can reduce the spatial resolution significantly. δ-electrons can leave the sensor without contributing to the deposited energy.

5.1.1 Statistical fluctuation in energy loss

The interaction of particles with matter is a discrete process and the mean energy loss per path length described by Equation (5.1) fluctuates as the number of interactions per path length as well as the corresponding energy transfer varies. For large numbers of collisions, i.e. a thick scatterer, the total energy loss in the material can be approximated with a Gaussian distribution, following the central limit theorem. In contrast, for thin scatterers, such as typical silicon sensors, the Gaussian approximation is not valid. Two effects govern the energy loss distribution in thin sensors: δ-electrons from high-energy-transfer collisions and the probability to fully stop the incident particle. This leads to an asymmetric shape of the distribution with a long tail towards high-energy depositions. The resulting distribution is Landau-shaped and the most probable energy deposition is considerably smaller than the mean [37, p. 552]. In thin sensors, the tail of the Landau distribution often can not be measured since particles leave the sensitive volume, which can result in a strongly

---

[1] Photon interaction is discussed in Section 5.1.3.

underestimated mean value. Therefore, energy loss in thin sensors is generally characterised by the most probable value (MPV) of the Landau distribution. The MPV is given by Equation (5.3) [126, p. 695]:

$$\Delta_p = \xi \left[\ln\left(\frac{2m_e c^2 \beta^2 \gamma^2}{I}\right) + \ln\left(\frac{\xi}{I}\right) + j - \beta^2 - \delta(\beta\gamma) \right] , \tag{5.3}$$

with $j = 0.2$ being a correction factor and

$$\xi = \frac{1}{2} \frac{Z \cdot z^2}{A \cdot \beta^2} \cdot K \cdot \rho \cdot x , \tag{5.4}$$

where x is the sensor thickness. Considering a MIP traversing a 200 µm silicon sensor, $\Delta_p \approx 51\,\mathrm{keV}$ and the most probable energy loss per unit length $\Delta_{p/x} = 257\,\mathrm{eV/\mu m}$.

5.1.2 Multiple Coulomb scattering

The interaction of charged particles with matter does not only lead to energy loss but also influences the direction of incident particles. The particles frequently scatter elastically at the nuclei with a cross section following the Rutherford formula:

$$\left.\frac{\mathrm{d}\sigma}{\mathrm{d}\Omega}\right|_{\mathrm{Rutherford}} = \left(\frac{zZ\alpha\hbar}{\beta p}\right)^2 \frac{1}{4\sin^4(\theta/2)} , \tag{5.5}$$

with the scattering angle θ, charge z, velocity β and momentum p of the incident particle, Z the charge of the nucleus and α is the fine-structure constant [122, p. 65]. The resulting distribution of scattering angles was described by Molière [127] but for most practical purposes the number of scatterings are large enough and the scattering angles small enough for a Gaussian approximation. For particle tracking in silicon sensors, the Gaussian approximation covers more than 99.9 % of scattering angles. The standard deviation of this distribution is then given by the Highland-Formula [128; 129]:

$$\theta_{MS} = \frac{13.6\,\mathrm{MeV}\,c^{-1}}{\beta p} z \sqrt{\frac{x}{X_0}} \left[1 + 0.038 \cdot \ln\left(\frac{x}{X_0}\right)\right] , \tag{5.6}$$

with x/X_0 the material budget, z, β, p (in MeV) of the incident particle. Notable are the dependence on particle momentum and material budget. Since the particle deviates from a straight path, multiple scattering deteriorates the spatial resolution of any detector. Consequently, tracking detectors are as thin as possible such to minimise x/X_0 and therefore θ_{MS}.

5.1.3 Energy loss of photons

While a short overview is given here, detailed discussions of photon interaction with matter are available in literature [122, p. 70 ff; 130, p. 136 ff]. Charged particles continuously lose energy in the scatterer and are stopped in a fixed, material-dependent absorption range, however the number of photons that reach a certain penetration depth x decreases exponentially in the absorber, following the Lambert-Beer law:

$$N(x) = N_0 e^{-\mu x} \ , \tag{5.7}$$

where μ is the attenuation coefficient. The inverse attenuation coefficient

$$\lambda = \frac{1}{\mu} = \frac{1}{n\sigma} \tag{5.8}$$

is the mean free path length with $n = \rho \frac{N_A}{A}$ the target density and σ the total interaction cross section. It can be interpreted as the distance after which a photon is absorbed with $1 - 1/e \approx 63\,\%$ probability. The attenuation coefficient for photons in silicon is shown in Figure 5.2. It is the sum of three most relevant processes, each dominant in a different energy regime.

Photoelectric effect: A photon of energy $E = h\nu$ interacts with the electrons of the absorber and transfers its full energy to the atom. For the photoelectric effect, the photon energy needs to exceed the binding energy B_e of electrons such that the atom is ionised and an electron with kinetic energy $T = h\nu - B_e$ leaves the atom. The photoelectric effect is dominant for energies in the keV regime.

Compton scattering: A photon scatters elastically off a shell electron which absorbs part of the photons energy and leaves the atom. The electron is considered *quasi-free* since, to first order, the binding energy does not affect the scattering interaction. The amount of energy $T = E_\gamma - E'_\gamma$ transferred depends on the scattering angle:

$$E'_\gamma = \frac{E_\gamma}{1 + \frac{E_\gamma}{m_e c^2}\left(1 - \cos\theta\right)} \ . \tag{5.9}$$

The scattered photon is not necessarily absorbed and can, given sufficient energy, continue to scatter off atoms. This creates the continuous energy spectrum called *Compton continuum*. For a scattering angle of $\theta = 180°$ the maximum energy is transferred. The upper end of the spectrum is constrained by this *Compton edge*. Compton scattering is the dominant interaction for photons with energies around 1 MeV.

Pair production: If the photon energy $E = h\nu \geq 2m_e = 1.022\,\text{MeV}$ the photon can convert into an electron–positron pair. The conversion needs an atom's nucleus as recoil partner to satisfy momentum conservation. The cross section for pair production is given by

$$\sigma_{pair} \approx \frac{7}{9}\frac{1}{X_0}\frac{A}{N_A\rho}\,, \tag{5.10}$$

and is dominant for photon energies above 20 MeV.

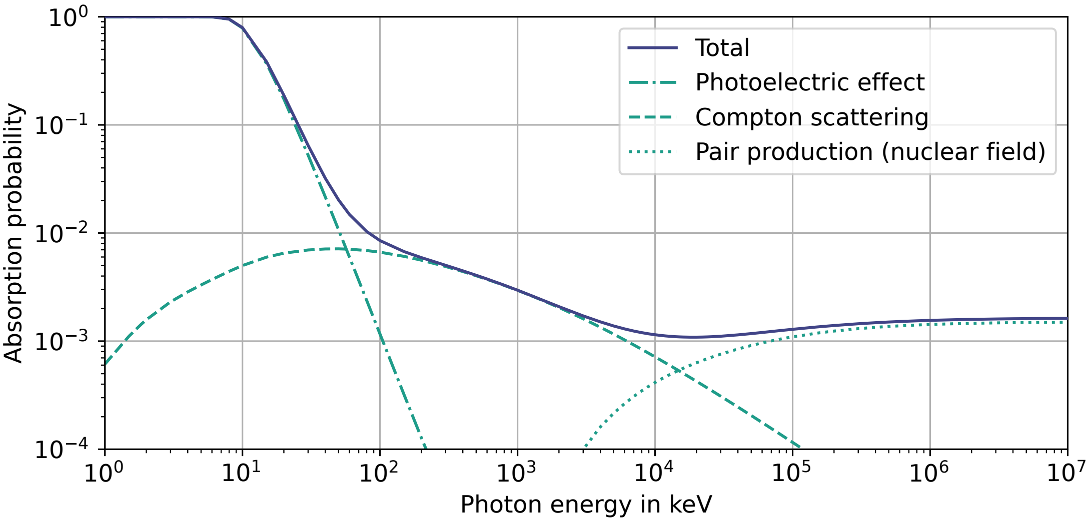

Figure 5.2: Absorption probability for photons in 200 µm of silicon. The photoeffect dominates up to 60 keV, Compton scattering up to 20 MeV and pair production dominates from there onwards. Values taken from the XCOM database [131].

While the high absorption probability for low energetic photons results in excellent detection capabilities, Figure 5.2 shows a strongly decreasing absorption probability in silicon for photons of more than $\mathcal{O}(10\,\text{keV})$. Therefore, silicon pixel detectors have a limited capability of detecting high-energetic photons.

5.2 Particle detection at the pn-junction

Silicon is a semiconductor with a diamond cubic lattice structure. The distance between atoms causes the energy levels of single atoms to split due to the influence of the neighbouring atoms. Single energy states can not be resolved and groups of states can be represented in energy bands instead. The *valence band* is the last filled energy band, while the higher *conduction band* still offers free charge carrier states. In case of a semiconductor, the valence and the conduction band are separated by a band gap in which no energy states are allowed. A sketch of the energy band structure for silicon is shown in Figure 5.3. For silicon, the gap energy is $E_g = 1.12\,\mathrm{eV}$ at room temperature [132, p. 16]. At this level, thermal excitation or energy transfer by ionisation of charged particles is sufficient for electrons to overcome the band gap and transition into the conduction band while a corresponding hole remains in the valence band. The electron and the hole are considered free charge carriers with different effective mass [133, p. 15]. The intrinsic charge carrier density n_i can be calculated as the product of the density of available states and the occupation probability [122, p. 268].

$$n_i = \sqrt{N_C N_V} \cdot \exp\left(-\frac{E_g}{2k_B T}\right) \approx 1.01 \times 10^{10}\,\mathrm{cm}^{-3} \tag{5.11}$$

for silicon at room temperature [132, p. 20]. Here N_C and N_V are the effective densities of states in the *conduction* and *valence* band, respectively. Considering the energy–momentum relation of electrons in the different energy bands, semiconductors can be classified in *direct* and *indirect*. The energy minimum in the conduction band of an indirect semiconductor has a different crystal momentum compared to the maximum in the valence band, resulting in a necessary momentum transfer for the transition of electrons from the valence to the conduction band [132, p. 12 ff]. Therefore, for an indirect semiconductor, such as silicon, the mean energy necessary for electrons to transit is larger than the energy gap. For silicon

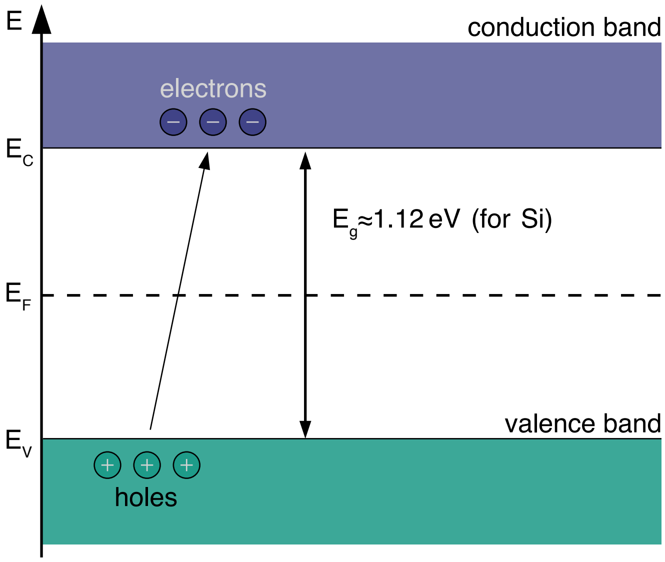

Figure 5.3: Simplified band structure for an un-doped semiconductor, adapted from [134]. The energy gap is sufficiently small for charge carriers to be lifted in the conduction band by thermal excitation.

the mean required energy to create an electron-hole pair is $w = 3.66\,\mathrm{eV}$ [135]. With a most probable energy loss per unit length $\Delta_{p/x} \approx 257\,\mathrm{eV/\mu m}$ (see Section 5.1.1) at a detector thickness $d = 200\,\mathrm{\mu m}$, one can calculate the expected number of charge carriers created by a MIP in the sensor:

$$N_{\mathrm{ion}} = \frac{\Delta_{p/x} \cdot d}{w} \approx 1.4 \times 10^4\,\mathrm{e{-}h}\ . \tag{5.12}$$

Given a typical sensor of area $A = 2 \times 2\,\mathrm{cm}^2$ the number of intrinsic charge carriers is:

$$N_i = n_i \cdot A \cdot d \approx 8.1 \times 10^8\,\mathrm{e{-}h}\ . \tag{5.13}$$

Thus, the signal is four orders of magnitude smaller than the number of intrinsic charge carriers present at room temperature at any time. It follows, that intrinsic silicon can not be used for particle detection. For actual detection of particles the charge carrier creation by external ionisation has to dominate the overall creation. To achieve this, a *pn-junction* is formed in the silicon bulk by doping it with acceptors and donators respectively. Doping is the controlled introduction of impurities from chosen elements into the crystal lattice. Silicon can be doped with pentavalent elements like phosphorus, also called *donors*, to introduce an excess of electrons. This is called *n-doping*. Introducing trivalent elements like boron or aluminium, called acceptors, creates an excess of holes and is called *p-doping*. Dopants introduce new energy levels in the band gap, for donors, slightly below the conduction band, and for acceptors, levels slightly above the valence band ($E_{A/D} - E_{V/C} \approx \pm 0.05\,\mathrm{eV}$) [132, p. 21]. Doping concentrations between $1 \times 10^{12}\,\mathrm{cm}^{-3}$ – $1 \times 10^{18}\,\mathrm{cm}^{-3}$ are common.

A pn-junction is then realised in direct contact of a p-doped and an n-doped semiconductor. Figure 5.4 shows a simplified view of the junction at thermal equilibrium. In the p-doped crystal, holes are dominant and therefore referred to as majority charge carriers, whereas electrons are majority charge carriers in the n-doped crystal. Driven by the strong gradient in charge carrier concentration, the free majority charge carriers of either side diffuse towards the minority region, creating a diffusion current I_{diff}. At the junction the charge carriers recombine, creating a zone without free charge carriers. This zone is called *depletion zone*.

Albeit free charge carriers are absent, the ionised atom cores of the crystal remain, leaving a *space charge* in the depletion zone. Since the respective majority charge carriers have recombined, the p-doped crystal now has a negative space charge while the n-doped crystal is positively charged. The opposing charges create an electrical field which is creating a drift current I_{drift} in opposite direction to I_{diff}. Once thermal equilibrium is reached, a diffusion, or *built in* potential V_{bi} arises. For silicon $V_{\mathrm{bi}} \approx 0.6\,\mathrm{V}$. Outside the depletion zone, the semiconductor crystal is electrically neutral. Since the overall crystal has to stay electrically neutral, the extent of the depletion zone in either doping domain $x_{n/p}$ is inversely proportional to the doping concentration:

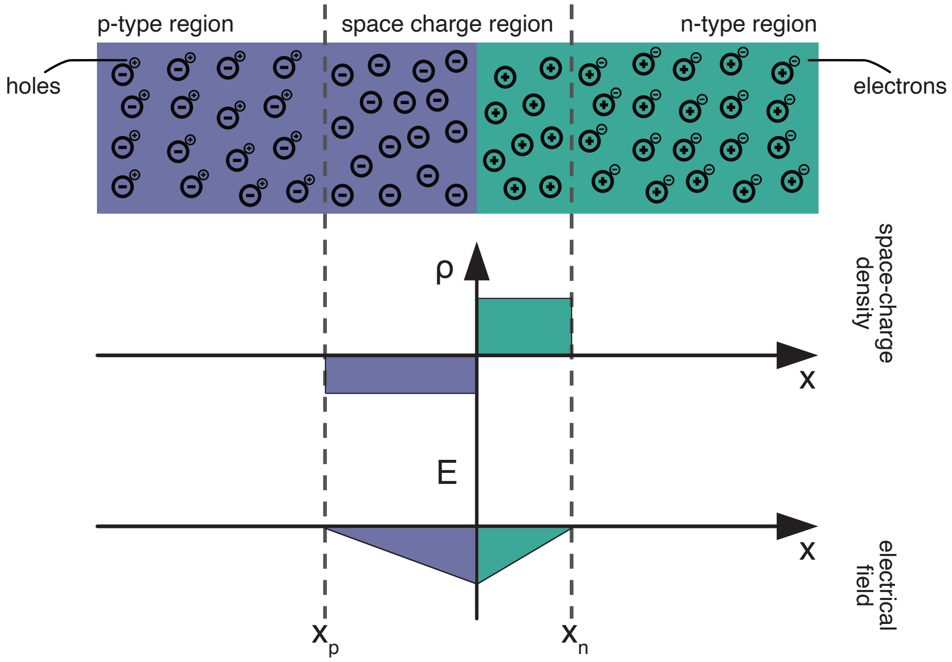

Figure 5.4: Representation of charge carrier density and electric field at an abrupt pn-junction, adapted from [122].

$$x_n = \sqrt{\frac{2\epsilon\epsilon_0}{e}\frac{N_A}{N_D(N_D+N_A)} \cdot V_{\mathrm{bi}}} \quad \wedge \quad x_p = \sqrt{\frac{2\epsilon\epsilon_0}{e}\frac{N_D}{N_A(N_D+N_A)} \cdot V_{\mathrm{bi}}}\ , \tag{5.14}$$

and consequently

$$\frac{x_n}{x_p} = \frac{N_A}{N_D}\ . \tag{5.15}$$

A planar silicon sensor for particle detection usually features an array of shallow (typically a few µm), heavily-doped implants and one thick, lightly-doped domain, as indicated in Figure 5.5. The depletion zone width is typically in the order of some 10 µm [122, p. 277] and much smaller than the sensor thickness. For particle detection, the depletion zone is of interest due to the absence of free charge carriers. Here, ionisation is by far the dominant source of charge carrier creation. Thus, it is beneficial to extend the depletion zone as far as possible, ideally across the whole sensor. To increase the depletion zone, an external bias voltage V_{bias} is applied to the pn-junction in reverse direction (the negative potential at p-type and the positive potential at the n-type domain). The external voltage serves a second purpose: Without external field, the created charge carriers would quickly

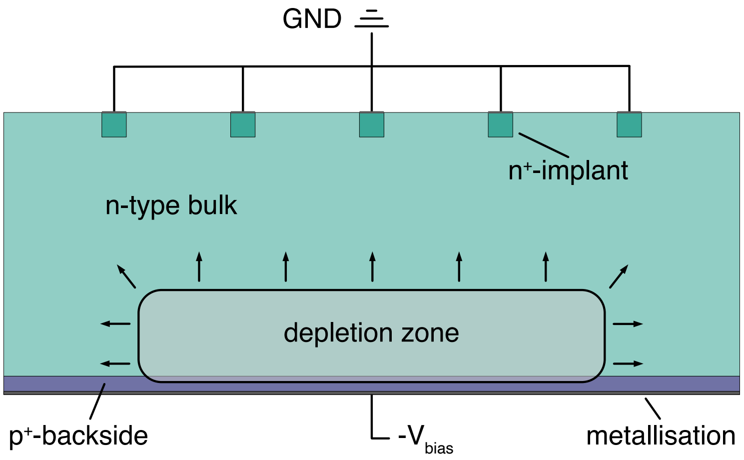

Figure 5.5: Simplified lateral view of an n^+ in n pixel sensor with applied bias voltage (not to scale). The pn-junction is at the sensor backside. Consequently, the growth of the depletion zone begins there.

recombine, and no signal would be detectable. With an external voltage applied, the charge carriers drift in the electric field towards the electrodes, where a signal is induced. The depletion zone width d changes with external voltage according to

$$d_{n/p} \approx \sqrt{\frac{2\epsilon\epsilon_0}{e}\frac{1}{N_{D/A}}(V_{\mathrm{bi}} + V_{\mathrm{bias}})} \,. \tag{5.16}$$

Since one doping domain is usually very thin and typically $V_{\mathrm{bias}} \gg V_{\mathrm{bi}}$, the overall depletion width can be approximated to

$$d_n \approx 0.55 \sqrt{\frac{\rho}{\Omega\,\mathrm{cm}}\frac{V_{\mathrm{bias}}}{\mathrm{V}}}\ \mu\mathrm{m} \quad \wedge \quad d_p \approx 0.32 \sqrt{\frac{\rho}{\Omega\,\mathrm{cm}}\frac{V_{\mathrm{bias}}}{\mathrm{V}}}\ \mu\mathrm{m} \,, \tag{5.17}$$

with the bulk resistivity

$$\rho \approx \frac{1}{q \cdot \mu_{e/h} \cdot |N_{\mathrm{eff}}|} \tag{5.18}$$

for the respective doping type. μ is the charge carrier mobility for the respective doping type and $N_{\mathrm{eff}} = N_D - N_A$ is called the effective doping concentration. The difference in depletion width for n- and p-type bulk material is due to the lower mobility of holes compared to electrons [122, p. 283]. The voltage V_{dep} necessary to deplete the whole silicon bulk is called *depletion voltage* and is proportional to N_{eff}:

$$V_{\mathrm{dep}} = \frac{e \cdot d_{\mathrm{det}}^2}{2\epsilon} \cdot N_{\mathrm{eff}} \,, \tag{5.19}$$

with the bulk thickness d_{det} [130, p. 458] and $\epsilon = \epsilon_0\epsilon_{\mathrm{Si}}$ is the silicon electric permittivity.

5.2.1 Charge carrier signal in a silicon pixel sensor

The charge carriers created in the bulk by ionisation drift in the electrical field. Electrons drift towards the n-doped domain and holes towards the p-doped domain. A current signal i is induced at the readout electrodes by the charge carrier drift, following the *Shockley-Ramo theorem* [136; 137]:

$$i = q\,\mu_{e/h}\,\vec{E}_w \cdot \vec{E}_D \;, \tag{5.20}$$

with the *weighting field* $\vec{E}_w$ and the external field $\vec{E}_D$ [122, p. 147]:

$$\vec{E}_D(x) = -\left(\frac{V_\text{bias} + V_\text{dep}}{d} - \frac{2V_\text{dep}}{d^2} \cdot x\right) \vec{e}_x \;. \tag{5.21}$$

The weighting field only depends on the electrode geometry, and for small electrodes the fields of single electrodes overlap such that also neighbouring electrodes see a signal. It is worthwhile to note that charge carriers closest to the electrode dominate the signal induction [138, p. 27]. The charge carrier mobility depends on the applied field E_D [122, p. 148]. Thus, to reduce dead time as well as to increase charge collection in case of irradiation, an overdepletion of the sensor is beneficial, meaning that E_D is larger than the field necessary to deplete the full sensor bulk. The charge collection time and the current induced in a silicon sensor are depicted in Figure 5.6. The current is induced by the movement of charge carriers from their origin and vanishes, once all created charge carriers have been collected. It is evident that electron movement dominates the induced current and that electron collection is rather quick compared to the holes. For practical purposes, therefore, one can neglect the contribution of holes.

5.2.2 Leakage current and thermal runaway

In a semiconductor detector a *leakage current* I_leak is observed. While there are different sources of leakage current, the main contribution is thermal generation of electron–hole pairs in the depletion zone. The size of I_leak is influenced by the concentration of impurities in the bulk material, and generally increases with radiation damage. While radiation damage is not studied here, the temperature dependence of I_leak needs to be considered for the detector design:

$$I_\text{leak}(T) \propto T^2 \exp\left(\frac{-E_\text{eff}}{2k_B T}\right) . \tag{5.22}$$

Here, E_eff is the effective energy necessary for charge carrier activation, and was determined experimentally for silicon to be $E_\text{eff} \approx 1.21\,\text{eV}$ [139, p. 3]. If the sensor temperature is too

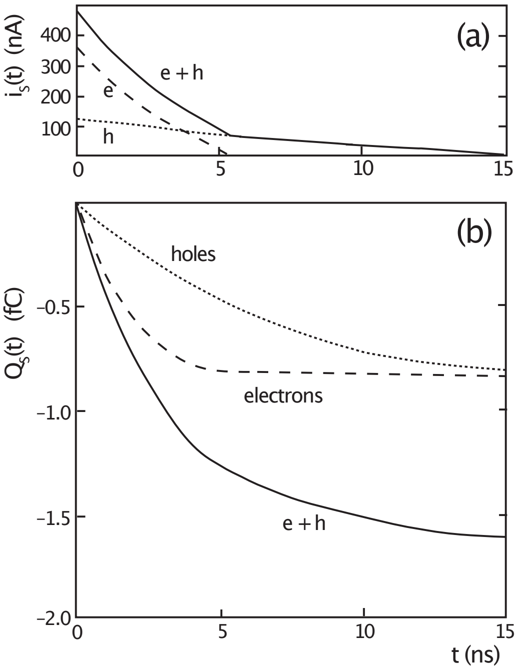

Figure 5.6: Signal evolution of current (a) and charge (b) induced at the negative electrode of a 300 µm thick silicon detector for a traversing charged particle. The sensor is overdepleted by a factor of 1.5. From [122, p. 150].

high, the increased current flow starts a feedback loop by heating up the sensor, creating more leakage current, which consequently can destroy the sensor. This effect is referred to as *thermal runaway*. A detailed discussion of the magnitude and dependence of leakage current was provided by Chilingarov [139]. The influence of leakage current on the setup and operation of the pixel tracker in SHiP−charm is discussed in Section 6.2.

6 The SHiP–charm pixel tracker

Pixel detectors are the technology of choice when high occupancy and demand for precise tracking meet. State-of-the-art pixel detectors for high-energy physics applications are radiation tolerant, feature fast readout circuitry and high spatial resolution. Pixel detectors are generally made of semiconductor materials, where silicon is used predominantly due to it being widely available and well understood [122, p. 260].
For the SHiP–charm experiment, the pixel tracker is crucial since it connects the target and the spectrometer, providing timing information to the ECC tracks and vertices. Within the scope of this thesis, the pixel tracker for SHiP–charm was planned, built and operated in the experiment setup.

6.1 The ATLAS IBL pixel detector

Today, two different design concepts for pixel detectors exist: the hybrid and the monolithic design. For a hybrid detector, sensitive volume and electronic readout are realised on different chips and the sensor pixels are paired with the readout circuitry to a *detector module* afterwards, while the monolithic approach integrates the whole detector on one chip. The monolithic approach is only possible since commercial complementary metal-oxide-semiconductor (CMOS) processes with high bulk resistivity have become available in recent years and are subject of present research [140]. The detector used within the SHiP–charm experiment is made of hybrid detector modules of the ATLAS Insertable B Layer (IBL) upgrade production [141]. The hybrid concept brings the advantage that sensor and readout can be realised in the technology best suited for the respective application. For the readout chip, requirements are radiation hardness, high logic density and low power consumption, while the sensor should offer low noise and large signal generation. Consequently, the readout chip was designed in a commercial 130 nm IBM CMOS technology while the sensor is from a custom process where the material qualities could be controlled to a certain degree. The disadvantage for the hybrid concept lies in the necessary hybridisation step, connecting sensor and readout to the final module. This step reduces the yield which increases the cost for detector module production. Second, the material budget is significantly higher for a hybrid detector. Figure 6.1 shows the hybrid detector scheme where the readout chip, also called front-end, is on the bottom, connected to the sensor on the top via solder bumps.

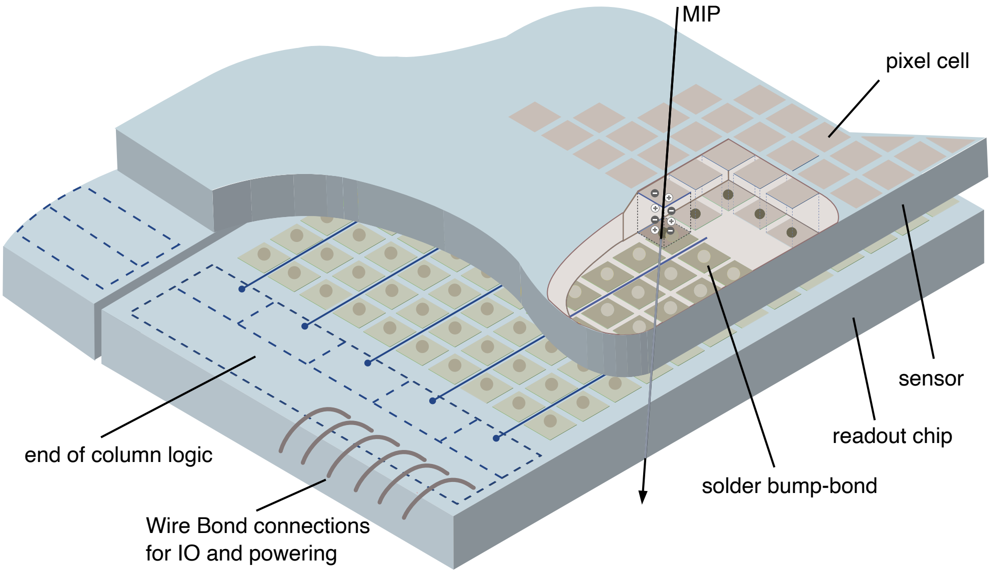

Figure 6.1: Hybrid detector concept: The pixelated sensor on the top is connected to the readout chip on the bottom via bump-bonds, fine-pitched solder bumps, connecting each pixel individually. Based on [138, Fig. 2.25].

A fully-equipped and operational IBL double-chip module (DC module), in the following also simply referred to as *module*, is depicted in Figure 6.2. Two front-end chips are thinned to 150 µm, connected to the sensor by bump bonding, and a flexible, printed circuit board (short: flex PCB) is glued on the top of the module, i.e. on the sensor backside. Via wire bonds, the flex establishes the interface to the module, providing power as well as data in- and output to the front-ends and high voltage to the sensor.

6.1.1 The FE-I4 readout chip

The ATLAS IBL readout chip, called Front-End I4 (FE-I4), was developed to cope with the high demands on occupancy, readout frequency and radiation hardness close to the interaction point at ATLAS. These requirements however make the chip versatile in application, and it has been used in different experiments [143–146]. The chip features 80 columns and 336 rows of pixels with an independent readout circuitry and a pixel size of $250 \times 50\,\mu\text{m}^2$. The overall chip size is $2.02 \times 1.88\,\text{cm}^2$ and the active area corresponds to 89 % of the chip area [147, p. 25]. The chip can cope with hit rates of up to $400\,\text{MHz/cm}^2$ without significant data loss ($< 1\,\%$) and trigger rates of up to 200 kHz [147, p. 10].
The pixel electronics can be subdivided in analogue and digital circuits. The analogue circuit

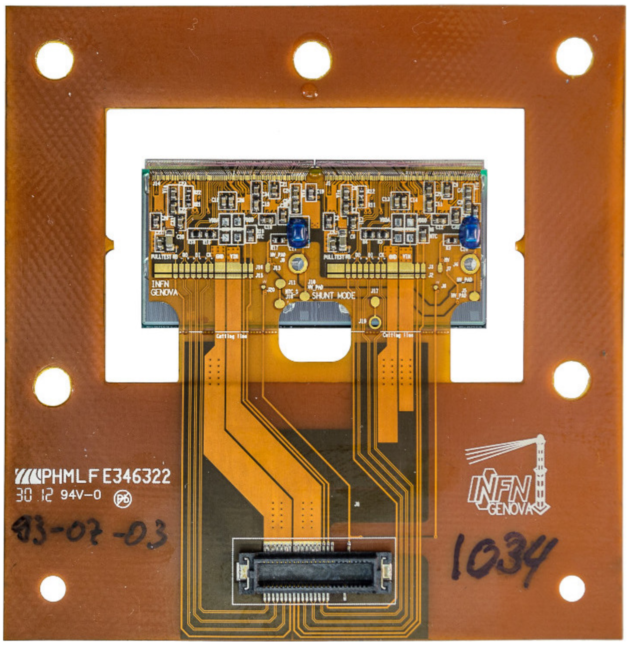

Figure 6.2: An ATLAS IBL DC module with one full size, planar sensor connected to two readout chips [142]. The flex PCB is glued on top of the sensor and electrically connected to the readout chip via wirebonds. The handling frame around is to be cut to shape prior to assembly inside a detector system.

amplifies and shapes the signal, while the digital logic is for data processing. Figure 6.3a shows the analogue circuit of one pixel. The amplification chain consists of a two-stage charge-sensitive amplifier (CSA), followed by a comparator which discriminates the input signal against a chosen threshold voltage. For the first stage of the CSA the shaping time, and for the comparator the threshold voltage, can be tuned per pixel. Via the `HitOut` the signal is fed to the digital processing line, where registered hits are buffered and attributed with a pixel address and a timestamp.

The signal shapes after CSA and comparator are shown in Figure 6.3b: The CSA integrates the current induced at the collection node and creates an output voltage proportional to the input charge. The constant current feedback provides a descending slope of the signal which is independent of the signal height. The comparator output is high as long as the input signal is larger than the chosen threshold voltage. The resulting Time-over-Threshold (ToT) at the output is consequently proportional to the collected charge. The finite rise time of the CSA signal can lead to different hit timings for different signal height: The lower the input signal, the later the threshold is crossed, delaying the comparator output. This delay is called time walk. If the time walk is large enough, the hit timing is different from the trigger timing, and hits with an amplitude close to the threshold might not be

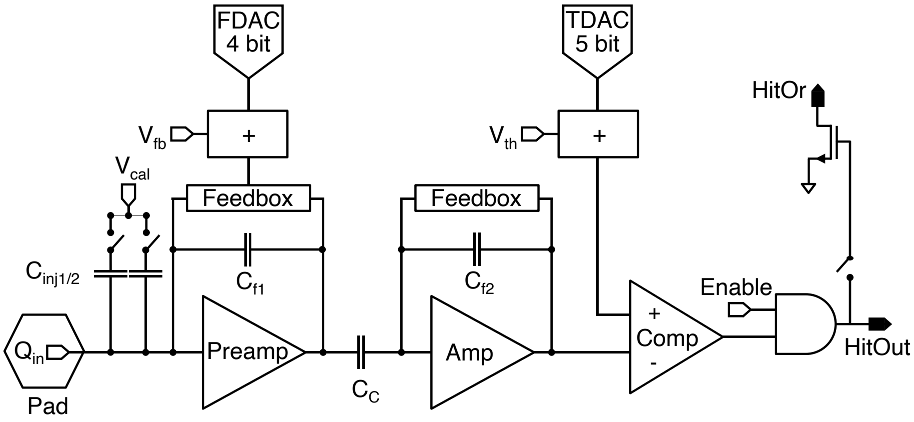

(a) Analogue circuit of one FE-I4 pixel, built from two AC coupled CSAs (*Preamp* and *Amp*), a comparator (*Comp*), the charge injection circuit V_{cal}, tuning circuit for the shaping time (V_{fb}, FDAC), and the threshold tuning (V_{th}, TDAC). The `HitOut` terminal connects to the digital circuit for further processing. The `HitOr` terminal provides access to a common analogue output of all discriminators on the front-end. Based on [147, p. 26]

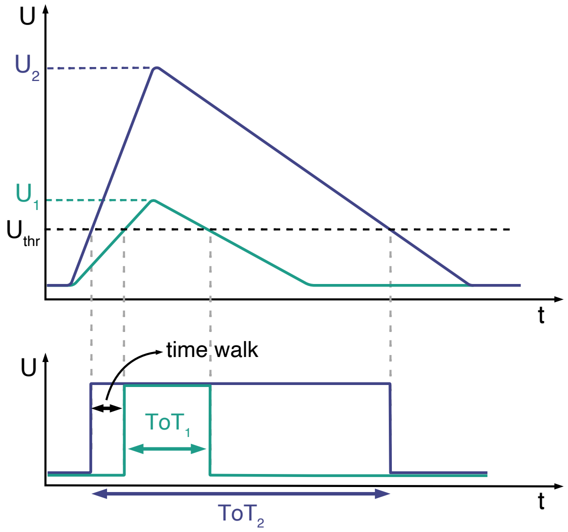

(b) Sketch of CSA and comparator waveforms for two different charges at the input. Top: The CSA output signal is higher for a larger amount of collected charge ($U_2 > U_1$). Bottom: The constant discharge current results in a longer discriminator output ($\mathrm{ToT}_2 > \mathrm{ToT}_1$). A charge close to the threshold delays the output of the discriminator with respect to a higher signal. This time difference is called time walk.

Figure 6.3: Analogue equivalent circuit of a FE-I4 pixel (a) and illustration of the ToT scheme (b).

read out. To minimise time walk, a short CSA rise time and a fast discriminator are necessary [148, p. 141].
For digitisation, the ToT signal is sampled with the front-end clock of 40 MHz and the collected charge is then measured in number of clock cycles. The ToT register of the FE-I4 offers 4 bits, corresponding to ToT values of 0 to 15. The digital circuit is realised as a 4-pixel digital region, where four pixel cells share a common digital logic. The registered ToT values are stored in memory together with the time of arrival and only if a trigger is received within a chosen time window, the data is read out, otherwise it is discarded. Barbero et al. provided a detailed description of the digital pixel logic [149].

6.1.2 The IBL pixel sensor

The planar sensors produced for the ATLAS IBL modules are n^+-in-n with a p^+ implant at the backside, surrounded by 13 guard rings [150] to prevent high electrical fields at the sensor edge [151, p. 82]. The pixel modules used for this work are double-chip modules where one large sensor is connected to two independent readout chips. The sensor therefore has 180 columns and 336 rows of pixels. To allow for the gap necessary between the two front-end chips the two central pixel columns are elongated and are 450 µm wide each. The two outer columns are elongated to 500 µm, as visible in Figure 6.4, to create an active area as large as possible [152, p. 11 ff]. For the IBL production, sensors were thinned to 200 µm while in a subsequent backup run sensors were thinned to 250 µm. While modules equipped with sensors of both thicknesses were used in this work, the different sensor thickness does not affect the hit detection capabilities since there was no substantial radiation damage. In the n^+-in-n design the depletion zone grows from the p^+ implant on the backside towards the single pixel implants on the top (see Figure 5.5). This means that the sensor needs to be operated fully-depleted in order to collect the full signal charge at the pixel implants.

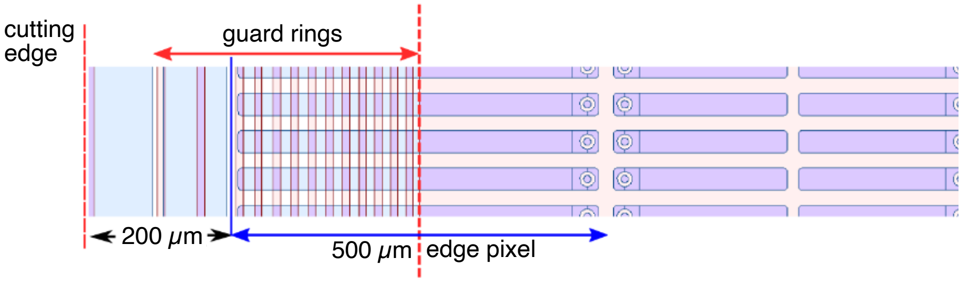

Figure 6.4: Edge design of the planar IBL pixel sensor. By placing guard rings on the backside, effectively overlapping with the elongated edge pixels, the inactive edge has been reduced from 1100 µm to 250 µm. From [141, p. 15].

6.2 Detector setup

To build the tracking detector for this work, twelve operational ATLAS IBL double-chip modules were procured. The limited number of modules makes it necessary to compromise between tracking performance and active area. For the event-integration, the pointing resolution of the pixel tracker towards the ECC is of utmost importance, while at the same time a reasonably large active area is necessary to offer an acceptance sufficient to make use of the spectrometer.

In the chosen layout, both parameters are accounted for by building six planes of two double-chip modules each, and rotating every second plane by $\pi/2$ around the beam axis. The rotation compensates for the much larger pixel pitch in x (250 µm compared to 50 µm in y) such that three high resolution measurements are possible for each dimension, Figure 6.5 shows an illustration. To maximise the solid angle coverage, the six planes are placed as close as possible to the moving ECC. In this configuration the cross section of the detector towards the target is approximately 11.3 cm^2 and the distance between first and last plane of the detector is approximately 13 cm. The solid angle coverage in this setup is $\theta_{\text{pix}} = 210$ mrad, 150 mrad in the x and y dimension each. The z-positions of single planes can be freely adjusted up to a total detector length of approximately 25 cm, associated with a lower solid angle coverage.

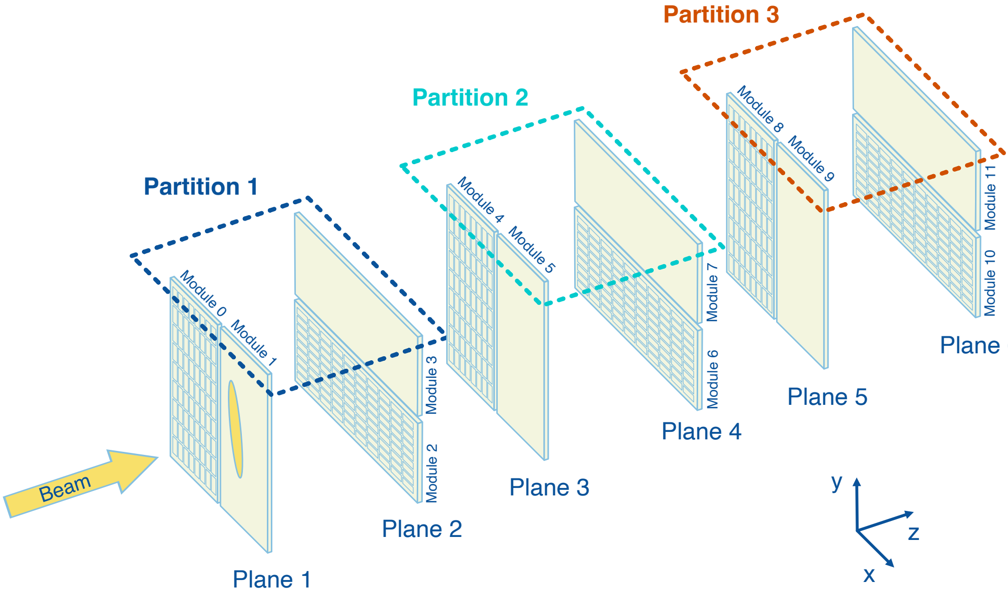

Figure 6.5: Spatial and logical orientation of the individual detector modules. The yellow ellipse indicates the proton beam. One detector plane is made of two modules and two consecutive planes build an independent readout partition, as indicated by the dashed frames. The sensor pixel matrix indicates the modules top side. The modules with pixel matrix (even numbers) are oriented in upstream direction, where no pixel matrix is visible (odd numbers) the module is oriented in downstream direction.

The mechanical support structure has to meet two opposing demands: The material budget introduced should be as small as possible to not interfere with spatial and momentum measurements, and at the same time the detector modules need to be held in place and cooled. To minimise the material budget, the mechanical support was made from aluminium frames with a cut out of 37 mm × 33 mm over which two modules are placed, one on the upstream side and one on the downstream side of the aluminium frame. In this setup the modules overlap in the $x - y$ plane by approximately 300 – 1000 µm. Thus, an overlapping active area is realised without introducing additional passive material. Three edges of each front-end backside, which overlap by approximately 1 mm with the frame, are glued on to the aluminium with thermal conductive glue. Figure 6.6 shows a photograph of the pixel tracker without front and back cover in the upstream view. The first module points towards the camera. Through the cutout of the frame the unprocessed backside of the second module can be seen. In this setup, the modules are arranged in four different spatial orientations (see Figure 6.5).

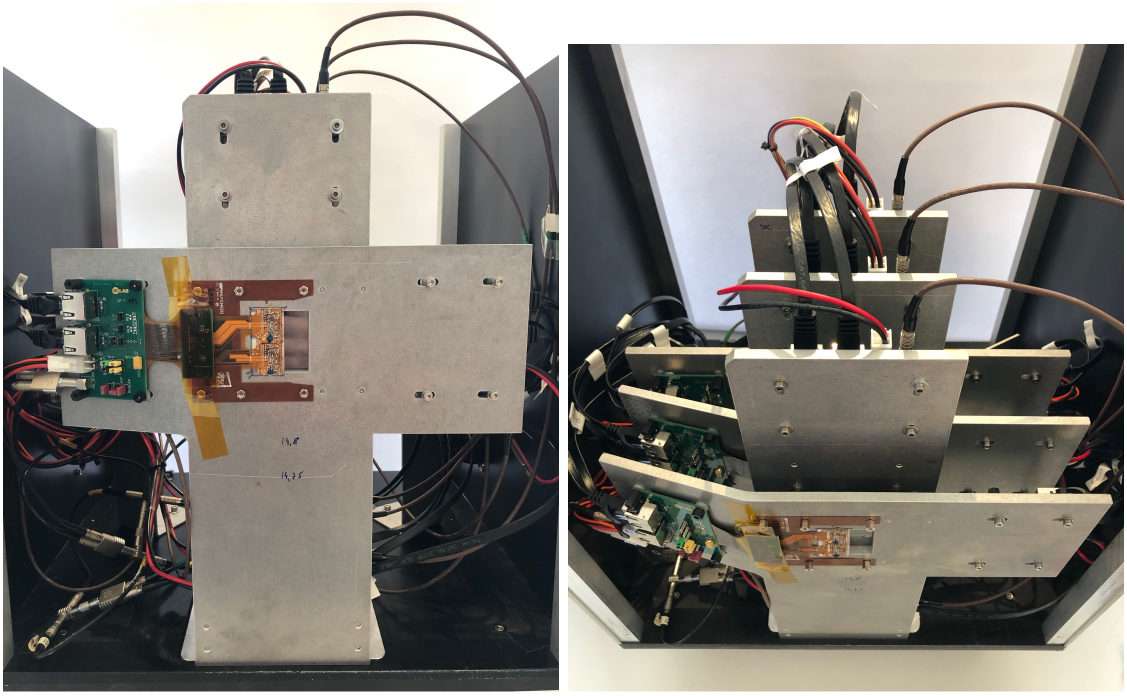

Figure 6.6: The uncovered pixel tracker for SHiP−charm from the front (left) and from above (right). The most upstream module is visible in the front, followed by the subsequent planes. The different orientation of modules can be distinguished by the direction of the service cables.

In operation, one module uses about 2 W of power. While the front-end chip can be operated at higher temperatures, without cooling the sensor is heated up, which can lead to thermal runaway (see Section 5.2.2). To prevent this, a cooling concept was developed and implemented in the mechanical support structure. The ground plate of the mechanical support structure is equipped with a cooling channel and kept at 12 °C with a circulating cooling fluid. By thermal contact to the ground plate the 5 mm thick aluminium frames can dissipate sufficient heat to keep the sensors from thermal runaway and the front-end chips operational.

The whole setup is covered by a box of aluminium plates to shield the detector from light and dust. Where the modules are located a beam entry and exit window is cut in the front- and backplate and covered with a 110 µm thin, light-tight Kapton foil.

6.3 Data acquisition

The twelve double-chip modules correspond to 24 logically-independent readout channels, each with a dedicated data connection. For integration of the pixel tracker in the SHiP–charm experiment an existing laboratory readout system, consisting of the *MMC3* readout board (see Figure 6.7) and the *pyBAR* readout software [153], was adapted, and the *pyControlHost* software was written to accept commands from and send interpreted data to the experiments' DAQ server, where the DAQ is realised with the *ControlHost* software [154].

6.3.1 Readout hard- and software

The FE-I4 is operated via pyBAR, a readout software written in Python, developed for single and multi-chip module characterisation. Integrated in pyBAR are asynchronous on- and offline data interpretation, as well as network publishing. The latter feature is important for the communication of the pixel tracker with the central DAQ. The interface between front-end and software is provided by the MMC3-board, a field-programmable gate array (FPGA) based readout board, developed at Bonn University. The firmware for the FPGA is based on the *basil* framework [155]. The MMC3-board offers connectivity for up to eight front-end chips via ethernet, as well as analogue in- and output via coaxial *LEMO-00* connectors, short LEMO.

For SHiP–charm, certain modifications of the existing readout hard- and software are necessary. To comply with the central DAQ, three Transistor-transistor logic (TTL) signals have to be accepted and processed (SoS, CLK, trigger) and the BUSY signal has to be provided via TTL to the central trigger logic (see Section 4.2.5). To realise a third TTL input, a customisable DOT PCB, also called Perfboard, with a LEMO input and a termination resistor is connected to the peripheral module interface (Pmod) connector. The FPGA firmware is modified to accept the third input signal, which resets the timestamp, and to set the BUSY output according to the readout status.

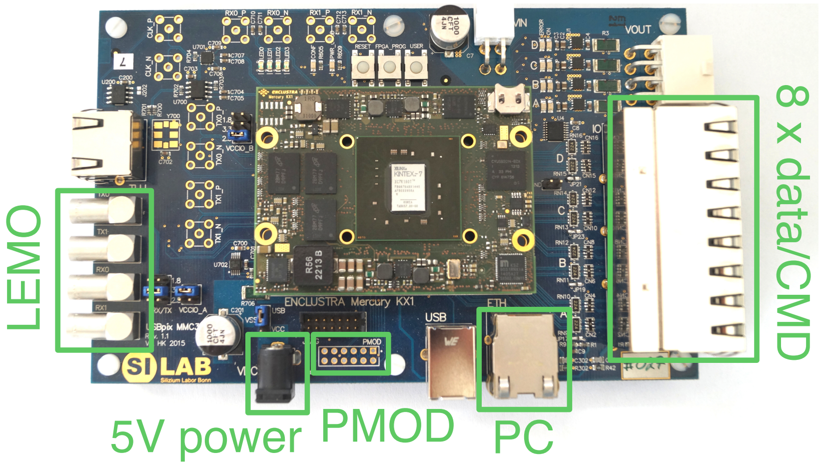

Figure 6.7: Top view of the USBpix MMC3-board. In the centre of the board the commercial Xilinx Kintex 7 FPGA is visible, providing the interface between detector and readout software. The LEMO ports offer two analogue in- and outputs, and are designed to work on TTL logic levels. The connection to the PC as well as to the single front-ends are realised via Gbit ethernet. The Pmod connector can be used to extend analogue in- and output capabilities.

The FPGA firmware consists of two major parts: The FE-I4 firmware module for front-end communication and data interpretation, and one module for trigger logic and timestamping. Figure 6.8 shows a simplified block diagram of the FPGA firmware implementation. The modules are described below:

Command signal generator (`CMD`): This part of the FE-I4 firmware module translates software commands to the respective chip register values and creates a command stream, which is sent to the front-end.

Clock (`CLK`): The FE-I4 chip does not have a clock generator, so the chip clock has to be provided externally. Usually the signal of a clock generator on the FPGA board is used to generate the 40 MHz signal. For the SHiP−charm experiment, three independent hardware instances have to be synchronised, thus, an external clock generator was used, feeding a synchronous clock signal to all three MMC3-boards.

Data receiver (`DATA`): Each front-end chip sends a 160 MHz data stream of trigger and hit words on a differential pair transmission lines, encoded in an 8bit-10bit data format. The data receiver decodes the 8bit-10bit format and ensures a permanent link of the readout hardware to the front-end.

Arbiter Unit (`ARU`): Several data streams arrive at the FPGA and have to be written to the same memory. The Arbiter Unit processes these data streams, the trigger words from the Trigger Logic Unit (TLU), as well as the hit and trigger data from the front-ends, sending a single data stream to the first-in-first-out (FIFO) stack. To ensure proper event reconstruction, trigger words are always prioritised over read out data.

First-In-First-Out stack (`FIFO`): This memory is buffering readout data, in case the Transmission Control Protocol (TCP) transfer to the PC is pending.

Trigger Logic Unit controller (`TLU`): This general-purpose trigger module enables synchronisation of different detectors and hardware instances, by accepting external triggers and sending out acknowledge and BUSY signals. The trigger format can be chosen between monotonically increasing trigger numbers, or timestamps increasing with the front-end clock of 40 MHz. For SHiP–charm the TLU module [153; 155] was modified to allow a 64-bit timestamp counter, as well as to accept the SoS signal for resetting the timestamp.

The adapted readout software and firmware are available on GitHub [156].

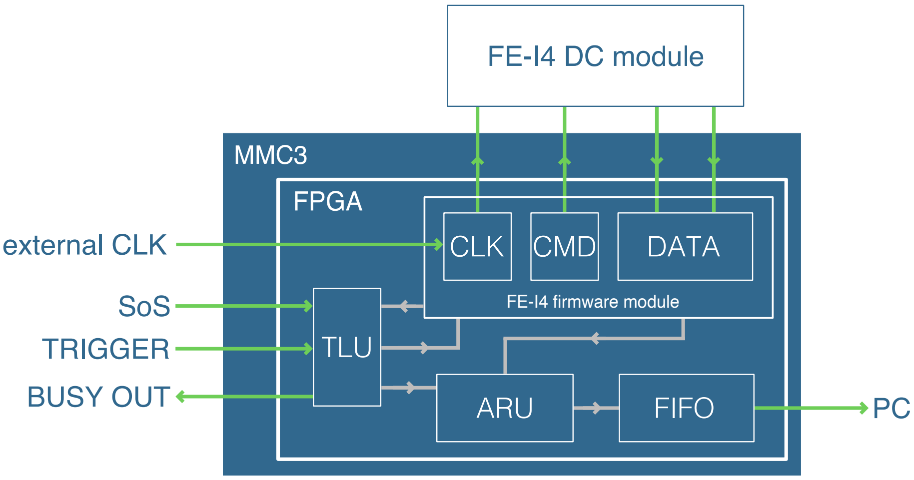

Figure 6.8: Simplified block diagram of the FPGA firmware modules. The in- and output signals are indicated in green. To synchronise the three detector partitions an external clock is fed to the MMC3-boards.

Each pixel detector module consists of 53 760 readout channels, and with twelve modules the detector offers a total of 645 120 channels. To represent all channels with unique IDs the pixel tracker is logically and physically operated in three independent *sub-partitions*, i.e. one for every MMC3-board, albeit connected to the same readout PC. Figure 6.9 visualises the setup: The three sub-partitions receive the same input signals, and all transmission lines are matched for signal propagation time. The partitions are also independently controlled by the ControlHost framework and three independent instances of pyControlHost and pyBAR are run on the host PC. The data is then merged during reconstruction and analysis. Each partition is identical in the way that all partitions have the same number of modules and the spatial orientation of individual modules is the same in all sub-partitions. In this setup the SHiP−charm pixel tracker is the largest operational FE-I4-based detector besides the ATLAS IBL.

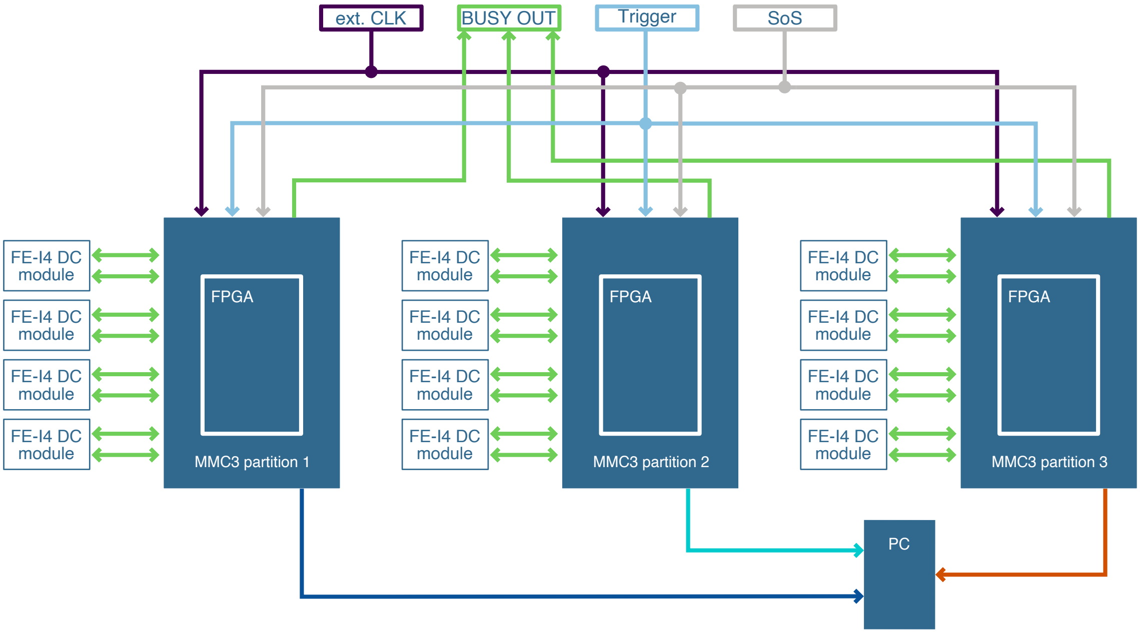

Figure 6.9: Visualisation of the data flow in the SHiP−charm pixel tracker. The three sub-partitions operate independent of each other, but receive the same, synchronous hardware signals. The lengths of lines in the picture are not to scale. In fact, the length of the transmission lines is matched, which is particularly important for the synchronous distribution of the external clock.

6.3.2 PyControlHost

Apart from processing the hardware signals, the pixel detector DAQ software has to communicate with the ControlHost server of the central DAQ. ControlHost uses a publisher-subscriber approach, where all sub-detector DAQs subscribe to the central DAQ. For the pixel tracker this is realised via the pyControlHost package [157], an interface between pyBAR and ControlHost. It accepts commands from the ControlHost instance of the central DAQ, and issues commands to pyBAR accordingly. PyBAR data is converted to a format compatible with the event builder and sent out to the ControlHost server.

Figure 6.10 shows a block diagram of the software framework as implemented for the pixel tracker in SHiP–charm: The ControlHost instance receives the SPS hardware signals (SoR, SoS, EoS, End of Run (EoR)) and sends out software commands (`RunStart`, `StartSpill`, `EndSpill`, `EndRun`). These commands are received by pyControlHost, and the respective actions are triggered:

- **`RunStart`:** The hardware is reset and configured for data taking. A new raw-data file is opened, the detector is awaiting trigger and ready to be read out.
- **`StartSpill`:** The trigger time stamp is reset.
- **`EndSpill`:** Data is interpreted, published to pyControlHost, translated to the ControlHost dataformat and sent to ControlHost.
- **`EndRun`:** The data taking is stopped regularly, the raw-data file is written to disc.

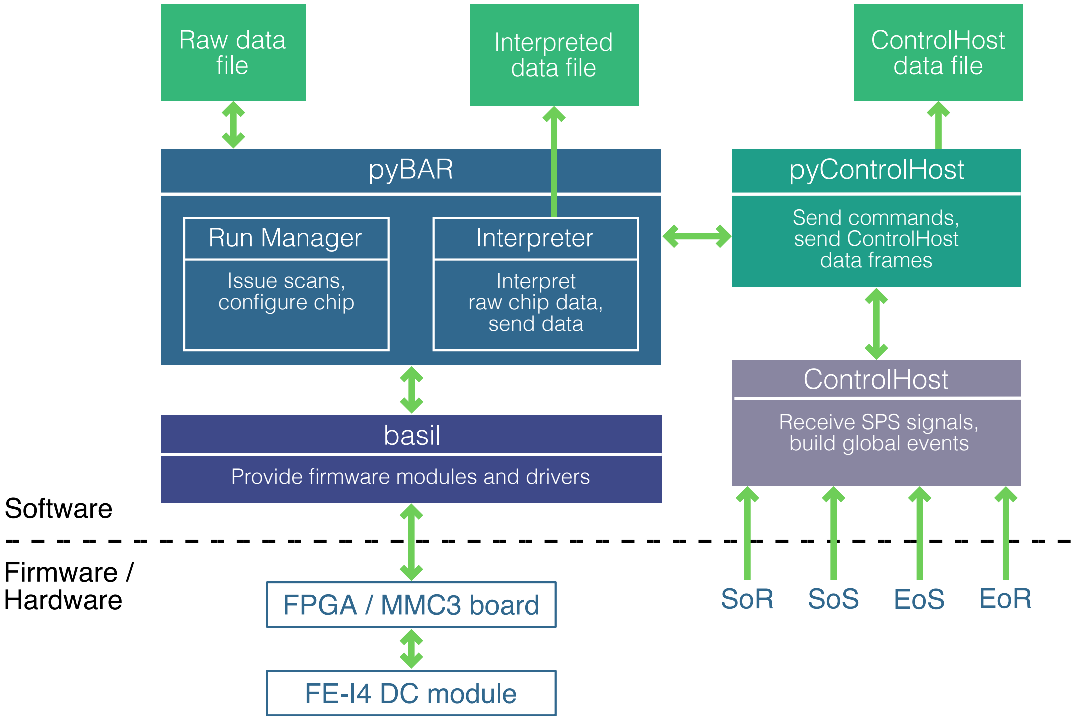

Figure 6.10: Block diagram of the DAQ software framework, used in the SHiP–charm experiment. PyControlHost acts as an interface between the existing laboratory readout system (pyBAR and basil on the left), and the ControlHost experiment DAQ. Not only is the interpreted data saved for later standalone analysis, also the data frames sent to ControlHost are saved in the respective format.

Two additional signals are used for slow control: `Stop` and `RunStart`. `Stop` interrupts data taking of pyBAR as well as sending data to the central DAQ immediately. The system is then restarted and awaiting `RunStart`. `Enable/Disable` starts/stops data conversion and sending of data frames.

The ControlHost server expects a unique identifier for every readout channel of the subscribed detector. The structure is based on single spills, every spill is identified by the SoS header, followed by the event frames. The data format is shown in Figure 6.11.

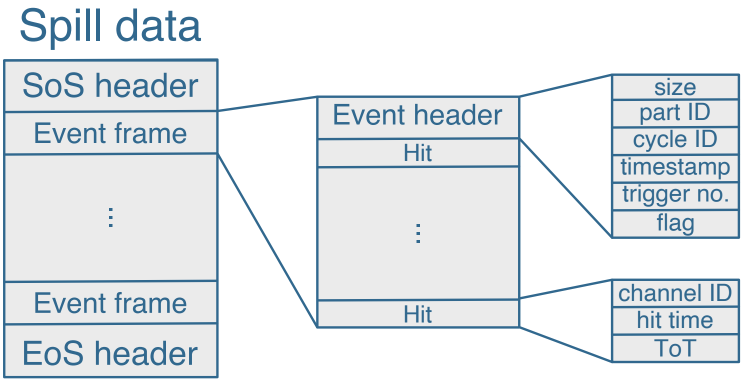

Figure 6.11: Visualisation of the data format sent to ControlHost. The data from one complete spill is sent after the `EndSpill` signal. The spill data frame consists of a header, followed by an individual frame for each event. The event frames begin with a dedicated header, containing information regarding the number of hits and unique event identification, followed by the registered hits. The hit data finally contains the unique channel ID, the timing relative to the trigger, and the ToT information.

For every trigger, an event frame consisting of a header with trigger number and timestamp, as well as the detector ID is sent, followed by one data word of up to 6 byte for every registered hit. The detector ID identifies the individual front-ends in the respective partition and runs from 0 to 7. The first 2 byte of the hit word are available for the unique channel ID, which runs from 0 for the lower right pixel of a single front-end up to 26879 for the upper right pixel. The second 2 byte decode timing information relative to the trigger. The pixel detector can not measure the hit timing relative to the trigger, so this is set to 0. The last 2 byte are optional and used for the ToT information of the hit[1]. The spill data is concluded by the EoS header, containing the total number of sent event frames.

---

[1] An implementation of the data format in C++ is shown in Listing 1 in the Appendix.

7 Track reconstruction and matching

As discussed in Section 4.2, the assignment of timestamps to ECC vertices is crucial for event reconstruction in SHiP− charm. Besides the momentum measurement with the spectrometer, particles and the corresponding trajectories have to be assigned to a vertex in order to identify the types of reactions and processes. The spatial and timing resolution of the pixel detector[1] allows for accurate track reconstruction and projection towards the ECC, and therefore linking vertices and timestamps. In order to do so, the data taken by the pixel detector is reconstructed to tracks (and vertices) independently, as is the data in the ECC. The two track sets are then matched in a dedicated track matching procedure. While in this chapter all aspects of the pixel detector track reconstruction and performance, as well as the alignment and matching of the two sub-detectors is discussed, the reader is kindly referred to the existing literature [46; 115; 158] for information about the ECC track and vertex reconstruction. The chapter is concluded by an estimation of the matching rate as function of the particle momentum.

7.1 Runs and beam conditions

For SHiP− charm the 400 GeV/c proton beam of the SPS is used. The beam is delivered in spills of approximately 4.8 s length while the beam intensity can be chosen by the user. For SHiP− charm an average intensity of 10 kHz was chosen to meet the occupancy limit of the ECC. Six target configurations with a thickness between 0.16 and 1.6 nuclear interaction lengths were implemented and named *CHARM 1* to *CHARM 6*. Table 7.1 lists all configurations and important features. The ECC for one run, CHARM 1 run 6, was realised with tungsten sheets instead of lead to simulate the actual SHiP target as accurately as possible. With 1.56×10^6 PoT approximately 3 % of the planned final dataset was collected in the optimisation run.

For a maximum yield of the ECC surface, the SPS beam was tuned to an elliptical shape, as visible on the left in Figure 7.1. Further analysis showed that the elliptical beam shape

---

[1] For a detailed discussion on the pixel detector the reader is kindly referred to Chapter 6.

	runs	passive material	ECC	films	integrated p.o.t. $\times 10^5$
CHARM 1	6	–	28 mm Pb/W + 29 films	174	5.4
CHARM 2	6	28 mm Pb	28 mm Pb + 29 films	174	5.2
CHARM 3	3	56 mm Pb	56 mm Pb + 57 films	174	1.0
CHARM 4	3	113 mm Pb	56 mm Pb + 57 films	171	0.8
CHARM 5	3	168 mm Pb	56 mm Pb + 57 films	171	1.6
CHARM 6	3	224 mm Pb	56 mm Pb + 57 films	171	1.6
Total	24			1032	15.6

Table 7.1: Configurations for the different CHARM runs, showing the number of runs taken, the amount of passive material in front of the ECC, the ECC composition, the number of films and the integrated PoT. The passive material employed in the ECC for CHARM 1 run 6 is not lead but tungsten sheets.

is actually a superposition of a circular beam spot moving over the period of one spill, as can be seen on the left in Figure 7.1. To determine the beam spot position, a run of primary protons was analysed. Every spill recorded is split into 14 time frames and the mean of all cluster positions on the first pixel detector plane (modules 0 and 1) within a time frame is calculated. The beam was centred on the right pixel detector half since one of the front-end chips on the left half of the tracker stopped functioning during data taking. In addition to the physics runs, data was recorded to align the sub-detectors and to integrate them with the DAQ. The central DAQ data is not available at the time of writing, and so this study is performed on the datasets recorded independently by the pixel detector and the emulsion detector, respectively.

7.2 Track reconstruction

The first step towards integration of the pixel detector with the ECC is a stand-alone track reconstruction in the pixel detector. The traversing particle's trajectories, short tracks, can be reconstructed from the single hits created in every passed detector layer. While in general at least two hits are necessary to define a straight line, for accurate trajectories more measurements are desirable. The reconstruction is performed in four distinct steps,

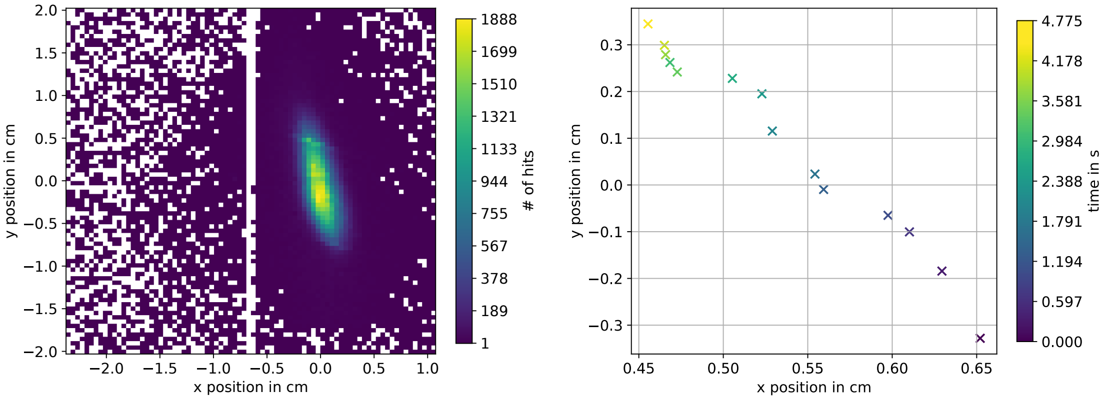

Figure 7.1: Reconstructed cluster centres on the first plane of the pixel detector for a primary proton run (left). The elliptical beam shape is visible. The coordinate system is aligned to the beam centre. Beam centre as a function of spill time for a primary proton spill (right). The colour codes the time relative to the SoS signal. A beam centre drift towards the upper left is visible.

which are first briefly summarised, while more detailed discussions of the track finding and fitting algorithms follow in Section 7.2.1 and Section 7.2.2:

Clustering: The binary hit information provided by the front-end only roughly represents the actual particle path. As discussed in Section 5.2, charge carriers are created over the whole sensor thickness, forming a charge cloud. Should a particle have a large angle relative to the sensor surface, or simply impinge on the border in between pixels, the charge cloud can be registered by several pixels, for extreme angles even by several tens of pixels. To represent the single hit in data, clustering is performed on the raw hit data. Neighbouring single pixel hits are combined to a common cluster with a charge-weighted cluster centre $\overline{x}$ for each dimension:

$$\overline{x} = \frac{\Sigma_k \, q_k \cdot x_k}{\Sigma_k \, q_k} \, . \tag{7.1}$$

Where x_k is a single pixel hit position and q_k the respective registered charge. The clustering of single pixel hits also improves the effective hit resolution [159]. At very high occupancies, clustering of hits can also be misleading, when in fact independent single pixel hits are clustered. For physics runs in SHiP−charm, occupancies of more than 1000 hit pixels on one double chip module were recorded. Figure 7.2 shows the cluster sizes (left) and number of clusters per event (right) for CHARM 1 run 1. While the majority of clusters is composed of one or two hits, there is a long tail in the distribution. However, in a high-occupancy event, clustering hits to a single large cluster might not represent the actual particle interaction any more. It can be geometrically shown that clusters larger than 4 hits are not likely to originate in a single track from the ECC: The maximum angle $\theta_{x/y}$ under which particles from the ECC can pass all detector layers is 150 mrad in the x and y dimensions (see Section 6.2). At an incident angle of 150 mrad with respect to the sensor surface, particles travel a lateral distance of only 37 µm while traversing the sensor. Considering the pixel pitch of 50 µm × 250 µm, a lateral extent of the charge cloud in this order of magnitude can not result in clusters larger than four hits.

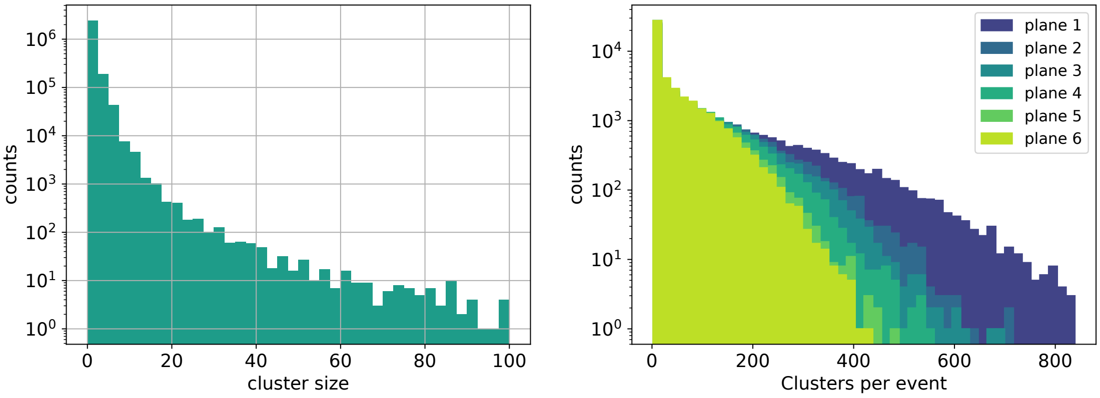

Figure 7.2: Cluster size (left) and number of clusters per event (right) for a run in CHARM 1 configuration.

Alignment: For a precise reconstruction of trajectories in space, the relative position and orientation of the single detector modules with respect to each other and to a common reference point has to be known. The alignment is the procedure of measuring these positions and orientations, and applying the correction to measured hit positions. For SHiP−charm a dedicated survey measured the pixel detector position relative to the beam with a precision of 500 µm by means of reference points on the outer detector cover [160]. Within the scope of the survey the positions of individual planes with respect to each other and to the reference point however could only be determined with lower precision. For accurate reconstruction, data from primary protons, i.e. events with only one track, is used. The presence of only one track makes unambiguous assignment of hits to this track straightforward. For the alignment a first set of trajectories is computed, and the deviation of each track to the measured hit positions, the residuum, is minimised by correcting the single module positions and angles.

Track finding: The single clusters on different detector planes have to be assigned to a track candidate, also called *track seed.* The high track multiplicity in events in SHiP−charm creates an environment where the correct assignment of clusters to tracks is not obvious. The challenge of optimal and unambiguous assignment of clusters to a track in high-occupancy events is met by a pattern recognition algorithm discussed in Section 7.2.1.

Track fitting: Once the clusters of a track are collected, the trajectory parameters, intersection at a reference point and direction, are determined in a χ^2 optimisation discussed in Section 7.2.2.

7.2.1 Pattern recognition

As described above, the assignment of hits to tracks is crucial for the correct reconstruction of events. It is even more important in case of events with numerous hits on every detector plane, where ambiguous track assignment is possible. For this study, a local pattern recognition approach was chosen, which relies on track seeds. For SHiP−charm, track seeds can be built from any two hits in the pixel detector, given the hits are on different planes. Figure 7.3 visualises the track seed and the pattern recognition algorithm. A track seed is computed as a straight line between two chosen hits. Around the seed position a region of interest (ROI) with the shape of an elliptical cylinder is calculated, where the lengths $a, b = 2\,\sigma_{x/y}$ of the two axes correspond to the uncertainty in the track seed position on any given plane in the respective dimension:

$$\sigma_{x/y} = \sqrt{\sigma^2_{\mathrm{proj},x/y} + \sigma^2_{\mathrm{cl},x/y}}\,, \tag{7.2}$$

where σ_{cl} is the uncertainty on the cluster centre position of the hit under investigation, and

$$\sigma^2_{\mathrm{proj}} = z^2 \cdot \sigma^2_{\mathrm{slope}} + \sigma^2_{\mathrm{pos}} + 2z \cdot \sigma_{\mathrm{slope/pos}} \tag{7.3}$$

is the uncertainty of the actual projection of the track seed position on the detector plane under investigation, with σ_{slope} the uncertainty on the track seed angle, σ_{pos} the uncertainty on the track seed position, $\sigma_{\mathrm{slope/pos}}$ as covariance of both, and z the distance to which the track seed is extrapolated. The cylinder width is chosen to be $2 \cdot \sigma_{x/y}$ to account for multiple scattering and other sources of deviation of the particle trajectory from a straight line.

Optimal performance is achieved, if the third and last detector plane are chosen for track seeds. This way, only tracks are reconstructed which leave the pixel detector and propagate towards the second half of the spectrometer. While track seeds from the first and last

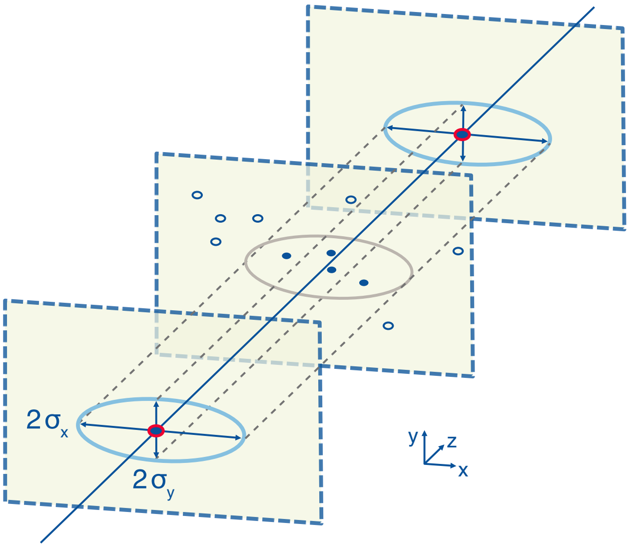

Figure 7.3: Sketch of the elliptic cylinder built around one hit on the first and one hit on the last plane (marked red), defining a track seed (solid blue line). The hits on the central plane are fed to the pattern recognition algorithm. Cluster centres are represented by the small dots, full dots correspond to clusters considered for the track fit, empty dots are discarded for their distance to the track seed.

detector planes are more precise, electromagnetic showers from secondary interaction in the target create numerous hits on the first plane, which do not lead to promising track seeds. The algorithm can also restrict track seeds to a maximum opening angle θ in order to only create seeds which will point towards the acceptance region of subsequent detectors. The solid angle coverage of the pixel detector is $\theta_{\text{pix}} = 210\,\text{mrad}$, while the SciFi detector downstream offers $\theta_{\text{SF}} = 62\,\text{mrad}$. The above selections reduce the computation time without impacting the event reconstruction performance.

Furthermore, the algorithm only considers clusters with up to four hits. In every given event a new track seed is created for all combinations of hit pairs on the chosen seed planes within above requirements[2]. Every hit on the remaining planes within the projected cylinder is considered for the fit. If not stated otherwise, six hits have to be assigned to a track seed for it to be considered for a track fit, at least one hit per detector plane.

7.2.2 Track fitting

Finding the actual trajectory from the collection of track seeds and assigned hits is an optimisation problem which can be solved by a least squares estimation, assuming inde-

---

[2] The pattern recognition can assign the same hit to different track seeds. This ambiguity is resolved during the track fit, discussed in the following section.

pendent Gaussian distributed measurements. While the exact trajectory is not necessarily found, the fit converges to the closest parameterisation, considering the uncertainties. In the following, this well known procedure is briefly introduced.

Assuming the track is a straight line in three dimensions, $1 \leq k \leq 3$ is indexing these dimensions and $1 \leq i \leq N$ indexes the number of measurement points for a track. The vector $\boldsymbol{y}$ contains the measured intersection coordinates, and λ is the expected intersection coordinate considering the track parameterisation $\boldsymbol{\alpha}$. The track χ^2 can then be written as

$$\chi^2 = \sum_{i,k} \frac{(y_{i,k} - \lambda(x_{i,k}; \boldsymbol{\alpha}))^2}{\sigma_{i,k}^2} . \tag{7.4}$$

Where

$$\boldsymbol{\alpha} = \begin{pmatrix} x \\ y \\ \theta_{xz} \\ \theta_{yz} \end{pmatrix} \tag{7.5}$$

with x and y denoting the track intersection coordinates for a given z, and $\theta_{xz} = \mathrm{d}x/\mathrm{d}z$ and $\theta_{yz} = \mathrm{d}y/\mathrm{d}z$ denote the direction tangents. The χ^2 for every track seed is minimised using the Minuit 2 software package [161] as part of the ROOT framework [162].

For track seeds with one or more planes containing several qualified hits, every combination is fitted. A common measure for the goodness of a fit is

$$\chi^2_{\mathrm{red}} = \chi^2/\mathrm{ndf} . \tag{7.6}$$

The number of degrees of freedom (ndf) is calculated as difference of the number of input measurements and the number of fitted parameters and should be positive. Here for at least 6 clusters per track ($n_{\mathrm{cl}} \geq 6$) and four parameters fitted for each track

$$\mathrm{ndf} = (2 \times n_{\mathrm{cl}} - 4) \geq 8 . \tag{7.7}$$

The track with the hit combination leading to the smallest χ^2_{red} is selected and has to pass a $\chi^2_{\mathrm{red}} < 5$ requirement. Figure 7.4 shows the χ^2_{red} distribution and the number of clusters associated to each track for CHARM 1 run 6 with approximately 50000 events and 112000 reconstructed tracks. The χ^2_{red} distribution peaks around 1, as is expected for properly modelled measurement uncertainties. The two modules building a detector plane can overlap in such a way, that tracks can create more than six clusters in the detector.

The distribution of associated clusters per track in Figure 7.4 shows that the probability for a track passing overlapping modules in more than one plane is small.

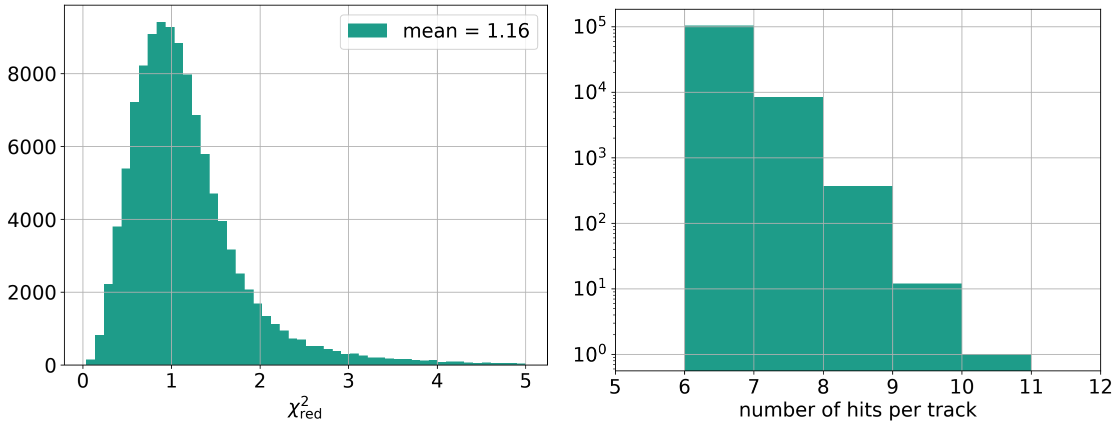

Figure 7.4: χ^2/ndf distribution (left) and assigned clusters per track (right) for fitted tracks in physics CHARM 1 run 6. Pixel modules can overlap, such that tracks passing the overlapping regions can have more than six true clusters.

7.3 Detector performance

To ensure the reconstruction quality, the overall detector performance has been investigated and the three aspects with the possibly largest influence on the performance are discussed in the following: noise of the modules, track reconstruction efficiency, and spatial resolution.

Noise and masked pixels

Within the scope of track reconstruction, hits registered coincidentally with a trigger, but not created by an actual particle interaction are referred to as noise. The largest source of detector noise lies in the analogue front-end electronics and can be strikingly reduced by tuning and equalising the response of the single pixels to the same amount of charge. During the tuning procedure, non-responsive and non-tunable pixels are disabled. Additionally, a dedicated noise tuning is performed to detect and disable pixels which fire without injected charge [138, p. 103]. The requirement for a pixel to pass the noise tuning is an occupancy without charge injection of 1×10^{-6} hits/trigger. After the tuning procedure less than 0.03 % of pixels on each module are disabled.

7.3.1 Residuals and hit-detection efficiency

The hit-detection efficiency of the IBL modules was thoroughly investigated during the ATLAS qualification process [141, p. 31]. Nevertheless, due to the complexity of this measurement, it is useful to determine the efficiency during the specific data-taking conditions of the testbeam and thereby verify the performance of the pixel tracker setup. Also, given a very high efficiency, it can be used to verify the other detectors of the SHiP–charm experiment. For a competitive hit-detection efficiency, the tuning, triggering, event building, and alignment need to work flawlessly for all detector modules. The hit-detection efficiency ϵ is defined as

$$\epsilon = \frac{n_{\mathrm{hit}}}{n_{\mathrm{track}}} \,, \tag{7.8}$$

where n_{hit} is the number of hits detected by the module under investigation, and n_{track} is the total number of tracks passing the module. The hit-detection efficiency is measured for each module individually on single track events from primary proton runs without ECC or passive material. To exclude noise hits, at most one hit is associated to the track if the residual is smaller than the association distance d_{assoc}.

For an unbiased measurement, the tracks are fitted without considering hits on the module under investigation, thus a new track set is fitted for the efficiency measurement of every single module. The distance between the intersection of the fitted track and the hit on the module under investigation is then called the *unbiased residual.* Figure 7.5 shows the unbiased residuals for module five. The module is oriented vertically, such that the x coordinate is measured with the short pixel pitch and y is measured with long pitch. Assuming negligible contribution of the reconstruction software, the width σ of the distribution is also the measurement resolution. In case of unbiased residuals it can be written as [163, p. 11]:

$$\sigma = \sqrt{\sigma_{\mathrm{int}}^2 + \sigma_{\mathrm{point}}^2} \,. \tag{7.9}$$

Here $\sigma_{\mathrm{int}} = p/\sqrt{12}$ is the intrinsic resolution of the measuring pixel with pitch p [122, pp. 300, 828], and σ_{point} is the pointing resolution of the detector, which depends on the relative distances of the planes, alignment, and multiple scattering. Depending on which of the two resolutions dominate, the shape of the residual distribution changes. A dominant intrinsic pixel resolution creates a box shape, which is the case for the long pixel pitch: The residual for any track pointing to a hit pixel of a single pixel cluster is calculated with respect to the pixel centre, resulting in a uniform distribution with maximum distance of $\pm p/2$. For the smaller pitch, the Gaussian distribution of multiple scattering (see Section 5.1.2) as well as misalignment dominate. The residual distribution for the long pixel pitch is thus fitted with a box-function convoluted with a Gaussian. The residual width is then the half width at half maximum (HWHM) of the fitted box function. It is worth to note, that for the vertically oriented modules the central columns with a long pixel pitch of 450 µm are at the centre of the beam spot. Therefore, the residual width is dominated by these pixels, see Section 6.2.

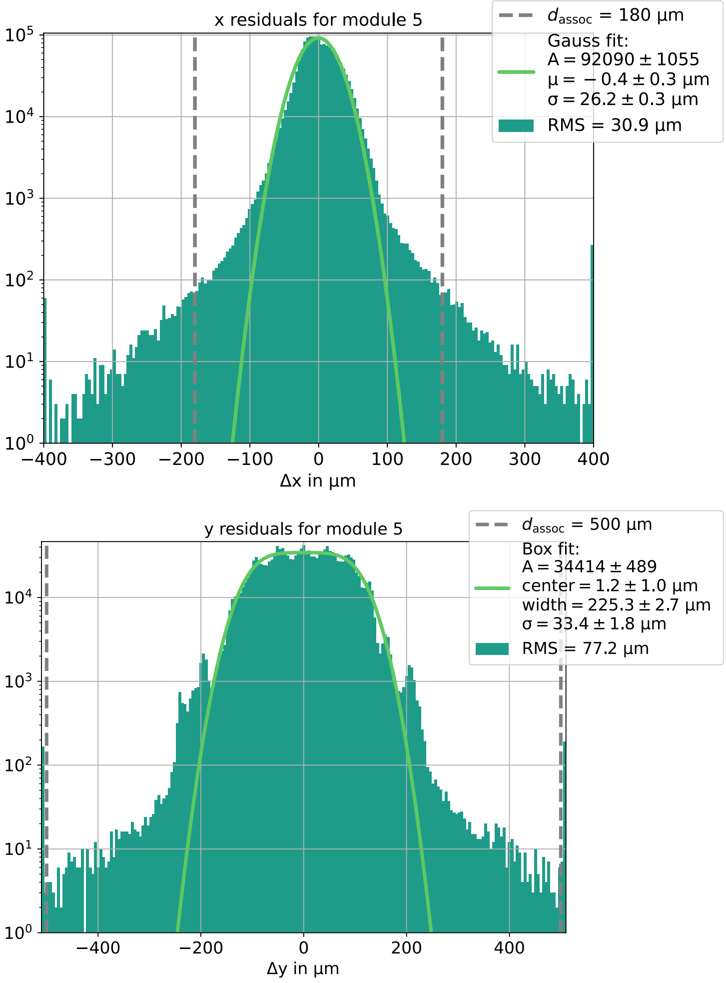

Figure 7.5: Residuals in x and y direction for a module of the central plane 3. The dimension with long pixel pitch (bottom, y-direction) is fitted by a box function convoluted with a Gaussian.

For residuals in the long pixel pitch, another effect can be observed: Due to the alternating orientation of the detector planes, the short-pitched planes create a substructure in the residuals for the long pitch. The long and short pitches have a ratio of 1:5 for the major part of the pixel matrix, and ratios of 1:9 and 1:10 for the two central and each of the edge columns, respectively. The more precise measurements from short pitches on the detector planes used for the track fit pull the track towards the small pitched pixel centres and therefore create the peaking structure observed in the lower plot in Figure 7.5. This effect has been observed before and is confirmed by simulation [145, p. 11].

Figure 7.6 shows the measured residuals for both dimensions and the hit-detection efficiency per module. As discussed, the efficiency is measured for single track events. As visible in Figure 7.1 the primary beam was shifted towards the right half of the detector. Thus, modules 0, 4 and 8 do not offer a sufficient amount of data for an efficiency measurement and are therefore omitted. For the remaining modules the efficiency is well above 99.6 % and comparable to existing measurements [141, p. 31].

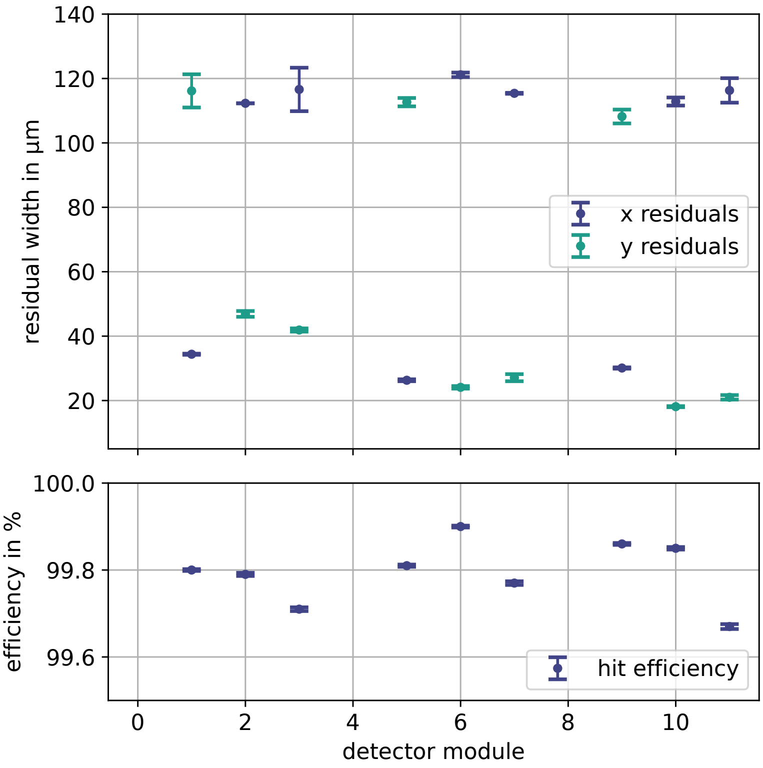

Figure 7.6: Residuals and hit-detection efficiency per detector module for primary protons in single track events. All modules investigated show an efficiency well above 99.6 %. Modules 0, 4 and 8 were not directly illuminated by the beam, thus there is insufficient data for an efficiency and residual measurement.

Statistical uncertainty

A detailed discussion on the uncertainty in the hit-detection efficiency is provided in Ref. [138, p. 79 ff]. The statistical uncertainty can be computed with Bayes' theorem and depends on the number of reconstructed tracks and the measured efficiency [164; 165].

Since the number of tracks is in the order of 10^6 and the measured efficiency is close to 100 % the statistical uncertainty is smaller than 0.006 % and therefore negligible.

Systematic uncertainties

There are various contributions to the systematic uncertainty in the hit-detection efficiency and the determination of their magnitude is not trivial. While a detailed analysis is provided in Ref. [138, p. 81 ff], the most important effects for this study are listed in the following.

Increase n_{track}: Building fake tracks leads to an overestimation of the number of reconstructed tracks, which consequently leads to an underestimated efficiency. Choosing a tight χ^2_{red} cut reduces the probability of fake tracks. The variation in the measured efficiency for different χ^2_{red} was below 0.007 %. For this analysis a requirement of $\chi^2_{\mathrm{red}} \leq 2.09$ is chosen, corresponding to a p-value close to 0.05.

Decrease n_{track}: If true tracks are not reconstructed, the efficiency can be overestimated when in the same event a hit on the module under investigation from a not reconstructed track is associated to another track. This effect can be reduced by a strict d_{assoc} or by a cut on the allowed number of tracks in an event. Since only events with one track are used for this analysis, an overestimation by wrong association of true hits is not possible.

Increase n_{hit}: Noise hits in the module under investigation which are associated to a reconstructed track lead to an overestimated efficiency. This effect can be minimised by choosing an appropriate d_{assoc}. To find a reasonable association distance one can compute the probability P_{noise} that i noise hits exist in the event and are within d_{assoc}. According to Ref. [138, p. 86]:

$$P_{\mathrm{noise}} = \sum_{i=1}^{N_{\mathrm{pixel}}} B(i, n = N_{\mathrm{pixel}}, p = P_{\mathrm{occ}}) \cdot \left(1 - (1 - P_{\mathrm{assoc}})^i\right) . \tag{7.10}$$

Given 53 760 pixels on each module and a noise occupancy $P_{\mathrm{occ}} = 1 \times 10^{-6}$ (see above), the Binomial distribution B describes the probability for i noise hits anywhere on the module and is below 5.1 %. The association probability can be written as

$$P_{\mathrm{assoc}} = \left[1 - \left(1 - \frac{d}{D}\right)^2\right]^2 , \tag{7.11}$$

where D is the beam width, assuming a uniform beam profile [138, p. 86]. The overestimation in the efficiency is then computed as

$$\Delta\epsilon = (1-\epsilon)\cdot P_{\text{noise}}\ . \tag{7.12}$$

For the optimal d_{assoc}, two parameters are to be considered: The residual width and the beam width. To not underestimate ϵ, d_{assoc} is chosen close to 6σ. By keeping $d_{\text{assoc}} \leq 0.1D$ the systematic overestimation is smaller than 0.001 %. For this study the ROI was chosen as an ellipse with $d_{\text{assoc}} = 180\,\mu\text{m}$ and $500\,\mu\text{m}$ for the short and long pixel pitch respectively[3].

In summary, the systematic uncertainty in the hit-detection efficiency is lower than 0.01 % and is almost exclusively overestimating the efficiency.

7.3.2 Tracking resolution

For the matching procedure, tracks in the pixel detector are projected towards the ECC. Therefore, a sufficient projection accuracy is crucial for a successful track assignment, especially in a high-occupancy environment. Figure 7.7 shows the uncertainties $\sigma_{x,\text{proj}}$ and $\sigma_{y,\text{proj}}$ for the projection of reconstructed pixel detector tracks to given z coordinates. The uncertainty is computed according to Gaussian error propagation of Equation (7.3):

$$\sigma_{x,\text{proj}} = \frac{1}{N}\sum_{i}^{N}\sqrt{(z\sigma_{\theta_{xz}})^2 + \sigma_x^2 + 2z\sigma_{x,\theta_{xz}}}\ . \tag{7.13}$$

Here, N is the number of tracks and the single uncertainties are provided by the covariance matrix from the track fit. $\sigma_{y,\text{proj}}$ is computed accordingly. In the pixel detector rest frame the last ECC layer is located at $z \approx -1.8\,\text{cm}$. At this position, the uncertainties compute to $\sigma_{x,\text{proj}} = 17\,\mu\text{m}$ and $\sigma_{y,\text{proj}} = 20\,\mu\text{m}$. As expected for a multi-layer tracker the uncertainty is smallest in the centre of the detector. The distance between the last measurement point and the projection plane dominates the uncertainty.

7.4 Matching emulsion and pixel detector tracks

For track–track matching between reconstructed ECC and pixel detector tracks, a spatial and temporal alignment of the two detectors with respect to each other is necessary. The alignment has to be performed for each run individually since the ECC blocks are

---

[3] At a beam extent of approximately $7000\,\mu\text{m} \times 12\,000\,\mu\text{m}$

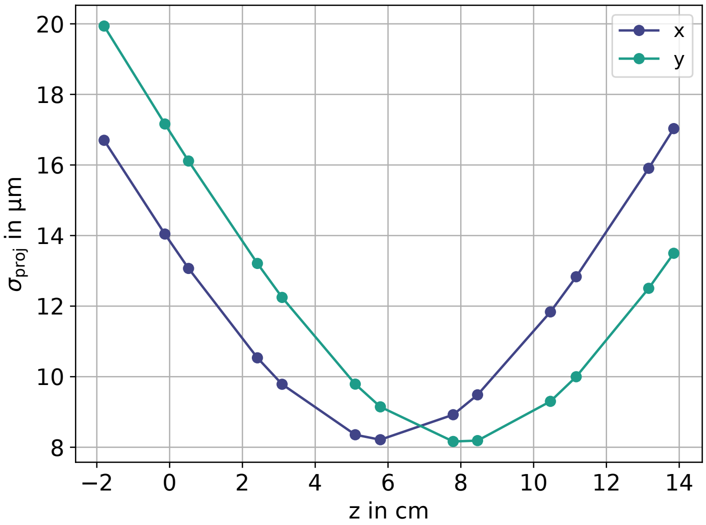

Figure 7.7: Projection uncertainty in track intersection coordinates for a given z for CHARM 1 run 6. The z coordinate is computed in the pixel detector reference frame.

exchanged manually, and the run conditions change. In the following, the alignment and matching quality are discussed and the matching rate for particles of different momentum is estimated. The results from this study are published in Ref. [166].

7.4.1 Alignment with the Newton-Raphson method

While there is no equivalent to the timestamp measurement of the pixel detector in the ECC, the start time, velocity and the direction of movement of the ECC can be used to transform pixel detector tracks in the ECC rest frame. This is possible, since the SoS signal triggers the ECC movement (with a fixed delay) as well as the timestamp reset of the pixel detector. The coordinate system used for the matching study is the rest frame of the emulsion detector. Assuming no misalignment, the coordinate transformation from the pixel reference frame $s(s')$ to the emulsion frame $s'(s)$ can be written as:

$$x' = -x - d_z\theta_{xz} + v_x t \tag{7.14a}$$

$$y' = s \cdot d_{\mathrm{s}} + y - d_z\theta_{yz} + v_y t \; . \tag{7.14b}$$

With d_z being the distance between the origin of the pixel tracker reference frame[4] and the last ECC layer, v_x and v_y the moving speed of the ECC during the spill in the respective

---

[4] For the pixel tracker reference frame the $x - y$ origin is chosen to be in the beam centre (cf. Figure A.4 in the Appendix), with $z = 0$ at the position of module 1, the one illuminated by the beam centre (cf. Figure 6.5).

direction, and t the time assigned to the pixel detector track. The spill number with respect to the run start is denoted by s and d_s is the vertical distance travelled by the emulsion detector in between spills. The pixel track direction in the $x-z$ and $y-z$ planes is given by θ_{xz} and θ_{yz} respectively.

To account for misalignment between the two detectors a set

$$\boldsymbol{\alpha} = \begin{pmatrix} x_0 & y_0 & d_z & \theta_{xz_0} & \theta_{yz_0} & \theta_{xy} & v_x & v_y \end{pmatrix} \tag{7.15}$$

of eight alignment parameters is introduced. The first two parameters, x_0 and y_0, account for spatial offsets. The rotational offsets θ_{xz_0}, θ_{yz_0} and θ_{xy} are with respect to the planes $x-z$, $y-z$ and $x-y$. The distance d_z between ECC and pixel tracker, as well as the velocities v_x and v_y are the same as introduced in Equation (7.14). This set of alignment parameters completes the coordinate transformation to the emulsion detector rest frame:

$$\boldsymbol{x}'_\mathrm{pix} = \begin{pmatrix} x' \\ y' \\ \theta'_{xz} \\ \theta'_{yz} \end{pmatrix} = \begin{pmatrix} x_0 + (x^\mathrm{pix} - d_z\theta'_{xz})\cos\theta_{xy} - (y^\mathrm{pix} - d_z\theta'_{yz})\sin\theta_{xy} + v_x t \\ y_0 + (y^\mathrm{pix} - d_z\theta'_{yz})\cos\theta_{xy} + (x^\mathrm{pix} - d_z\theta'_{xz})\sin\theta_{xy} + v_y t \\ (\theta^\mathrm{pix}_{xz} + \theta_{xz_0})\cos\theta_{xy} - (\theta^\mathrm{pix}_{yz} + \theta_{yz_0})\sin\theta_{xy} \\ (\theta^\mathrm{pix}_{yz} + \theta_{yz_0})\cos\theta_{xy} + (\theta^\mathrm{pix}_{xz} + \theta_{xz_0})\sin\theta_{xy} \end{pmatrix} . \tag{7.16}$$

To determine the parameters $\boldsymbol{\alpha}$, a dedicated alignment algorithm based on the work of Bocci and Hulsbergen [167] is employed [166].

A χ^2 of the residual between the emulsion and transformed pixel detector track is defined as:

$$\chi^2_\mathrm{track} = \boldsymbol{r}^\mathrm{T}\boldsymbol{V}^{-1}\boldsymbol{r} \ , \tag{7.17}$$

with

$$\boldsymbol{r} = \boldsymbol{x}'_\mathrm{pix} - \boldsymbol{x}_\mathrm{emu} = \begin{pmatrix} \Delta x & \Delta y & \Delta\theta_{xz} & \Delta\theta_{yz} \end{pmatrix} \tag{7.18}$$

as the vector of residuals of the single track parameters. $\boldsymbol{V} = \boldsymbol{V}_\mathrm{pix} + \boldsymbol{V}_\mathrm{emu}$ is the respective covariance matrix of the residuals, evaluated at the z-coordinate of the last ECC layer, defined as $z = 0$ in the emulsion detector rest frame. The χ^2_track is computed for all pairs of emulsion and pixel detector tracks and only pairs with $\chi^2_\mathrm{track} < 100$ are considered. Additionally, a hard cut of ±5 mm for Δx and Δy is applied, as well as a maximum of ±15 mrad for the two residuals $\Delta\theta_{xz}$ and $\Delta\theta_{yz}$. The remaining track pairs are ordered by their χ^2_track, and for every single track only the pair with the smallest χ^2_track is considered.

The total

$$\chi^2 = \sum_j \chi^2_{\mathrm{track},j} = \sum_j \left(\boldsymbol{r}^\mathrm{T}\boldsymbol{V}^{-1}\boldsymbol{r}\right)_j \ , \tag{7.19}$$

for j track pairs, is now to be minimised. The condition for a minimal χ^2 with respect to $\boldsymbol{\alpha}$ can be written as:

$$0 = \frac{d\chi^2}{d\boldsymbol{\alpha}} = 2\sum_j \left(\frac{\partial \boldsymbol{r}^{\mathrm{T}}}{\partial \boldsymbol{\alpha}} \boldsymbol{V}^{-1} \boldsymbol{r} \right)_j \quad . \tag{7.20}$$

The optimal set of parameters $\boldsymbol{\alpha}$, that satisfies this condition, is determined using the Newton-Raphson method [168, pp. 1023–1028]. For a given set of initial parameters $\boldsymbol{\alpha}_0$ the updated set $\boldsymbol{\alpha}_1$ is determined by computing the difference of the initial set and the derivative of Equation (7.20) with respect to the initial parameter set:

$$\boldsymbol{\alpha}_1 = \boldsymbol{\alpha}_0 - \left(\frac{\mathrm{d}^2\chi^2}{\mathrm{d}\boldsymbol{\alpha}^2} \right)^{-1} \Bigg|_{\alpha_0} \left(\frac{\mathrm{d}\chi^2}{\mathrm{d}\boldsymbol{\alpha}} \right) \Bigg|_{\alpha_0} \quad . \tag{7.21}$$

The calculation is iterated until a chosen convergence criterion is met, which in this case is a stable χ^2 with minimal or no observable change for increasing iterations. The resulting set $\boldsymbol{\alpha}$ is the optimal solution. The algorithm can be summarised to following steps:

1. Define a set of input alignment parameters $\boldsymbol{\alpha}_0$.
2. Transform the pixel detector tracks with the given set of parameters according to Equation (7.16).
3. Calculate the total χ^2 of track residuals for all pairs using Equation (7.19), apply the χ^2_{track} and Δx, Δy cuts described above.
4. Get a new set of parameters $\boldsymbol{\alpha}_i$ with Equation (7.21).
5. Repeat from step 2 using $\boldsymbol{\alpha}_i$ until χ^2 converges.

With the Newton-Raphson method, χ^2 does not necessarily converge. A successful alignment depends on an appropriate initial set of parameters. Without these, the algorithm could optimise the set of track pairs and alignment parameters to a weak mode, dominated by combinatorial background.

For the optimisation run, an alignment survey was performed on the SHiP−charm setup, measuring the physical positions of the sub-detectors with respect to a common reference point [160]. The offsets for pixel and emulsion detectors from this survey are used as input for the spatial positions of the initial parameter set. At the same time, the survey measurement constrains the possible spatial offsets. The initial rotational offsets are assumed to be zero. The target mover initial velocity is set to the programmed value of $v_x = 2.6\,\mathrm{cm/s}$ and $v_y = 0$. The optimised parameters for CHARM 1 run 6 are listed in Table A.1 in the Appendix, noteworthy results are discussed in the following.

The spatial offsets are within the survey measurement results, in particular the distance between ECC and pixel detector is measured to be $d_z = (1.835 \pm 0.007)\,\mathrm{cm}$, and the average target mover velocity is measured to be $v_x = \pm(2.610 \pm 0.005)\,\mathrm{cm/s}$. The shift in x_0 between alternating spills corresponds to a target moving with the given velocity for 5.2 s, matching the total moving time aimed for[5]. While the experiment was planned with no movement along the y axis, an average velocity $v_y = \pm(0.0295 \pm 0.0006)\,\mathrm{\mu m/s}$ with alternating direction is measured. From the change of direction of v_y for alternating spills a rotation of the ECC block by 11 mrad around the beam axis can be determined.

7.4.2 Track matching rate and resolution

Once converged, the Newton-Raphson method also provides the set of matched tracks in form of unique track pairs, sorted by the residuals χ^2. For a set of tracks to be matched, various selections are applied to the emulsion and pixel tracks before the alignment:

Emulsion tracks: The reconstruction of tracks and vertices in the emulsion detector is done independently of this work. In the following, the aspects important for the track matching are discussed. For a detailed description of the track reconstruction process in the emulsion detector the reader is referred to Refs. [115; 158].

> **Multiplicity:** On average, a 400 GeV/c proton interaction produces more than 10 charged particles and a similar number of photons. A large fraction of these particles carries enough energy for secondary hadronic re-interaction and development of electromagnetic showers, which can increase the number of reconstructed vertices by a factor of up to 100 [158, p. 10]. To reduce combinatorics and to select interesting hadronic interactions, only tracks associated to a vertex with at least six tracks are considered.
>
> **Transition:** Only tracks leaving the emulsion detector can be considered for matching. An emulsion track therefore has to have a base track[6] in the most downstream emulsion layer at $z = 0$.
>
> **Acceptance:** To ensure only tracks that are contained within the pixel detector are considered, an opening angle of $\theta_{\mathrm{emu}} \leq 210\,\mathrm{mrad}$ is required for the emulsion track.
>
> **Interaction:** The goal of SHiP−charm is to measure charmed interactions, therefore the focus lies on the reconstruction of events with inelastic proton scattering. To

---

[5] As discussed in Section 4.2.2, the target is accelerated before the actual spill start and also moves at the defined velocity before and after the spill

[6] For information on ECC track reconstruction the reader is kindly referred to Section 4.2.2

suppress non-interacting protons, a cut $n_{\text{passed}} \leq n_{\text{total}} - 1$ is placed on the number of emulsion layers passed by the track, n_{passed}.

Resolution: To minimise the influence of multiple Coulomb scattering on the matching resolution, the parameters of the base track in the most downstream emulsion layer are used for the alignment and matching described in Section 7.4.1.

Pixel tracks: As input for the matching, a new set of pixel detector tracks is reconstructed, employing fitting parameters optimised for the matching.

Transition: Only tracks leaving the pixel detector are reconstructed. A hit in the most downstream detector plane is therefore required for any pixel track. This requirement is satisfied by choosing the third and the last detector plane for track seeding, as described in Section 7.2.1.

Number of hits: Pixel track seeds with four or more independent hits (hits on different detector planes) are reconstructed as described in Section 7.2.2. While this increases the number of reconstructed pixel tracks with respect to the 6-hit requirement used for stand-alone pixel track reconstruction, no negative impact on the quality of matched tracks is expected. The ECC is the matching reference and pixel detector tracks without corresponding emulsion track are discarded in the alignment process.

Acceptance: While the transition criterion is in principle sufficient to also ensure reconstruction within the acceptance, a limit on the pixel track seed opening angle $\theta_{\text{pix}} \leq 210\,\text{mrad}$ is set to reduce computing time and combinatorics.

Figure 7.8 shows the residuals as defined in Equation (7.18) in all four track parameters for matched tracks in CHARM 1 run 6, using the alignment parameters $\boldsymbol{\alpha}$, given in Table A.1. All four distributions are well centred and symmetrical. Furthermore, the distributions show similar behaviour, as they can be described by the sum of two Gaussian distributions with $\sigma_1 \approx 2 \cdot \sigma_2$. The fit on the y-residuals in Figure 7.8 however, results in two equally high distributions only distinguished by the width. The y-residual distribution is particular sensitive to a cut on the positive track angle $\theta_{xz} < 75\,\text{mrad}$. This suggests that a significant contribution to the measurement uncertainty is added by angular misalignment of one of the detectors and that multiple scattering is not dominating the residual width, as would be expected according to Section 7.3.1. The uncertainty in track parameters for matched tracks is measured as the full width at half maximum (FWHM) of the respective distribution, and given in Table 7.2. Despite room for optimisation of the alignment, the results allow for satisfactory track matching and further studies.

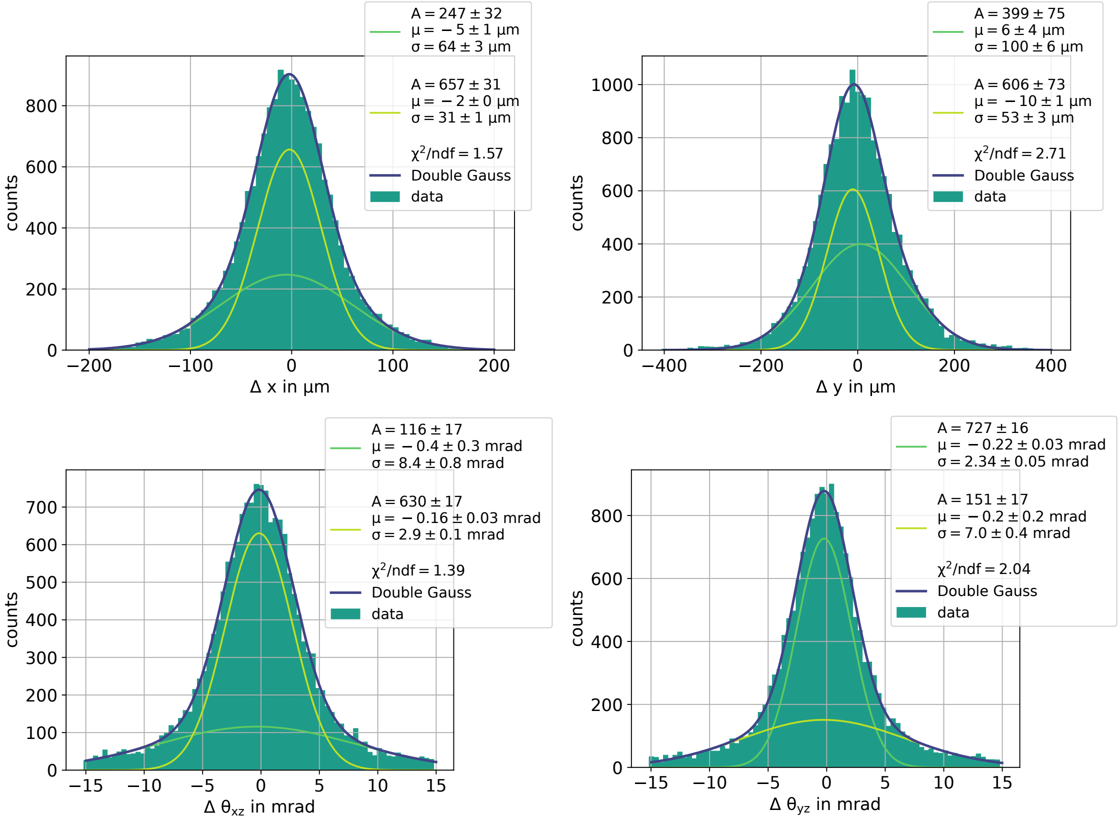

Figure 7.8: Positional and rotational residuals of matched emulsion and pixel detector tracks for optimised $\boldsymbol{\alpha}$ in CHARM 1 run 6. The distributions are well described by a sum of two Gaussians. Results for y show equally strong contribution from the two functions and are sensitive to the track angle θ_{xz}.

Parameter	**Value**
σ_x	41 µm
σ_y	71 µm
$\sigma_{\theta_{xz}}$	3.8 mrad
$\sigma_{\theta_{yz}}$	3.1 mrad

Table 7.2: Uncertainties in track parameters for matched tracks from fits to the residual distributions. The projection accuracy is dominated by the uncertainty in the track angles. Fit results and distributions can be obtained from Figure 7.8.

Figure 7.9 (left) shows the track intersections of matched tracks on the last emulsion layer of CHARM 1 run 6 in the emulsion rest frame. The single spills can be identified; within spills the track intersection points are uniformly distributed. The right plot shows the corresponding χ^2_{red} distribution. It peaks around 1 and is falling continuously.

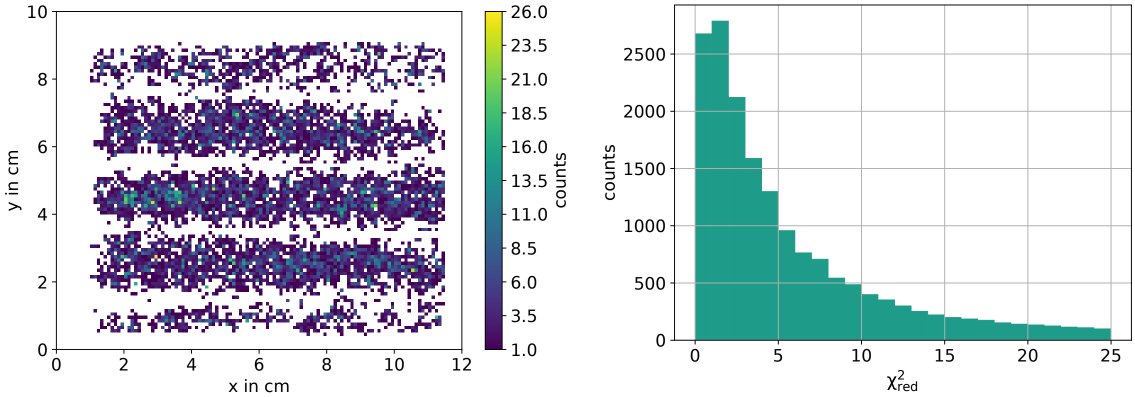

Figure 7.9: Position of matched tracks in the emulsion rest frame for CHARM 1 run 6 (left). The single spills can be clearly identified. χ^2_{red} distribution for matched tracks in the same run (right). The distribution peaks around 1.

For analysis and presentation, an event display has been developed in the scope of this work, presented in Figure 7.10. One matched event is displayed, where the combined emulsion and pixel detector data is visible. A 3 D view is provided on the left, and 2 D views are provided on the right. For a matched emulsion track, all selected tracks associated to the same vertex are plotted. For a matched track of a pixel detector event, all selected tracks within the event are plotted. Observing the event display, the power of matching single tracks is evident: Once a single track of an emulsion vertex is matched, all tracks of this vertex are assigned a timestamp, and are thus available for event building and further analysis.

To quantify the matching performance, a matching rate is computed, similar to the hit-detection efficiency in Section 7.3.1. To ensure a clean sample, characteristic events are selected, considering two features:

1. For the experiment, only tracks reaching the spectrometer are of interest: During data analysis the occupancy in the drift tube detector was found to be too high for meaningful reconstruction. Therefore, only tracks within the SciFi detectors acceptance are considered, which translates to a maximum allowed track opening angle $\theta = 62\,\mathrm{mrad}$.

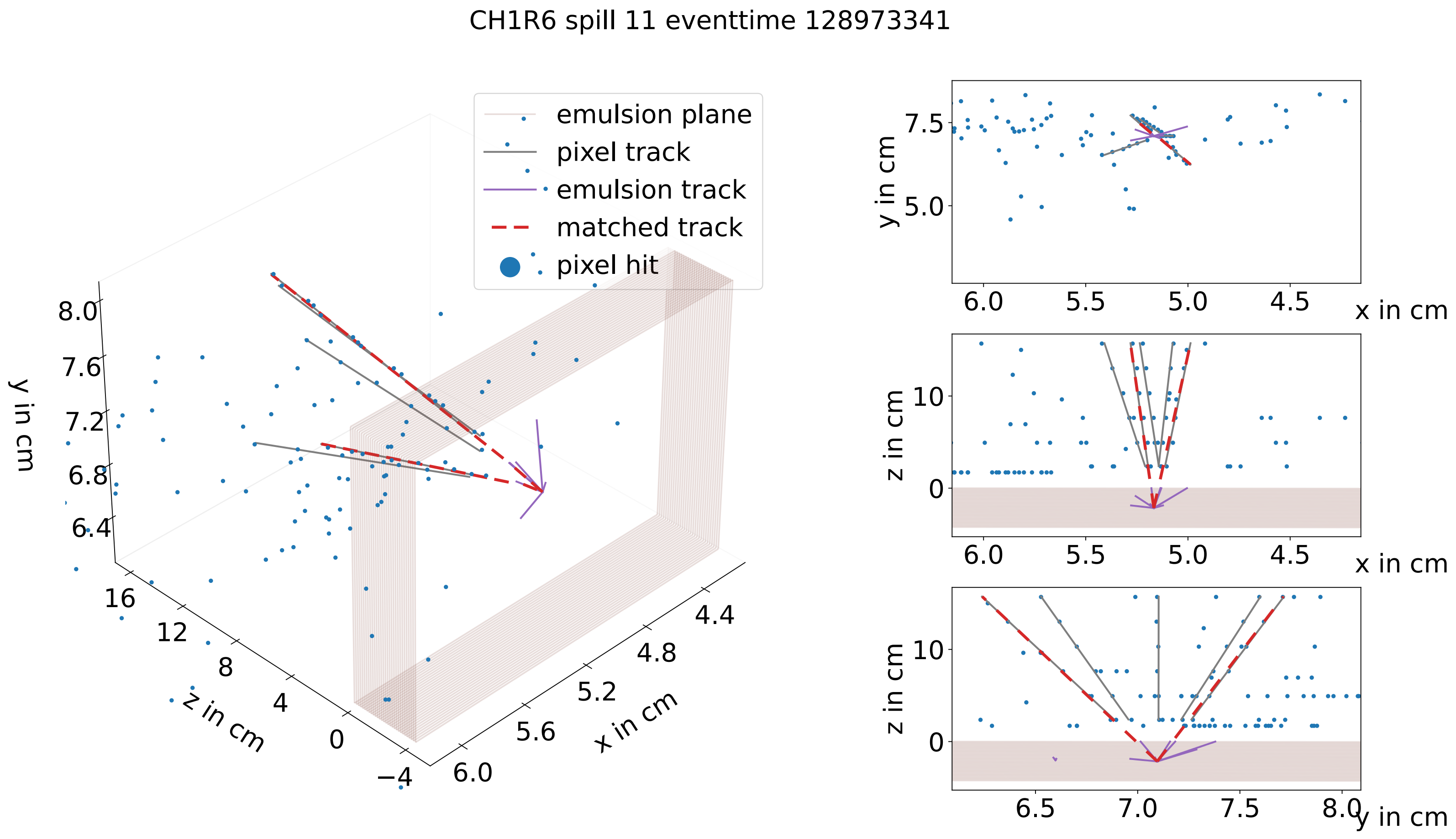

Figure 7.10: Display of a matched event in the emulsion and pixel detectors. The red dashed lines mark matched tracks, blue points mark hits in the pixel detector. The single emulsion layers are rendered transparent.

2. The spill assignment of emulsion tracks is solely based on the y intersection coordinate of tracks. For tracks with larger angles, or in case of a run with 10 spills on a single brick, this assignment is not necessarily correct. To measure the matching rate, an unambiguous spill assignment is necessary. Therefore, only emulsion tracks with a $y - y_s \leq \pm 0.4\,\mathrm{cm}$ are considered. Here, y_s is the mean y for a given spill.

The rate ϵ_m is defined as the ratio of selected ECC tracks assigned to tracks in the pixel detector n_pix over the number of selected ECC tracks n_ECC:

$$\epsilon_\mathrm{m} = \frac{n_\mathrm{pix}}{n_\mathrm{ECC}} \,. \tag{7.22}$$

In Figure 7.11 (left) the matching rate is displayed as a function of the track intersection on the last emulsion layer. The single spills can be identified, and no systematic inefficiencies can be observed. The average matching rate is $(82.6 \pm 0.4)\,\%$, with the statistical uncertainty given, determined according to Ref. [138, p. 79 ff]. For the systematic contributions a dedicated analysis is done in the following section.

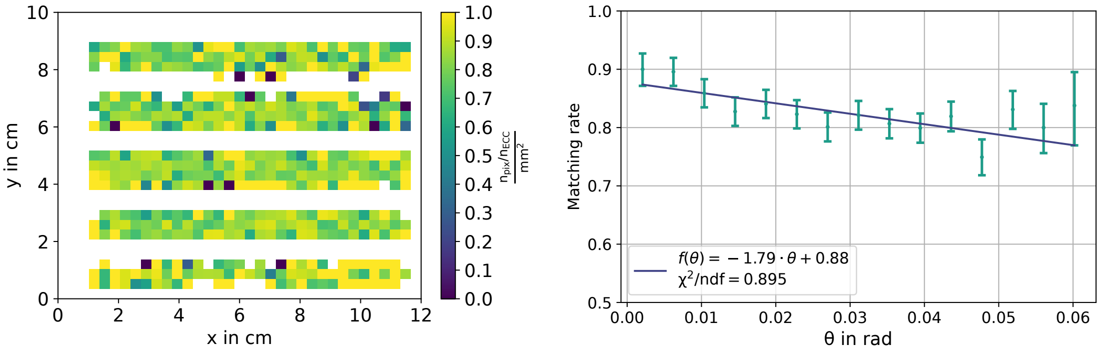

Figure 7.11: Matching rate as a function of the track position in the ECC coordinate system (left) and as function of the emulsion track opening angle θ (right) for CHARM 1 run 6. The error bars represent $\sigma_\mathrm{stat} \oplus \sigma_\mathrm{syst}$. This result is also published in [166].

The average matching rate is defined with respect to the number of selected emulsion detector tracks. The matching rate of vertices reconstructed in the emulsion detector is in fact higher: Timestamps can be assigned to $(87 \pm 2)\,\%$ of vertices associated to selected tracks and in case a vertex is timestamped the matching rate for selected tracks associated to this vertex is on average $(86 \pm 1)\,\%$, while for $(65 \pm 3)\,\%$ of vertices all selected tracks can be matched. Table 7.3 summarises the results.

rate	**value**
track matching (ϵ_{m})	$(82.6 \pm 0.4)\,\%$
vertex matching	$(87 \pm 2)\,\%$
in-vertex matching	$(86 \pm 1)\,\%$
fraction of completely matched vertices	$(65 \pm 3)\,\%$

Table 7.3: Matching rates of tracks and vertices.

Systematic effects in the matching rate

Figure 7.11 (right) shows the matching rate as function of the track opening angle. As is evident, the rate decreases for increasing track opening angle. To quantify the dependence, a linear function is fitted to the data points considering the uncertainty

$$\sigma_{\epsilon(\theta)} = \sqrt{\sigma_{\mathrm{stat}}^2 + \sigma_{\mathrm{sys}}^2}\,, \tag{7.23}$$

computed for every data point. Here the statistical contribution is computed as described above, considering the small amount of data the single measurement points offer. For the systematic contribution, the track matching rate is measured for a series of χ^2_{red} cuts, as is displayed in Figure 7.12. The systematic error is quantified as the average deviation of $\epsilon_\theta(\chi^2)$:

$$\sigma_{\mathrm{sys}} = \frac{1}{N} \sum_{i=10}^{N=100} \bar{\epsilon}_\theta\left(\chi^2_{\mathrm{red}} \leq \frac{i}{2}\right) - \bar{\epsilon}_\theta\left(\chi^2_{\mathrm{red}} \leq 25\right)\,. \tag{7.24}$$

Where $\bar{\epsilon}_\theta(\chi^2_{\mathrm{red}})$ is the average over the single $\epsilon(\theta)$ measurements for given χ^2_{red}.
Two contributions to this systematic dependence are identified: The angular alignment leaves room for improvement, as discussed above. Additionally, the observed dependence suggests a correlation between particle momentum and track opening angle, discussed in Section 7.4.3.

7.4.3 Predicted matching rate as function of particle momentum

The measured yields for SHiP−charm are directly proportional to the matching rate, which has been shown to have an angular dependence. At the same time, the charmed hadrons produced in SHiP−charm are expected to have low momenta compared to the primary protons. In Figure 7.13 the momentum distribution of charmed hadrons in primary and

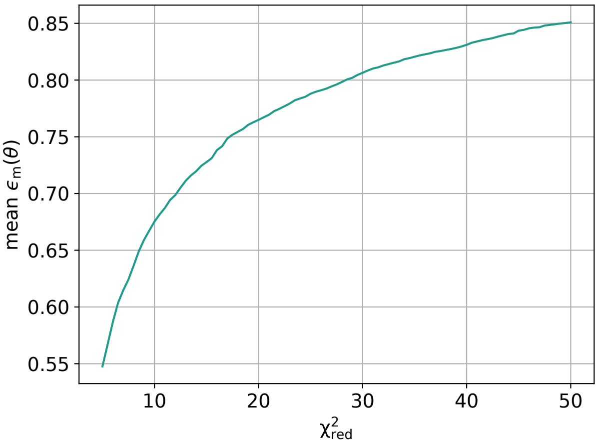

Figure 7.12: Matching rate as a function of allowed χ^2_{red} for CHARM 1 run 6. Given the observed behaviour, the cut of $\chi^2_{\mathrm{red}} \leq 25$ should not overestimate the matching rate.

cascade production is shown, as predicted by simulation [100]. The distribution shows the majority of primary as well as secondary charmed hadrons below 50 GeV/c. The pixel and emulsion detector data alone does not allow for momentum measurements, since both detectors are located outside of the magnetic field (see Chapter 4).

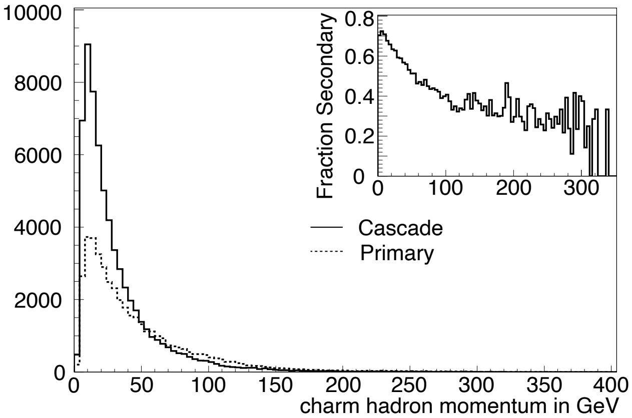

Figure 7.13: Momentum of charmed hadrons from primary and cascade production as expected from simulation [100, p. 8].

The matching rate as function of the particle momentum can be estimated. To investigate the correlation between track opening angle and matching rate, data from an existing Monte-Carlo simulation is used [115]. A total of 135000 events in the CHARM 1 run 6 target configuration is available, including tracks and vertices reconstructed in the emulsion detector. This dataset offers 8×10^6 particle tracks associated to a vertex. A selection on the emulsion tracks in three aspects is performed.

Acceptance: To leave the magnetic field in downstream direction after deflection, tracks from the emulsion detector need sufficient momentum. Therefore, a requirement of $p \geq 10\,\mathrm{GeV}/c$ is set.

Interaction: Only particles from interaction in the target are considered. Thus, in the simulation dataset only particles with an identified mother particle are selected.

Transition: Only tracks leaving the emulsion detector are considered. Again this is ensured by selecting only tracks with an entry in the most downstream ECC layer.

After selection, approximately 7×10^4 emulsion tracks are available for the study. Figure 7.14 (top and centre) shows the track opening angle θ for various momenta in the selected dataset. A decrease of the mean track angle with increasing momentum can be observed. Using the relation $\epsilon_\mathrm{m}(\theta)$ obtained from the fit (see Figure 7.11) and the relation between track opening angle and momentum from simulation, the matching rate as a function of momentum is calculated (Figure 7.14, bottom). The rate saturates at 87 % around a particle momentum of $50\,\mathrm{GeV}/c$. This matching rate is a conservative estimation, since also tracks outside the acceptance of the SciFi detector are considered. While the estimated matching rate of 81 to 86 % for the lower momentum regime is deemed to be sufficient for the charmed hadro-production measurement, the accuracy would be improved by a higher matching rate. Event reconstruction employing SciFi detector data is the most promising step towards a rate improvement.

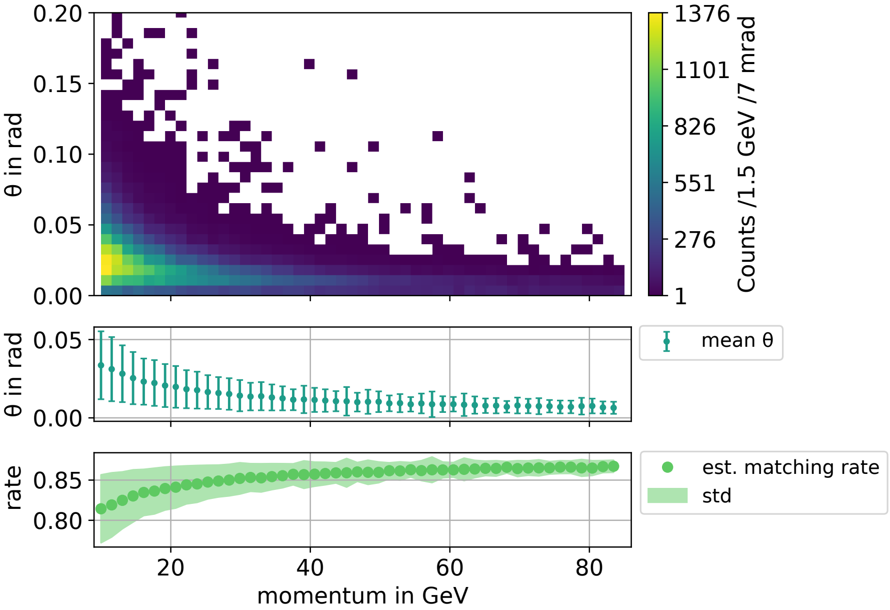

Figure 7.14: Track angle (top), average track angle (centre) and matching rate (bottom) as a function of particle momentum of simulated tracks in the emulsion detector. This result is also published in Ref. [166].

7.5 Track projection to the SciFi detector

In preparation of an analysis which employs all sub-detectors, the tracks reconstructed in the pixel detector can be projected through the magnetic field of GOLIATH and towards the SciFi detector. A detailed measurement of the magnetic field was performed prior to the SHiP−charm measurement campaign, with an equally spaced three-dimensional grid mapping the field with 50 mm resolution in every dimension and for different field strengths [169]. Figure 7.15 shows the magnetic field strength and the corresponding deflection angle for 400 GeV/c protons.

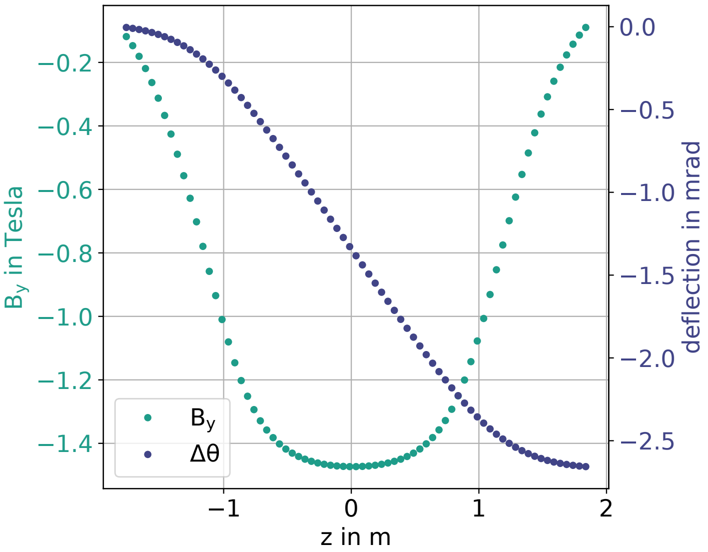

Figure 7.15: y-component of the GOLIATH field along the beam axis for the maximum possible field strength and resulting deflection angle for 400 GeV/c protons. The right-handed coordinate system originates in the magnet centre on the beam axis.

In SHiP−charm, all runs with magnetic field “on” were performed with the maximum possible field strength of approximately −1.5 T. A projection of particle tracks through the magnetic field depends on the momentum and the charge of the particle (see Section 4.2.3), and the projection in this study is done based on pixel detector data alone. Therefore, for calibration purposes, primary proton events are used for their known momentum and charge. The tracks reconstructed in the pixel detector are propagated through the magnetic field in 73 steps according to Equation (4.3). Figure 7.16 shows the propagation exemplarily for three tracks and the resulting distribution for an example run. As can be obtained from the trajectories, the extrapolated position strongly depends on the track angle at the point of entry in the field. The long projection distance of 4.55 m implies an uncertainty of 1.7 mm on average.

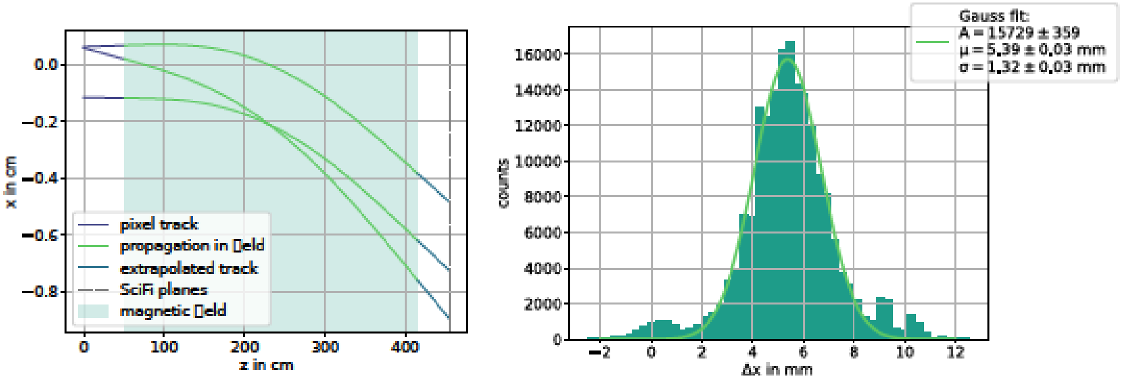

Figure 7.16: Track propagation through the GOLIATH magnetic field for three 400 GeV/c proton tracks (left). Deflection in x of proton tracks at the first SciFi detector plane for an example run. The right-handed coordinate systems origin is the beam centre on the first pixel detector plane.

The SciFi detector was not fully operational during the optimisation run. In particular, data readout was severely impaired and lead to incomplete and incorrectly reconstructed SciFi-detector events. The performed projection study, however, shows, that with an operational readout and within reasonable occupancy, the reconstruction of events employing the pixel and SciFi detectors seems promising.

8 Vertex reconstruction in a thick target

The tracks reconstructed in the pixel detector stem from interaction vertices located upstream in the ECC, as illustrated in Figure 8.1. While vertex positions and track-to-vertex association for the SHiP−charm measurement is provided by the emulsion detector, the quality of pixel detector tracks is sufficient to conduct standalone vertex-reconstruction studies.

In this chapter, the reconstruction process is introduced. First, vertex seeds or 2-track vertices are identified, which are then fed to a vertex-finding algorithm. Once the most likely combination of tracks for a vertex is identified, the vertex position is fitted. Results of the vertex reconstruction procedure on a Monte-Carlo simulation sample are presented and features of reconstructed vertices in SHiP−charm data are discussed. Finally, the vertices in pixel detector data are matched with the vertices in ECC data.

8.1 General approach – finding vertex seeds

Given an event with more than one track, the tracks reconstructed in the pixel detector stem from an unknown number of interaction vertices in the target. Figure 8.1 shows an illustration of different possible topologies. The origin of tracks could be a single primary vertex, several secondary vertices, or a mixture of both, and without additional information, the vertex reconstruction can only rely on the track parameters measured.

The vertex reconstruction is performed on track sets reconstructed with the algorithm introduced in Section 7.2 along with a requirement of six hits per track. The first step is the reconstruction of 2-track vertices, or *vertex seeds*: points in space where two tracks intersect. Since skewed lines do not necessarily intersect, and an actual intersection is unlikely due to measurement uncertainty, the vertex seed is defined as the point of closest approach (POCA), the point in space where the two lines come closest to each other, with respect to their uncertainty. To find all seeds in one event, the POCA $\boldsymbol{q}$ of two tracks is computed for all combinations of tracks reconstructed in the event. Figure 8.2 shows an illustration of two tracks with the corresponding POCA. Assuming the two tracks are

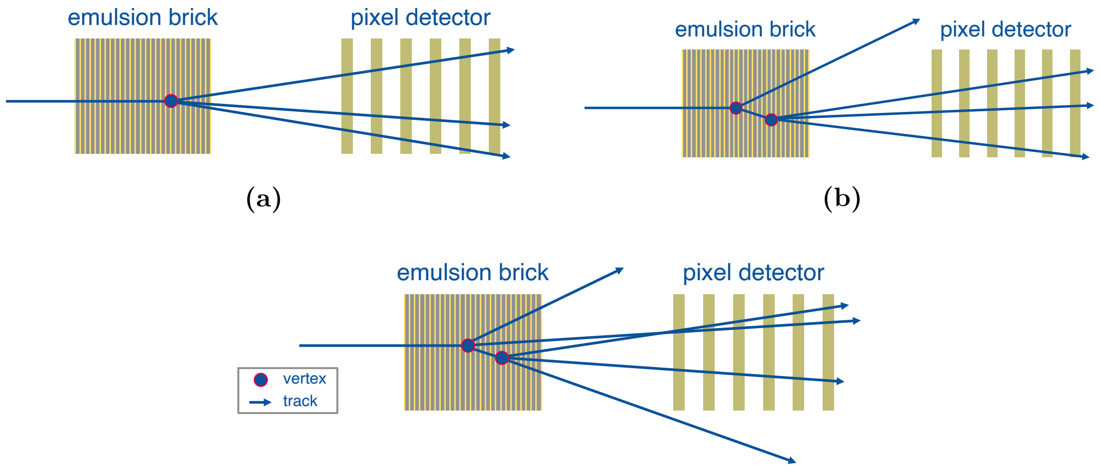

(a) (b) (c)

Figure 8.1: Selection of different vertex topologies in SHiP−charm. Three categories can be distinguished: The event contains only a primary vertex located in the ECC (a). The emerging tracks enter the pixel detector. The event contains primary and secondary vertices (b), particles from the secondary vertex enter the pixel detector. The event contains primary and secondary vertex (c), but tracks from both vertices enter the pixel detector. While this is a selection for illustration purposes, at the occupancy in SHiP−charm, much more complex topologies are likely.

parameterised as

$$\boldsymbol{f}(t) = \boldsymbol{x} + t \cdot \boldsymbol{u} \quad \text{and} \quad \boldsymbol{g}(s) = \boldsymbol{y} + s \cdot \boldsymbol{v} \ , \tag{8.1}$$

and not parallel, then a vector

$$\boldsymbol{r} = (\boldsymbol{f}(t) - \boldsymbol{g}(s)) \tag{8.2}$$

can be defined. The minimal $d(s,t) = \|\boldsymbol{r}\|$ is found in a line perpendicular to $\boldsymbol{f}$ and $\boldsymbol{g}$, satisfying $\nabla_s d(s,t) = \nabla_t d(s,t) = 0$:

$$\Rightarrow 0 = 2\, \boldsymbol{r}(s,t) \cdot (-\boldsymbol{v}) \ , \tag{8.3a}$$

$$\Rightarrow 0 = 2\, \boldsymbol{r}(s,t) \cdot \boldsymbol{u} \ . \tag{8.3b}$$

Equations 8.3 are solved for $s_\mathrm{m}, t_\mathrm{m}$, and the resulting $\boldsymbol{r}(s_\mathrm{m}, t_\mathrm{m})$ gives the shortest $\boldsymbol{r}$ between the two tracks. The POCA $\boldsymbol{q}$ is defined as the centre between the two points $\boldsymbol{x}_\mathrm{m}$ and $\boldsymbol{y}_\mathrm{m}$ on the lines $\boldsymbol{f}$ and $\boldsymbol{g}$, connected by $\boldsymbol{r}(s_\mathrm{m}, t_\mathrm{m})$:

$$\boldsymbol{q} = \frac{\boldsymbol{x}_\mathrm{m} + \boldsymbol{y}_\mathrm{m}}{2} = \begin{pmatrix} x_\mathrm{q} \\ y_\mathrm{q} \\ z_\mathrm{q} \end{pmatrix} \ . \tag{8.4}$$

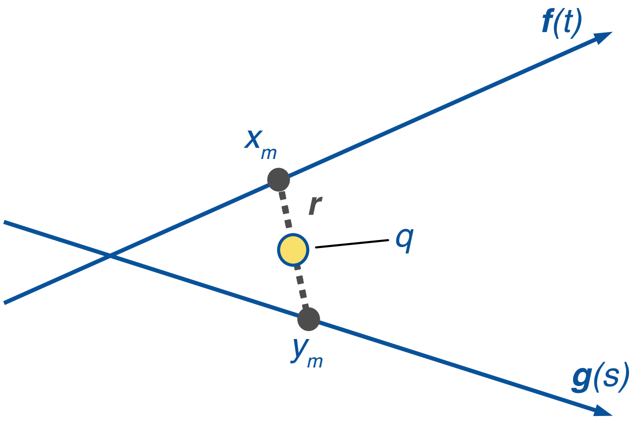

Figure 8.2: Reconstruction of POCA for two tracks in three dimensions. The vector $\boldsymbol{r}$ is minimal if it is perpendicular to both tracks. The POCA $\boldsymbol{q}$ is then in the centre of $\boldsymbol{r}$.

The vertex seed position is fitted with $\boldsymbol{q}$ as input, and the resulting $\boldsymbol{v} = (x_\mathrm{v}, y_\mathrm{v}, z_\mathrm{v})$ kept if the evaluated $p \geq 0.05$, where p denotes the probability to observe a vertex position with the given χ^2. The probability is computed as the incomplete gamma function for given χ^2 and ndf:

$$p = 1 - P\left(\frac{\chi^2}{2}, \frac{\mathrm{ndf}}{2}\right) = 1 - \frac{2}{\mathrm{ndf}} \int_{\chi^2/2}^{\infty} e^{-t} \cdot t^{\,\mathrm{ndf}/2-1}\, dt\,. \tag{8.5}$$

Here, ndf $= 1$ since each of the two tracks provides an x and y coordinate for given z. The vertex fitting method is described in detail in Section 8.3. Figure 8.3 shows the reconstructed z_v and the target position for vertex seeds in CHARM 1 run 6. Neither in the fit, nor for selection, a cut on the vertex seed position is applied.

The ECC extent is well-matched, although combinatoric background can not be completely removed by the quality requirement. The distribution of x and y positions of the vertex seeds is matching the beam spot (see Figure 7.1), as expected. A successful reconstruction of target and beam position without fit restrictions proves the quality of vertex seeds suited for further reconstruction.

8.2 Vertex finding

The set of vertex seeds is generated from all possible combinations of tracks, and therefore does not reflect the true association of tracks to vertices. To reconstruct true vertices, the vertex seeds need to be combined to sets of the most-likely combinations of tracks. To do so, an undirected graph is built from all reconstructed vertex seeds in an event and evaluated with a Bron–Kerbosch algorithm [170], as implemented in the boost C++ library [171].

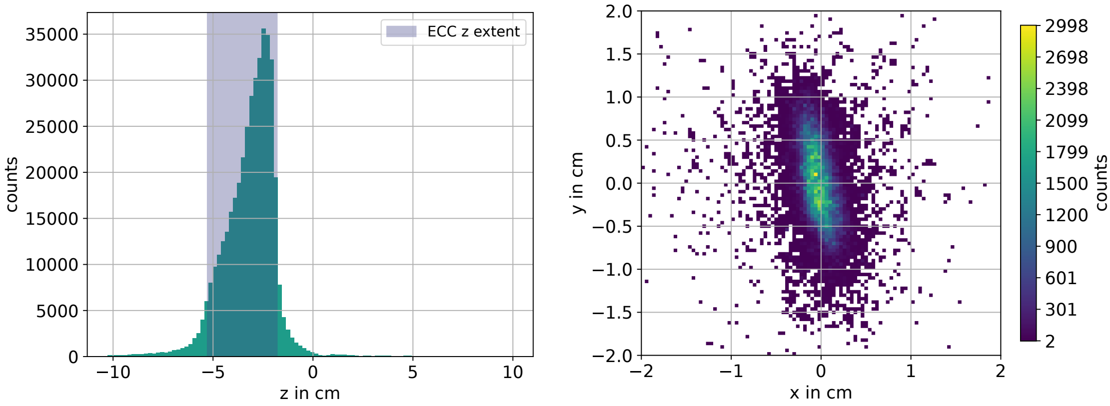

Figure 8.3: z_v (left) and $x-y$ map of vertex seed positions (right) in CHARM 1 run 6. The target position (ECC z extent), which was determined with track matching (see Section 7.4), and the beam spot (compare Figure 7.1) are well-matched.

In a graph, nodes are connected by edges, in an undirected graph the edges do not carry additional information. In this work, each track in a vertex seed is represented by a node, and two tracks are connected by an edge, if they form a seed. The quality of the vertices that have been found is improved by applying selection cuts to the vertex seeds before building the graph:

- $(z_\mathrm{min} - 1\,\mathrm{mm}) \leq z_\mathrm{v} \leq (z_\mathrm{max} + 1\,\mathrm{mm})$. With $z_\mathrm{min}, z_\mathrm{max}$ the start and end position of the target along the beam axis.
- $|x_\mathrm{v}|, |y_\mathrm{v}| \leq 4\,\mathrm{cm}$. This limit approximates the active detector surface with respect to the target and is only chosen to reduce the computing time. The $3\,\sigma$ extent of the beam is smaller, approximately 1.2 cm in y and 0.36 cm in x (see Figure A.4 in the Appendix).

The Bron–Kerbosch algorithm finds all maximal complete subgraphs in this graph, also called *maximal cliques*. A clique is a set of nodes, where all nodes are adjacent, i.e. connected by edges. A maximal clique is then defined as a clique which can not be extended any more, and as such is not contained in any larger clique. The Bron–Kerbosch algorithm uses a recursive backtracking approach on the set of all nodes V in a graph G. Nodes are assigned to either one of three sets R, P and X. R is the clique under investigation, P is the set of candidates to join R, and X is an exclusion set, containing already processed vertices. An important feature of nodes is the *neighbourhood* $N(v)$: $N(v)$ is the set of all nodes which are connected by an edge to v. A representation of the algorithm in pseudocode is available in Listing 2 in the Appendix, it can be summarised to the following steps:

1. Start with $R = \{\}, P = V, X = \{\}$. Pick one node $v \in V$ as seed for a clique: $R = \{v\}$.
2. Prepare sets for recursion: $P_r = P \cap N(v)$, $X_r = X \cap N(v)$
3. **Start recursion**: For every node $v_r \in P_r$ add v_r to the set R.
4. If X_r and P_r are empty, a maximal clique R is found, return R.
5. Remove v from P_r and add v to X.
6. Repeat steps 1-5 for all $v \in P$.

Figure 8.4 visualises the graph for an event with seven tracks and eight vertex seeds on the left. On the right side, the graph is divided in all maximal cliques, where each clique represents a possible vertex. Whether the track set forms a true vertex has to be verified by a fit.

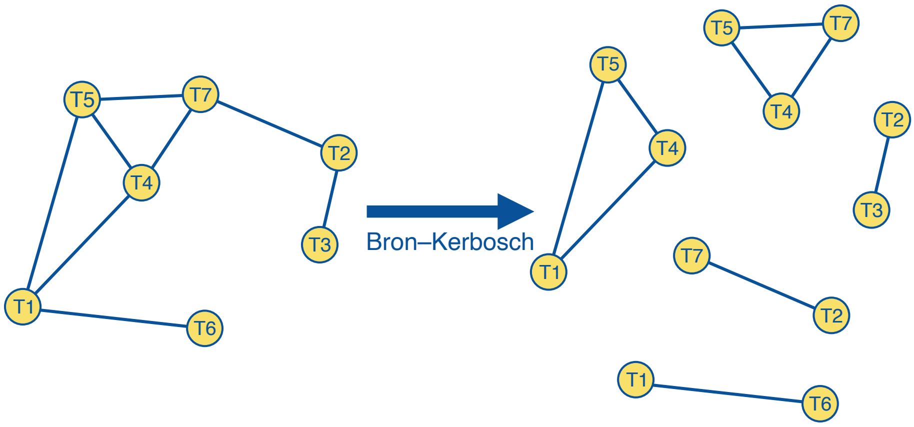

Figure 8.4: Graph with 7 nodes and 8 edges. The nodes T1 to T7 represent all tracks in the event, associated to a vertex seed. The edges represent the seed association. The Bron–Kerbosch algorithm creates the maximal cliques on the right. The tracks within a clique likely form a vertex. Ambiguities are disentangled during the fitting procedure, based on the vertex p-value.

8.3 Vertex fitting

The vertex position is defined as the point in space where the associated tracks originate from, as illustrated in Figure 8.1. The reconstruction of this point can not be done by calculation of the intersection of all associated tracks, since tracks are reconstructed with an uncertainty and do not necessarily, in fact never, intersect in one space point. Therefore, the track set determined by the vertex finding algorithm is used as input for a vertex position.

Under the assumption that the associated tracks in fact originate from the vertex position, the track parameters can be optimised in the fit as well. The vertex fit is thus a simultaneous fit of vertex position and track parameters of associated tracks. The fit is realised as a χ^2 minimisation with

$$\chi^2 = \sum_i \boldsymbol{r}_i^T \boldsymbol{V}_i^{-1} \boldsymbol{r}_i \ , \ \text{with} \ \ \boldsymbol{r}_i = \boldsymbol{x}'_i - \boldsymbol{x}_i = \begin{pmatrix} x'_i - x_i \\ y'_i - y_i \\ \theta'_{xz,i} - \theta_{xz,i} \\ \theta'_{yz,i} - \theta_{yz,i} \end{pmatrix} \ . \tag{8.6}$$

Here, $\boldsymbol{x}'_i$ is the vector of new trajectory parameters for the i-th track associated to the vertex. The vertex position is directly depending on the new trajectory directions:

$$\theta'_{xz,i} = \frac{v_x - x_i}{v_z}, \quad \text{and} \quad \theta'_{yz,i} = \frac{v_y - y_i}{v_z} \ . \tag{8.7}$$

The χ^2 is minimised with the same Minuit 2 algoritm as the track fit in Section 7.2.2. After convergence, a set of track parameters

$$\boldsymbol{\alpha}_\mathrm{t} = \begin{pmatrix} x_1 & y_1 & \theta_{xz,1} & \theta_{yz,1} & \cdots & x_n & y_n & \theta_{xz,n} & \theta_{yz,n} \end{pmatrix} \tag{8.8}$$

and the vertex position

$$\boldsymbol{\alpha}_\mathrm{v} = \begin{pmatrix} v_x & v_y & v_z \end{pmatrix} \ \text{with} \ \ \mathrm{ndf} = 3 - 2 \cdot n \tag{8.9}$$

are available, where n is the number of tracks associated to the vertex.

This fit is performed on all cliques found in an event and the set of fitted vertices is further optimised:

- The fitted vertex has to pass a $p \geq 0.05$ cut.
- In case the vertex quality is lower, a refining process starts. In each process iteration, the track with the strongest influence on p is removed from the vertex and the fit is performed again with the reduced track set until the cut is passed. If only 2 tracks are left in the vertex and p is not meeting the requirement, the vertex is discarded.
- The vertex z position is verified with the same requirements imposed on the vertex seeds, depending on the target position and size. Only a maximal and minimal z are provided for the cut.

- Since all maximal cliques are fitted, and the initial set of vertex seeds forming the cliques is ambiguous, tracks can be associated to more than one vertex. To resolve this ambiguity, all vertices with common tracks are further processed:
  - If a vertex is fully contained in another one, the vertex with lower multiplicity is dropped.
  - Vertices with common tracks are merged, given the new vertex passes the p-value requirement.
  - In case the merged vertex is not of sufficient quality, the one with higher p is kept, and common tracks are removed from the remaining vertices. The residual vertices are then fitted again with the same p requirement.

8.3.1 Verification with Monte-Carlo simulation vertex sample

The performance of the algorithm is verified with a simulated sample of 10 000 events. For every event, between 1 and 3 vertices are created with 2 to 6 associated tracks each. The sample contains $\mathcal{O}(2 \times 10^4)$ vertices and $\mathcal{O}(8 \times 10^4)$ tracks. The distributions of vertex and track positions are modelled to emulate the distributions found after track reconstruction for CHARM 1 run 6, as can be seen in Figure 8.5. The coordinate system is the same as for track reconstruction, with the origin in the beam centre on the first detector plane and z following the beam. The track intersection points and angles are consequently defined with respect to a detector plane at $z = 0$. The track angles are limited to $\theta_{xz}, \theta_{yz} < 150\,\mathrm{mrad}$. Under the assumption of no detector misalignment and without considering multiple scattering, the uncertainties in the track intersection coordinates $\sigma_{x,\mathrm{truth}} = 17\,\mu\mathrm{m}$ and $\sigma_{y,\mathrm{truth}} = 20\,\mu\mathrm{m}$ are chosen as the projection resolutions of the pixel detector measured with primary protons as presented in Section 7.3.2. The uncertainty in track opening angles $\sigma_{\theta_{xz,\mathrm{truth}}}$ and $\sigma_{\theta_{yz,\mathrm{truth}}}$ depends on the uncertainty σ_z in the distance between the vertex and the assumed detector plane $\Delta z = z_0 - z_{\mathrm{v,truth}}$: An uncertainty $\sigma_z = 50\,\mu\mathrm{m}$ is assumed for the computation of track opening angle uncertainties. The vertex-seed finding is applied to the true tracks and their respective uncertainties with the same $p \geq 0.05$ requirement as for data, and the finding and fitting algorithms for the final vertices are applied to the resulting vertex seeds with the following parameters:

- $-100\,\mathrm{cm} < z_{\mathrm{v,reco}} < 0\,\mathrm{cm}$,
- $|x_{\mathrm{v,reco}}|, |y_{\mathrm{v,reco}}| \leq 100\,\mathrm{cm}$,
- $p \geq 0.05$.

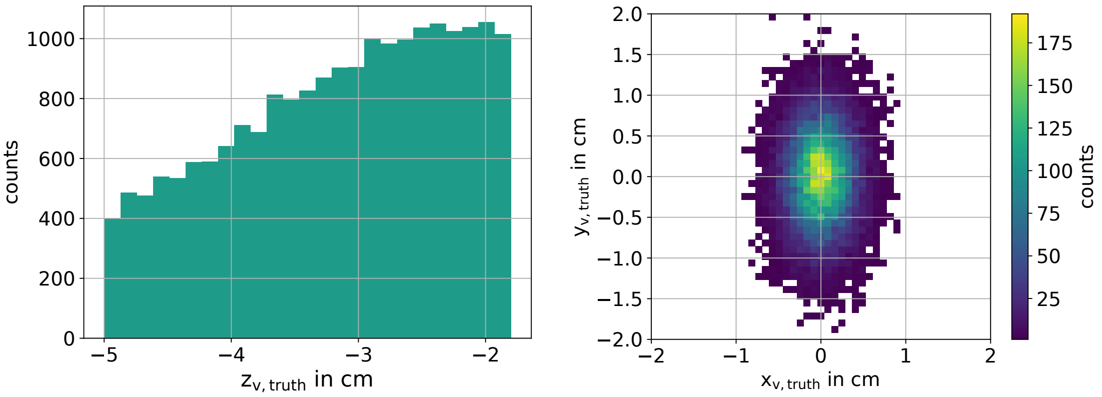

Figure 8.5: z_v and $x_\mathrm{v} - y_\mathrm{v}$ distributions for simulated vertices. The coordinate system chosen is the same as for track reconstruction with the origin at the beam centre on the first detector layer.

The resulting χ^2/ndf and p-value distributions for reconstructed vertices are shown in Figure 8.6. The histograms discriminate between 2-track vertices and vertices with higher multiplicity, as for the results on data in Section 8.3.2. For the 2-track vertices with ndf $= 1$, a χ^2 distribution peaking close to 0 is expected. For Gaussian distributed uncertainties of adequate size a flat p-value distribution is expected. Here the average p-value for reconstructed vertices is 0.52 and the distribution is considered reasonably flat. The true vertex multiplicity, track angle distributions as well as track residual distributions are shown in Figures A.5 to A.7 in the Appendix.

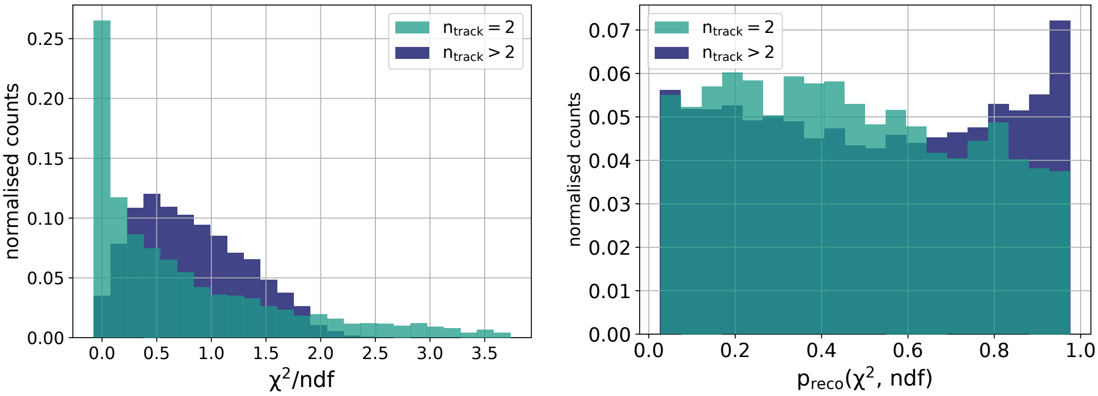

Figure 8.6: χ^2/ndf (left) and p-value distributions (right) of reconstructed Monte-Carlo simulation vertices. The histograms are normalised to one. The 2-track vertices only have one degree of freedom. Uncertainties provided for the true tracks are modelled without multiple scattering or misalignment.

To quantify the algorithms performance a vertex reconstruction efficiency ϵ_r is defined:

$$\epsilon_\mathrm{r} = \frac{n_\mathrm{reco}}{n_\mathrm{truth}} \,, \tag{8.10}$$

with n_reco and n_truth being the number of reconstructed and generated vertices. The reconstruction efficiency as function of the true vertex z position is shown in Figure 8.7.

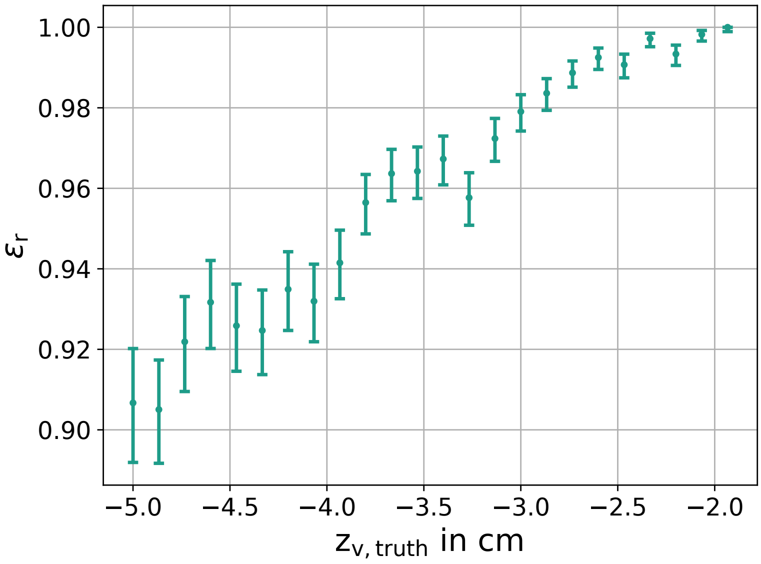

Figure 8.7: Reconstruction efficiency as function of z_v. The increasing lever arm for distant z_v increases the uncertainty on track projections towards the vertex and therefore decreases the reconstruction efficiency.

With the given uncertainties and $z_\mathrm{v,truth}$ distribution, the finding and fitting algorithm is able to reconstruct $(96.7 \pm 0.1)\,\%$ of vertices. The uncertainty given is the statistical uncertainty, computed according to Section 7.3.1.

The dependence of ϵ_r on z_v is founded in the increasing distance Δz for smaller z_v. The projection uncertainty of tracks to the vertex increases with increasing Δz, and a misreconstruction of vertices in form of track migration, the association of a track to the wrong vertex, and displaced $z_\mathrm{v,reco}$ are more likely.

With the resulting reconstruction efficiency and residual distributions (see Figure A.7) the vertex reconstruction procedure is considered well-suited for application to data.

8.3.2 Quality and multiplicity of reconstructed vertices

For this study, CHARM 2 run 1 is chosen representatively, since this run offers a high number of PoT (1.3×10^5) as well as a moderate amount of passive material. Figure 8.8 shows the vertex multiplicity for CHARM 2 run 1. With a ratio of 56 %, the majority of reconstructed vertices have only 2 tracks associated. Particles created in an interaction vertex in the target are subject to interaction, and a considerable fraction is stopped in the target or deflected outside the pixel detector acceptance. Thus, tracks from vertices further upstream in the target are less likely to be reconstructed, and a large part of vertices is left with 2 tracks, due to the challenging reconstruction environment. This effect is further discussed in Section 8.4. Considering these losses, it is distinguished between vertices with only 2 tracks, and vertices with multiple tracks associated for this study.

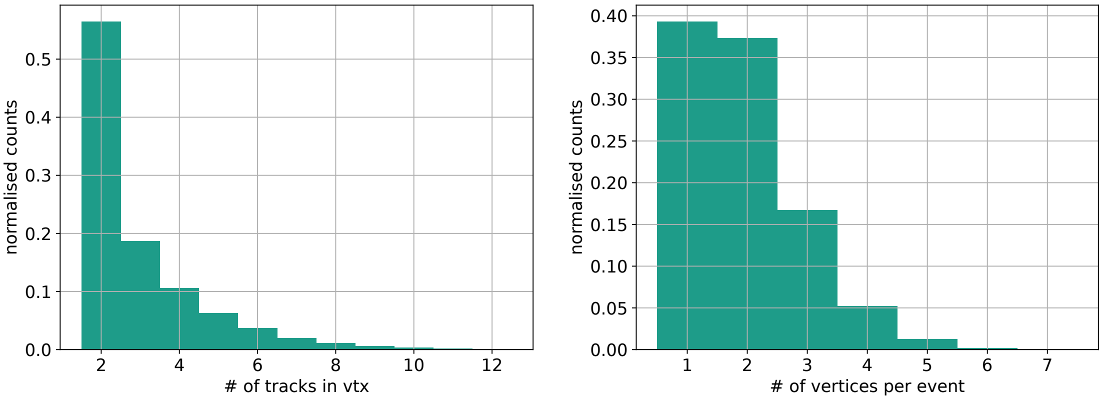

Figure 8.8: Multiplicity (left) and number of vertices (right) in CHARM 2 run 1. The majority of reconstructed vertices has 2 associated tracks, while in most events one or two vertices can be reconstructed. The histograms are normalised to one.

The χ^2/ndf and p-value distributions for fitted vertices in CHARM 2 run 1 are shown in Figure 8.9. The high-multiplicity vertices show a lower p-value. The lower fitting quality can be explained by larger multiple scattering and incomplete reconstruction for higher multiplicity: For a fixed primary energy, the single tracks from vertices with higher multiplicity have a lower momentum, compared to vertices with 2 tracks. The average scattering angle is higher for lower momentum particles (cf. Equation (5.6)), as is the probability to be absorbed in the target.

8.4 Reconstruction in different target configurations

Six different target configurations were used in the optimisation run for SHiP−charm to emulate target thicknesses between 0.16 and 1.6 nuclear interaction lengths. The run

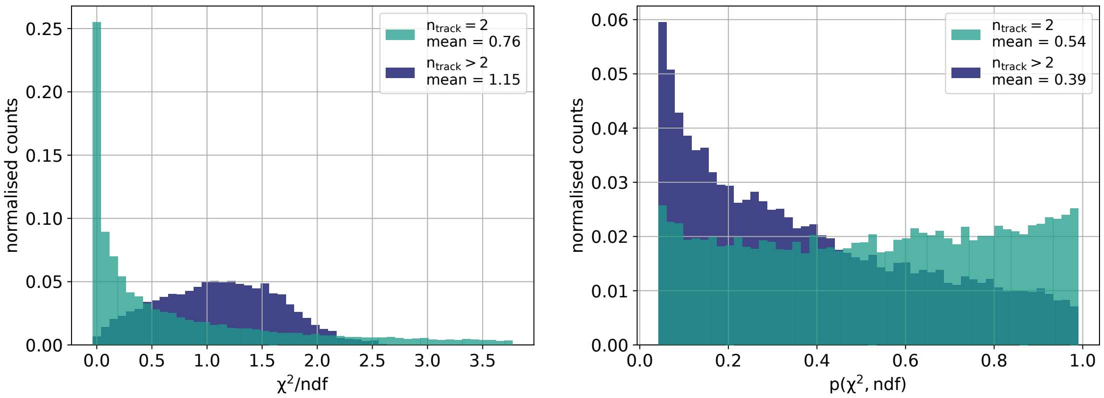

Figure 8.9: The χ^2/ndf (left) and p-value (right) distributions in CHARM 2 run 1 for vertices with 2 tracks and more than 2 tracks after vertex finding and fitting. The histograms are normalised to one. The 2-track vertices only have one degree of freedom.

configurations are listed in Table 7.1, and an illustration of the target configurations is available in Figure A.3 in the Appendix. The substantially different interaction lengths are also reflected in the vertices reconstructed in the pixel detector. Figure 8.10 shows the reconstructed z positions of vertices, z_v, in the runs with lowest and highest material budget. The position and extent of ECC and passive blocks (shaded areas) can be reconstructed. Furthermore, the algorithm is able to reconstruct the gap in between passive blocks and ECC without additional input information. The increase in the number of vertices with z matches the expected behaviour for absorption of charged particles in matter (cf. Section 5.1).

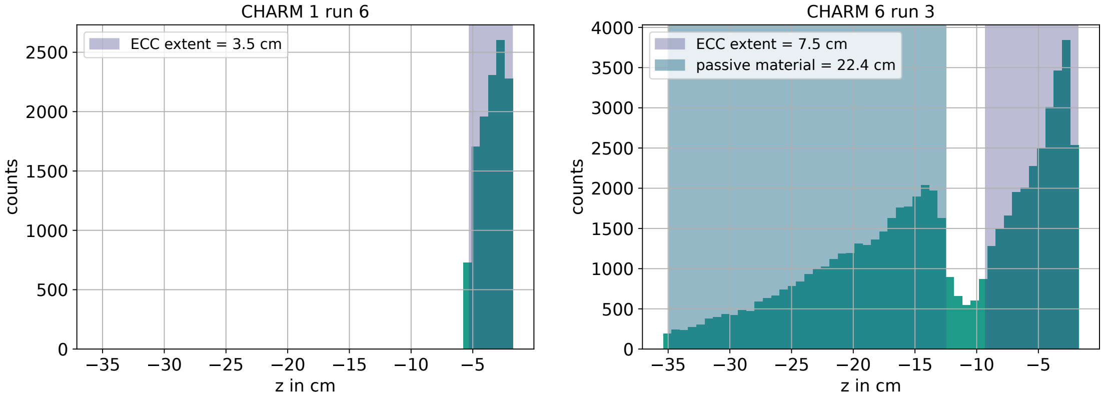

Figure 8.10: z_v of reconstructed vertices. For CHARM runs with lowest (left) and highest (right) nuclear interaction length. The gap between passive material and moving emulsion for CHARM 6 run 3 (right) is reconstructed by the vertexing algorithm.

The average z position of vertices, z_v, with respect to the vertex multiplicity is shown in Figure 8.11a. With increasing material budget, the measured average z_v for vertices with multiple tracks is shifted downstream. The absorption of secondary particles in the target reduces the number of tracks from upstream interaction available for reconstruction in the pixel detector, and consequently the average multiplicity for upstream vertices is reduced. This effect also influences the measured average number of tracks per vertex, as shown in Figure 8.11b. For increasing material budget the average number of tracks associated to a vertex is reduced. Figure 8.11b also shows the number of vertices per event, and in events with two or more vertices, there is at least one secondary vertex. Absorption in the target material also reduces the number of secondary vertices which can be reconstructed, as can be obtained from the plot.

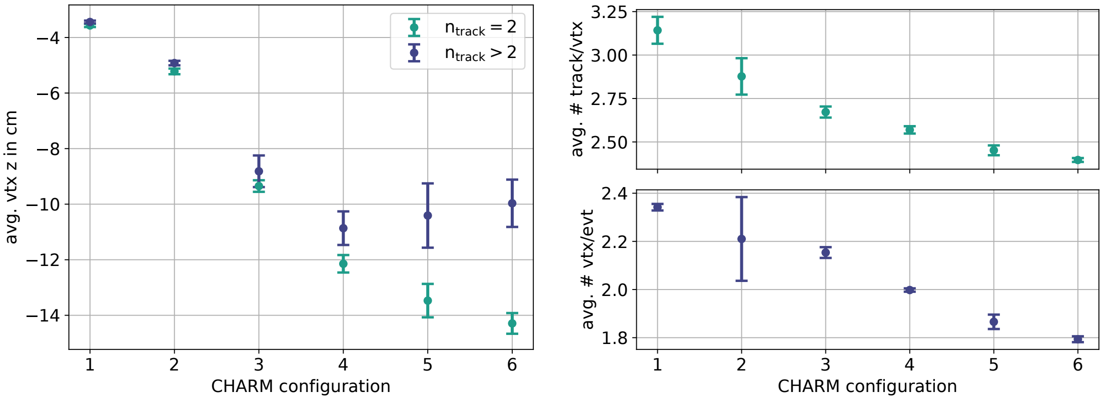

(a) **(b)**

Figure 8.11: Average z_v position of reconstructed vertices with 2 and more than 2 tracks (a). The position of reconstructed vertices is inversely proportional to the material budget. Vertex multiplicity (b, top) and number of vertices per event (b, bottom). Secondary particles are more likely to be absorbed in the target, which is reflected in the multiplicity of reconstructed vertices. The amount of passive material increases from 27 mm (CHARM 1) to 280 mm (CHARM 6). The target configurations are available in Table 7.1

8.5 Matching emulsion and pixel vertices

The matched emulsion tracks are associated to vertices reconstructed in the ECC[1], which can be compared to those reconstructed using the pixel detector standalone data. For this study, vertices are reconstructed in the same pixel detector track set as used for the track

---

[1] The selection criteria in the track matching procedure require emulsion tracks to be associated to a vertex with at least 6 tracks.

matching in Section 7.4. The vertices in emulsion data, which have been assigned to pixel detector events, are then matched to the set of reconstructed pixel vertices on an event basis.

The set of pixel detector vertices is first translated to the ECC reference frame, using the alignment parameters $\boldsymbol{\alpha}$ determined in Section 7.4[2], then the χ^2 between the emulsion and pixel detector vertex is calculated:

$$\chi^2 = \sum_i \frac{\left(\boldsymbol{x}_i^{\text{emu}} - \boldsymbol{x}_i^{\text{pix}}\right)^2}{\sigma_i^2}\,, \tag{8.11}$$

where $i = x, y, z$ is the spatial dimension, and σ_i the respective uncertainty in the pixel vertex position after translation to the ECC reference frame. The procedure is similar to the track matching, as all combinations of vertices in an event are considered, and the pairs with lowest χ^2 are chosen. The ndf in this case is 1. As for track matching, a $\chi^2 \leq 25$ selection cut is applied before vertices are considered a match (see Section 7.4.2 for information on the cut selection). Figure 8.12 shows the resulting χ^2 distribution for CHARM 1 run 6. The distribution is as expected for one degree of freedom.

A vertex matching rate ϵ_{v}, similar to the track matching rate in Equation (7.22) can be defined, and is used to evaluate the vertex matching result. For $(74.8 \pm 0.7)\,\%$ of emulsion vertices with at least one matched track, a vertex is reconstructed in the pixel detector data. The uncertainty given is the statistical uncertainty, determined according to Section 7.3.1. The matching rate as function of emulsion vertex z-position is displayed in Figure 8.12. With the available dataset, no significant dependence of the rate on z is observed. For a more detailed analysis, a larger dataset including spectrometer data would be necessary.

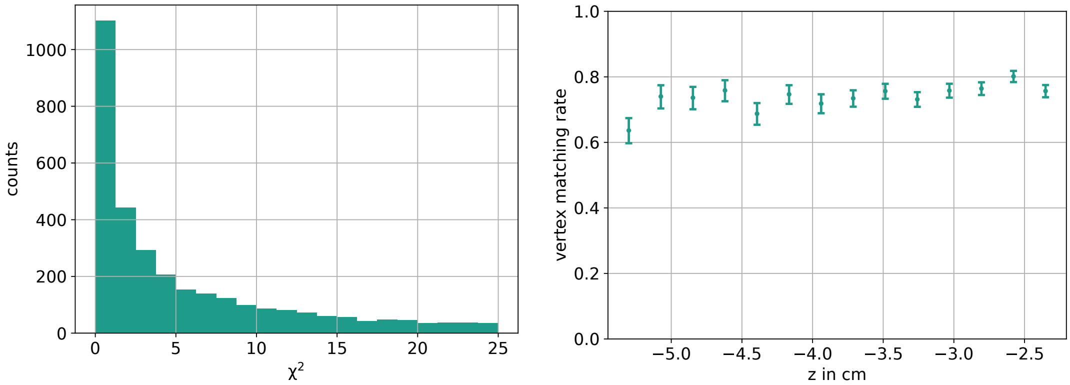

Figure 8.12: Matching χ^2 distribution with ndf $= 1$ for vertices reconstructed in the pixel detector matched with ECC vertices (left). Matching rate as function of emulsion vertex z (right).

---

[2] The full set of parameters is available in Table A.1 in the Appendix.

The event display in Figure 8.13 shows an event with matched tracks and the vertex reconstructed in pixel detector data. The 2-D views show the vertex position, the two half axes of the ellipse correspond to the uncertainty ($1\,\sigma$) in the respective dimension.

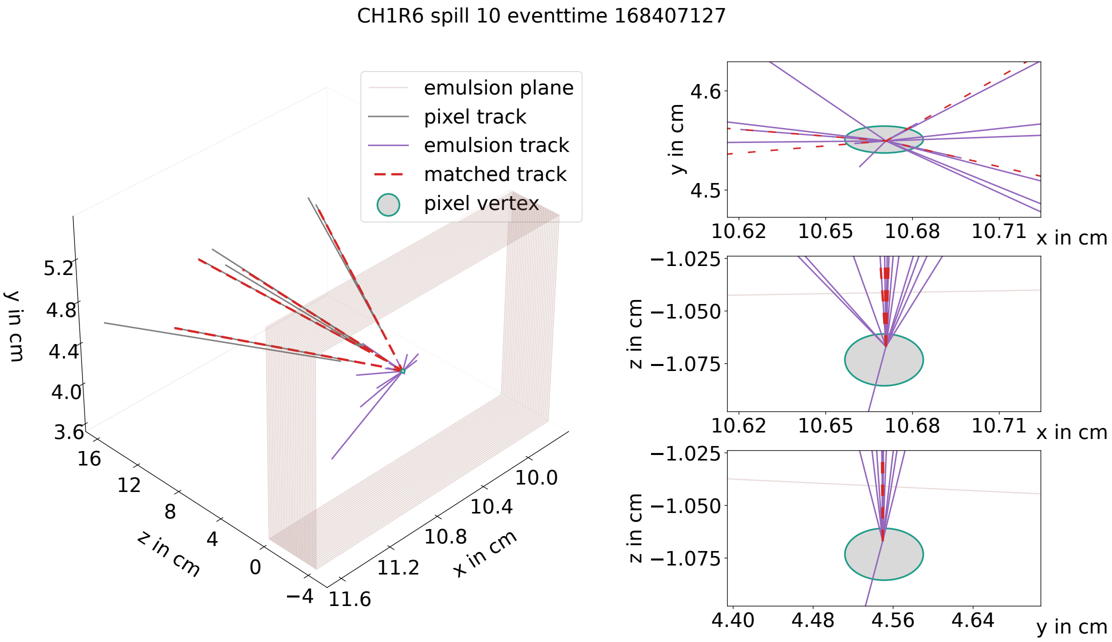

Figure 8.13: Event display with emulsion and pixel data as well as the matched pixel vertex in the emulsion reference frame. The extent of the ellipse is the uncertainty (1σ) in the vertex position for the respective dimensions.

8.5.1 Vertex displacement

The vertex matching rate is lower, compared to the track matching rate determined in Section 7.4.2. To investigate the influence of vertex displacement on the matching rate, the distance between matched pixel and emulsion vertices is displayed in Figure 8.14 for each coordinate $x_{\mathrm{v,m}}$, $y_{\mathrm{v,m}}$ and $z_{\mathrm{v,m}}$. The distributions are clearly influenced by the alignment, as discussed for the track matching in Section 7.4.2, as they follow similar double-Gaussian distributions. It may be noted that $\Delta z_{\mathrm{v,m}} \approx 10 \Delta y_{\mathrm{v,m}}$. The vertex z coordinate z_{v} depends on the track directions and intersection coordinates in the $x-z$ and $y-z$ plane. The uncertainties in the track parameters therefore have a large influence on the uncertainty in the $z_{\mathrm{v,m}}$ position of matched vertices. As for the track matching, the matching uncertainties are measured as the FWHM of the residual distributions and listed in Table 8.1. The uncertainties in $x_{\mathrm{v,m}}$ and $y_{\mathrm{v,m}}$ are slightly larger, compared to the track matching results in Table 7.2. As discussed, the uncertainty in $z_{\mathrm{v,m}}$ is mostly depending on $\sigma_{\theta_{xz}}, \sigma_{\theta_{yz}}$ and the projection distance.

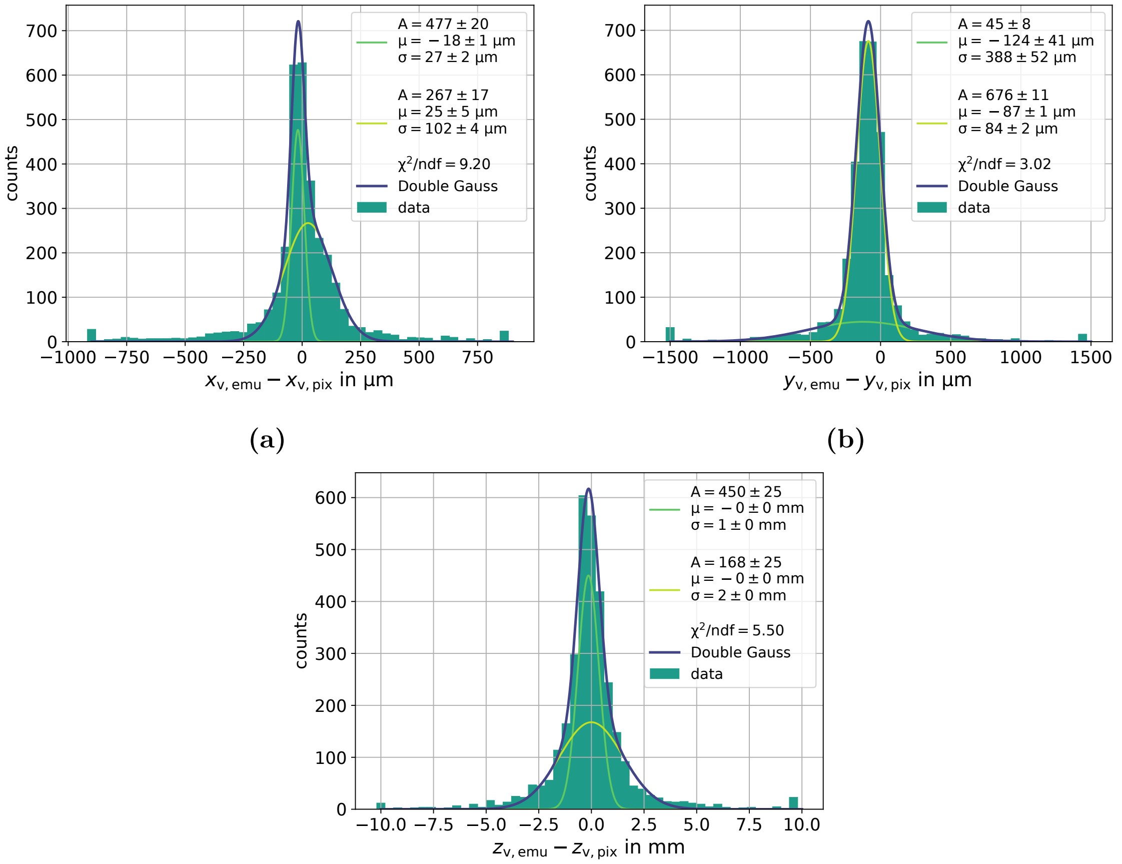

(a) **(b)**

(c)

Figure 8.14: Vertex matching residuals for the $x_{\mathrm{v,m}}$ (a), $y_{\mathrm{v,m}}$ (b) and $z_{\mathrm{v,m}}$ (c) dimensions. The distance in z is a factor ~ 10 larger compared to the x and y distances. The $z_{\mathrm{v,m}}$ position is especially sensitive to changes in the track direction.

Due to the influence of track directions, the contribution of multiple scattering to the displacement of vertices reconstructed in the pixel detector can not be neglected. To estimate the contribution of multiple scattering, tracks from ECC vertices which could not be matched are considered. The track segment in the last emulsion layer of these tracks is projected to the position of the associated emulsion vertex and the distance between track segment intersection coordinate $x_{\mathrm{s,proj}}$ and the emulsion vertex position $\Delta\boldsymbol{x} = \boldsymbol{x}_{\mathrm{s,proj}} - \boldsymbol{x}_{\mathrm{v,emu}}$ is computed. If the distance in any of the three dimensions $i = (x, y, z)$ exceeds the measured width in Table 8.1 by a factor 6, $\Delta x_i > 6\,\sigma_i$, the track is considered as displaced.

Parameter	Value
σ_x	54 µm
σ_y	103 µm
σ_z	775 µm

Table 8.1: Uncertainties in vertex position for matched vertices from fits on the residual distributions. The z position accuracy is dominated by the uncertainty in the track directions. Fit results and distributions are obtained from Figure 8.14.

A vertex can only be reconstructed by the pixel detector if at least two tracks are close enough. Therefore, any emulsion vertex is considered as not displaced, if two or more of the associated and matchable tracks are not displaced. Figure 8.15 shows the ratio of displaced vertices in the unmatched emulsion vertices as a function of the vertex z position, the ratio of displaced vertices among unmatched vertices is $(54 \pm 2)\,\%$ and proportional to the z distance. A significant contribution of multiple scattering in the ECC on the vertex matching rate is evident.

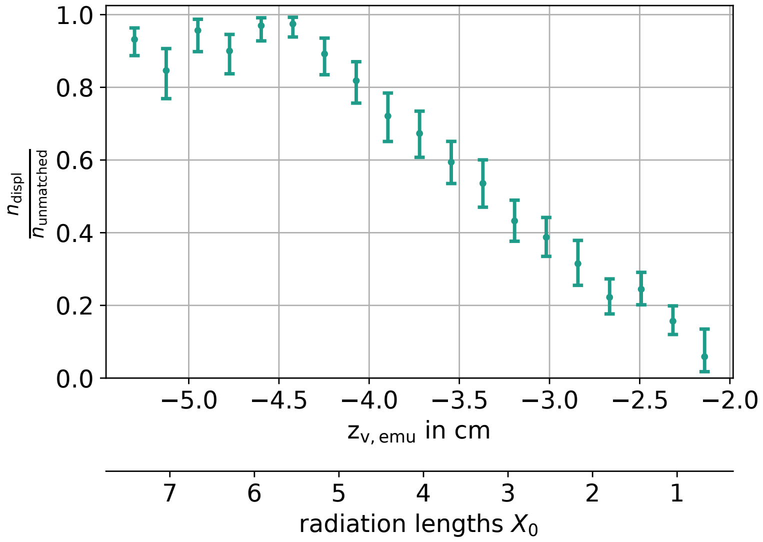

Figure 8.15: Ratio of displaced vertices to unmatched vertices as a function of $z_{\mathrm{v,emu}}$ in CHARM 1 run 6. As expected for multiple scattering, the displacement increases proportional to the distance travelled in the material.

8.6 Future studies

Altogether, it can be concluded that the reconstruction of vertices in pixel detector standalone data is demonstrated to be possible, while for further studies an improvement in reconstruction uncertainties and statistics, as well as a full event reconstruction, including momentum measurements from spectrometer data, would be beneficial.

It is also evident that the combination of ECC and pixel tracker makes a powerful tool to measure the charm cascade production. The ECC allows reconstruction of vertices deep inside the target material, and it allows tracking of particles, highly perturbed by multiple scattering, to the ECC exit. With the much longer lever arm and timing information, the pixel tracker can pass these tracks through the magnetic field to measure the particle momenta.

Data acquisition with the ECC, however, is complex. After irradiation, the single emulsion layers have to be scanned with dedicated hardware and the low radiation tolerance, intrinsic to the detection principle, prevents collection of large statistics. Correcting for the observed displacement by multiple scattering can enhance the quality of vertices reconstructed by the pixel tracker independently, enabling a simpler setup, and – without the occupancy limitation imposed by the emulsion detector – a much larger dataset.

A modified experiment to measure the charm (and possibly beauty) cascade production is therefore possible: A setup with a passive target, followed by the pixel tracker and a simple spectrometer could collect large datasets. The necessary calibrations of displacement and reconstruction rate can be determined in a dedicated measurement employing ECCs of different material budget and the pixel tracker, only.

9 Summary

In the search for dark matter candidates the SHiP experiment is proposed to collect 2×10^{20} events in a zero background environment. The experiment is built as a beam-dump setup for the 400 GeV proton beam of the SPS and is sensitive to several models of feebly interacting particles like dark photons, HNLs or axions.

For an accurate model of the SHiP physics processes, the charm-production cross section in a thick target needs to be known much more precicsely than what is currently measured. In the thick target especially secondary production of charmed hadrons is of interest. This cascade effect has so far never been measured, and known measurements for the charm cross section in thin targets bear large uncertainties. It is however expected, that the secondary production exceeds primary production by at least a factor of 2.

The SHiP−charm experiment is designed to measure the secondary charm interaction in a target with 0.16 - 1.6 nuclear interaction lengths. It is built from an active target, a spectrometer and a muon identification system. In the target, nuclear emulsions interleaved with sheets of tungsten or lead form an ECC with unmatched track and vertex reconstruction precision but without electronic event information. Within the scope of this work a pixel tracker was developed and operated to complement the ECC with timestamped event information, enabling full event reconstruction with the SHiP−charm spectrometer. An optimisation run with $\sim 3\,\%$ of the planned final dataset was performed. The pixel tracker DAQ was integrated with the common SHiP−charm DAQ system and within the SHiP−charm collaboration the reconstruction procedure to match ECC and pixel tracks was developed. The pixel tracker is built from 12 ATLAS IBL double-chip modules with a total of ~ 645000 readout channels. To the best of the author's knowledge, this is the largest detector using IBL modules outside of ATLAS.

In this work, the pixel tracker performance in the optimisation run was investigated. The tracker is found to detect hits with an efficiency of more than 99.6 %, compatible with previous results. Tracks are reconstructed with a projection uncertainty towards the ECC of 17 µm and 20 µm for the x and y dimension respectively, sufficient for event reconstruction including ECC data. The matching rate between ECC and pixel tracks was found to be $(82.6 \pm 0.4)\,\%$. The matching rate for particles as a function of their

momentum was estimated and is found to be adequate for efficient event reconstruction, with 81 % for particle momenta just above the acceptance, and a saturation of 87 % for momenta from 50 GeV/c on. The setup is found to be suited for a charm production cross-section measurement.
The tracks reconstructed in the pixel tracker are used for a standalone vertex reconstruction study. A reconstruction algorithm for vertices was developed within the scope of this work and vertices were reconstructed for targets of different nuclear interaction lengths. The influence of multiple scattering and absorption on the interaction remnants was observed. Finally, a vertex matching study was performed and (74.8 ± 0.7) % of timestamped vertices in the ECC could be reconstructed by the pixel tracker. The vertex matching however is influenced by displacement due to multiple scattering in the target material.

In conclusion, the pixel tracker performance and the tools developed for event reconstruction are well suited for a charm-production cross-section measurement and the combination of ECC and pixel tracker is a powerful tool for measuring the charm cascade production. For future measurements a simpler experiment, enabling larger datasets can be proposed: A short calibration campaign with ECC and pixel tracker to correct for multiple scattering, and a long measurement with a passive target followed by the pixel tracker and a spectrometer.

Appendix

Beam-dump facility and target

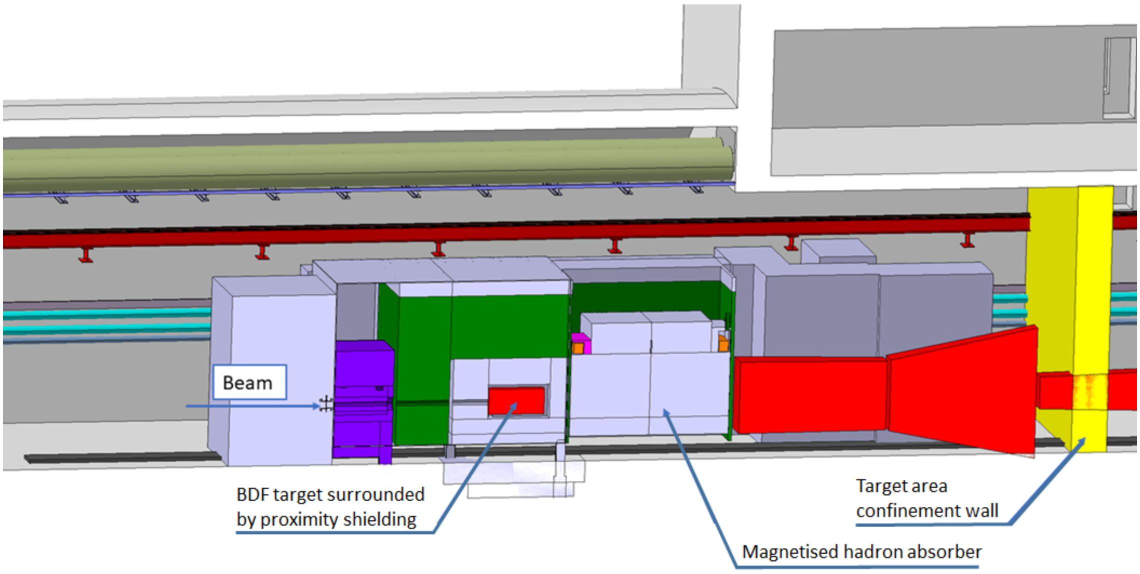

Figure A.1: Preliminary design of the target area at the ECN3 beam line. The target in the centre is shielded with iron blocks, the layer closest to the target is water cooled. A 5 cm thick iron window opens towards the active hadron absorber. From [76, p. 6].

ControlHost data format

```
struct DataFrameHeader
{
uint16_t size;  // Length of the data frame in bytes (including header).
uint16_t partitionId;   // Identifier of the subdetector and partition.
uint32_t cycleIdentifier;   // SHiP cycle identifier as received from TFC.
uint32_t frameTime; // Frame time in 25ns clock periods
uint16_t timeExtent;    // sequential trigger number
uint16_t flags; // Version, truncated, etc.
};

struct RawDataHit
{
uint16_t channelId; // Channel Identifier
uint16_t hitTime;   // Hit time, coarse 25ns based time in MSByte, fine
    time in LSByte
uint16_t extraData[0];  // Optional subdetector specific data items
};
```

Listing 1: Event data format as accepted by ControlHost. The number of RawDataHits is not limited, the number of hits which are read is determined by the size parameter in the header.

SHiP– charm run configurations

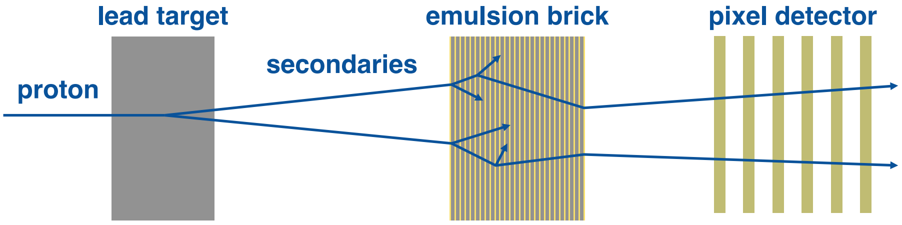

Figure A.2: Sketch of one event in the ECC and pixel detectors. The primary interaction vertex is located in the pre-shower brick. The pixel detector only measures secondary particles. The tracks reconstructed in the pixel detector can be projected towards the ECC surface.

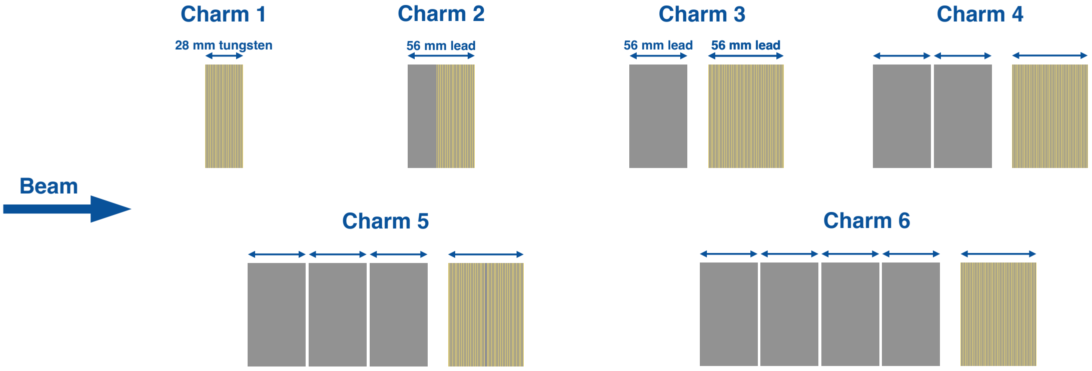

Figure A.3: Schematic layout of the six different target configurations. Adapted from [158, fig. 3].

Beam profile

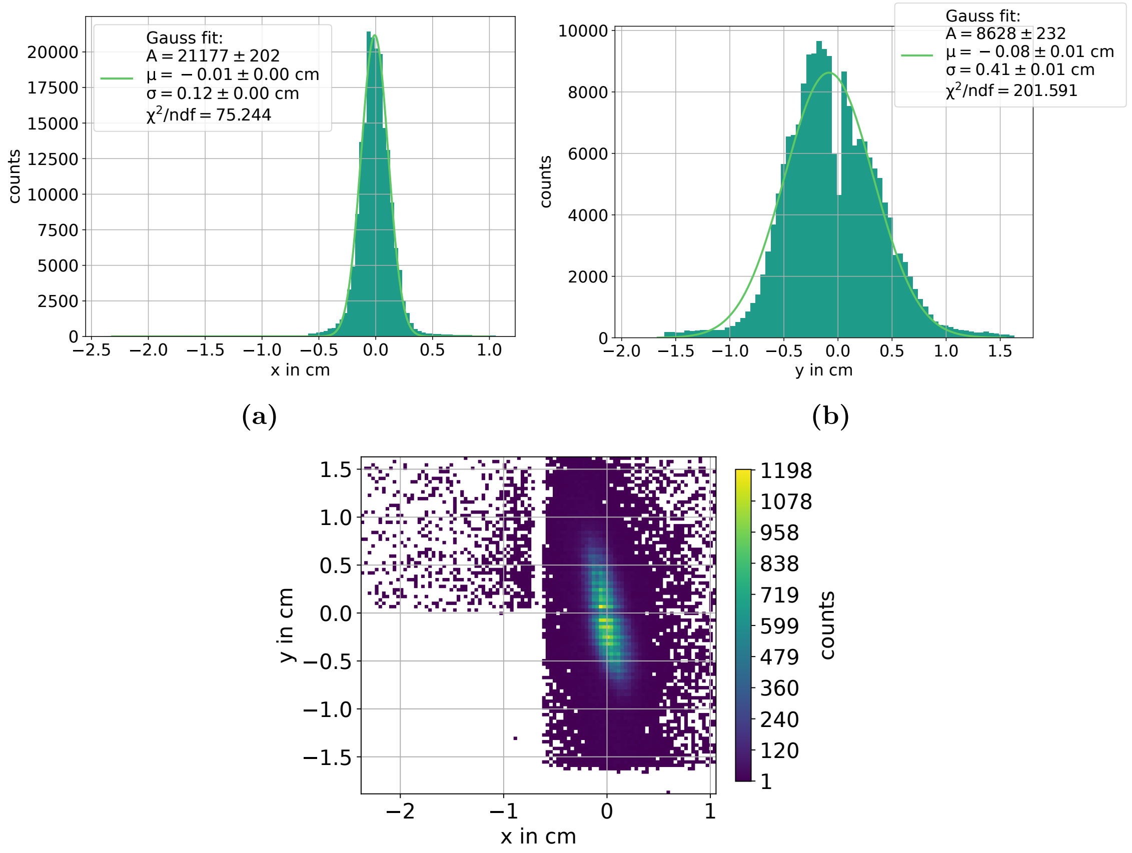

(a) **(b)**

(c)

Figure A.4: Beam profiles in x (a), y (b) and both dimensions (c) for a primary proton run, without target. The track intersection coordinates at the first plane of the pixel tracker are plotted.

Emulsion and pixel detector alignment

Spill	x_0 in cm	y_0 in cm	z_0 in cm	θ_{xz_0} in mrad	θ_{yz_0} in mrad	θ_{xy} in mrad	v_x in m/s	v_y in m/s
8	-0.409	-15.479	1.824	-1.3	0.1	-20.1	2.6104	-0.029
9	13.340	-15.625	1.830	-1.0	-0.1	-19.0	-2.6104	0.030
10	-0.378	-15.485	1.838	-0.3	0.1	-18.5	2.6101	-0.030
11	13.369	-15.603	1.840	-0.6	0.7	-18.9	-2.6100	0.029
12	-0.336	-15.440	1.843	-0.2	1.2	-18.4	2.6091	-0.029

Table A.1: Alignment parameters $\boldsymbol{\alpha}$ for emulsion and pixel detector in CHARM 1 run 6. The alignment algorithm considers each spill separately. The spill number is the one recorded by the pixel detector, based on the SoS signal. The run start command issued to the sub-detectors does not necessarily match the start of the ECC moving sequence.

Bron-Kerbosch algorithm

```
// define Bron-Kerbosch function
BronKerbosch(R,P,X):
    if P and X are empty:
        return R
    for each v∈P:
        BronKerbosch(R∪{v}, P∩N(v), X∩N(v))
        P = P\{v}
        X = X∪{v}
// call function with empty R, empty X and P=V = all vertices in the graph
BronKerbosch(R={}, V, X={})

```

Listing 2: Pseudo-code describing the Bron-Kerbosch algorithm to find all maximal cliques in a graph with the set of nodes V. The algorithm uses a recursive backtracking approach, where multiple states of sets are created by calling the algorithm on subsets of the input nodes. R represents the clique under construction, P is the set of nodes adjacent to R and X is the exclusion set, containing already processed nodes $v \in V$. $N(v)$ is the neighbourhood of v, i.e. the set of nodes connected to v by an edge.

Monte-Carlo simulation vertex sample

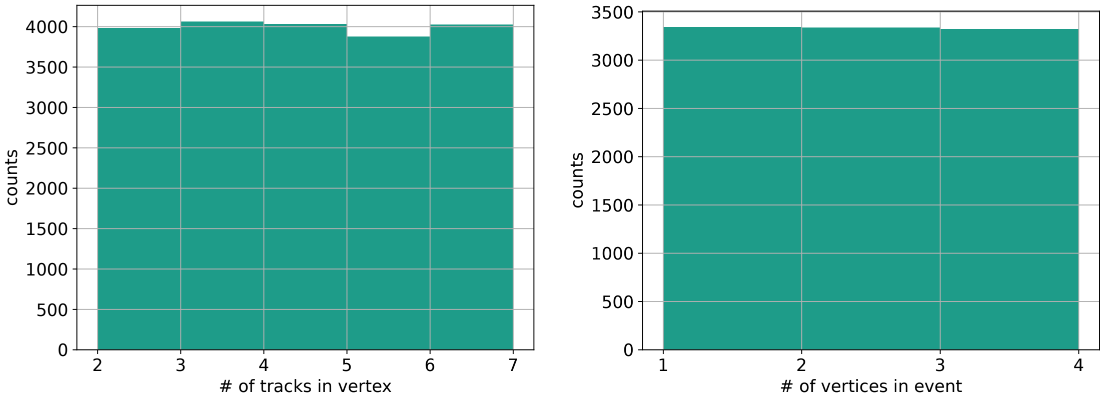

Figure A.5: True vertex multiplicity (left) and number of vertices per event (right).

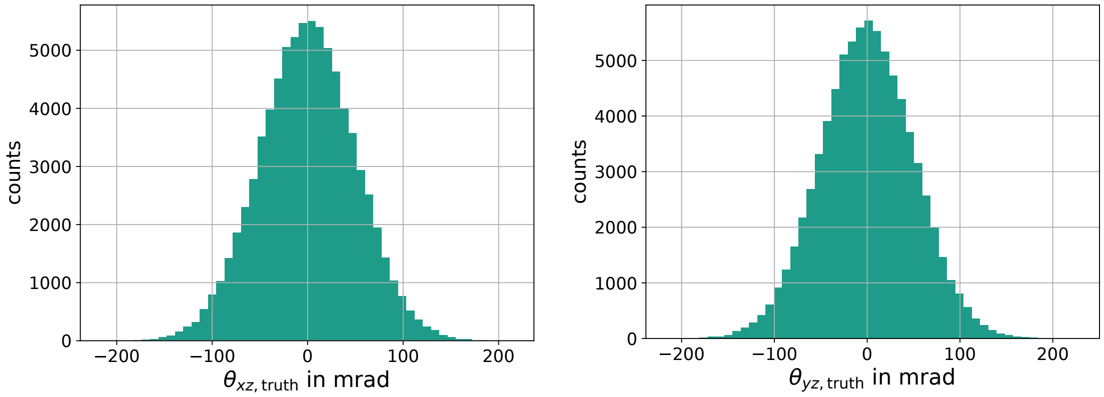

Figure A.6: Track opening angle θ_{xz} (left) and θ_{yz} (right) of true tracks in vertex sample. The angles are limited to emulate the opening angle of the pixel tracker.

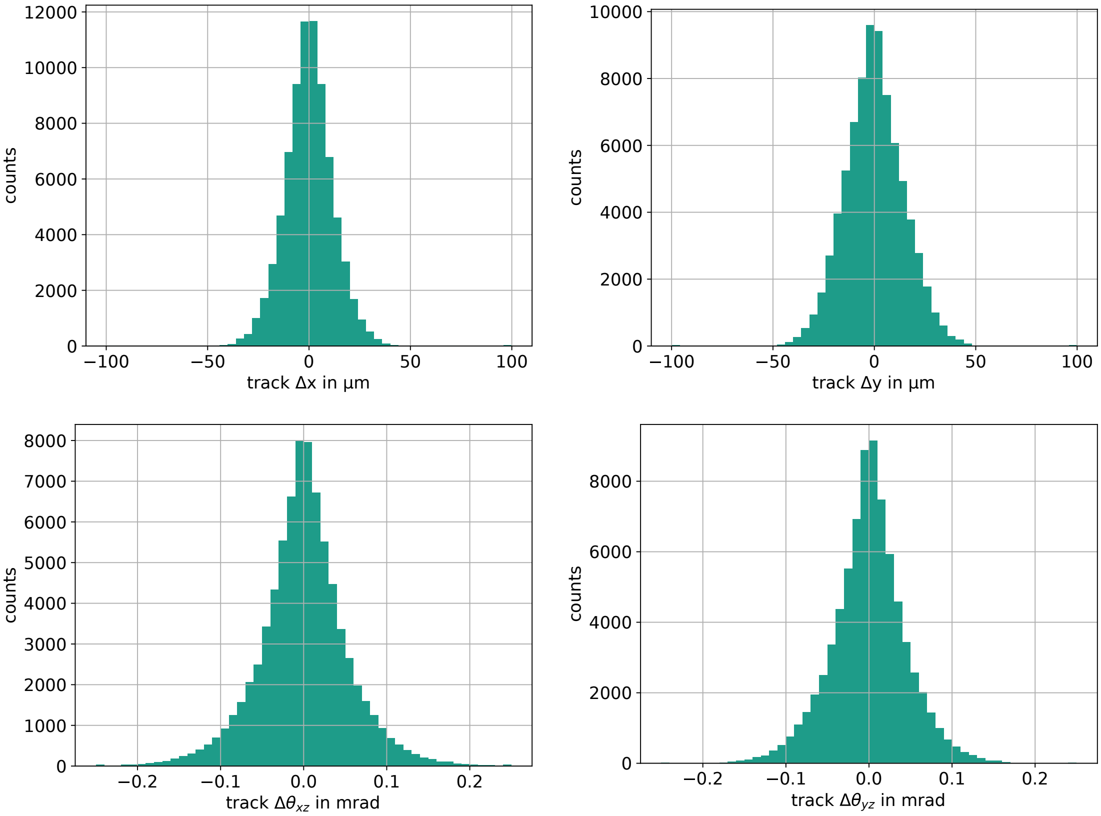

Figure A.7: Residuals $\Delta q = q_{\text{truth}} - q_{\text{reco}}$ with $q = (x, y, \theta_{xz}, \theta_{yz})$ for reconstructed tracks in all four parameters. The uncertainties provided for the Monte-Carlo sample are the measured projection resolutions for the track intersection coordinates, and a $\sigma_z = 50\,\mu\text{m}$ for the computation of the uncertainties in the opening angle.

Abbreviations

νMSM	Neutrino Minimal Standard Model	10
ALP	Axion-Like Particle	10
BAU	Baryon Asymmetry of the Universe	9
BDF	Beam-Dump Facility	23
BEH	Brout-Englert-Higgs	4
BSM	Beyond the Standard Model	10
CC	Charged Current	20
CCDIS	Charged-Current Deep-Inelastic Scattering	20
CES	Compact Emulsion Spectrometer	30
CMOS	Complementary Metal-Oxide-Semiconductor	59
CSA	Charge-Sensitive Amplifier	61
DAQ	Data Acquisition	37
DC module	Double-Chip module	60
ECC	Emulsion Cloud Chamber	2
EoR	End of Run	70
EoS	End of Spill	44
FE-I4	Front-End I4	60
FIFO	First-In-First-Out	68
FPGA	Field-Programmable Gate Array	66
FWHM	Full Width at Half Maximum	90
HNL	Heavy Neutral Lepton	15
HS	Hidden Sector	10

HSDS	Hidden Sector Decay Spectrometer	24
HWHM	Half Width at Half Maximum	82
IBL	Insertable B Layer	59
LHC	Large Hadron Collider	1
MIP	Minimum Ionising Particle	39
MPV	Most Probable Value	50
ndf	Number of Degrees of Freedom	79
NLO	Next-To-Leading Order	36
pdf	Parton Distribution Function	36
Pmod	Peripheral module Interface	67
POCA	Point of Closest Approach	101
PoT	Protons on Target	25
pQCD	Perturbative Quantum Chromodynamics	36
QCD	Quantum Chromodynamics	7
QFT	Quantum Field Theory	3
ROI	Region of Interest	77
RPC	Resistive Plate Chamber	29
SciFi	Scintillating-Fiber	31
SHiP	Search for Hidden Particles	iii
SM	Standard Model of Elementary Particle Physics	1
SND	Scattering and Neutrino Detector	24
SoR	Start of Run	44
SoS	Start of Spill	41
SPS	Super Proton Synchrotron	1
TCP	Transmission Control Protocol	68
TLU	Trigger Logic Unit	68
ToT	Time-Over-Threshold	61
TTL	Transistor-Transistor Logic	66

TZM	Titanium–Zirconium–Molybdenum	26

Bibliography

[1] ATLAS collaboration, *Observation of a new particle in the search for the Standard Model Higgs boson with the ATLAS detector at the LHC*, Phys. Lett. B **716** (2012), p. 1, DOI: `10.1016/j.physletb.2012.08.020`.

[2] CMS collaboration, *Observation of a new boson at a mass of 125 GeV with the CMS experiment at the LHC*, Phys. Lett. B **716** (2012), p. 30, DOI: `10.1016/j.physletb.2012.08.021`.

[3] S. Alekhin et al., *A facility to search for hidden particles at the CERN SPS: the SHiP physics case*, Rep. Prog. Phys. **79** (2016), p. 124201, DOI: `10.1088/0034-4885/79/12/124201`.

[4] J. Beacham et al., *Physics beyond colliders at CERN: beyond the Standard Model working group report*, J. Phys. G: Nucl. Part. Phys. **47** (2020), p. 010501, DOI: `10.1088/1361-6471/ab4cd2`.

[5] S. N. Gninenko, D. S. Gorbunov and M. E. Shaposhnikov, *Search for GeV-scale sterile neutrinos responsible for active neutrino oscillations and baryon asymmetry of the Universe*, 2013, DOI: `10.48550/ARXIV.1301.5516`.

[6] F. Englert and R. Brout, *Broken Symmetry and the Mass of Gauge Vector Mesons*, Phys. Rev. Lett. **13** (1964), p. 321, DOI: `10.1103/physrevlett.13.321`.

[7] P. W. Higgs, *Broken Symmetries and the Masses of Gauge Bosons*, Phys. Rev. Lett. **13** (1964), p. 508, DOI: `10.1103/physrevlett.13.508`.

[8] P. Higgs, *Broken symmetries, massless particles and gauge fields*, Phys. Lett. **12** (1964), p. 132, DOI: `10.1016/0031-9163(64)91136-9`.

[9] D. Griffiths, *Introduction to elementary particles*, Wiley-VCH, 2008.

[10] M. Thomson, *Modern Particle Physics*, Cambridge University Press, 2013, DOI: `10.1017/CBO9781139525367`.

[11] J. Ellis, *Higgs Physics*, 2013 European School of High-Energy Physics, CERN, 2015, p. 117, DOI: `10.5170/CERN-2015-004.117`.

[12] M. E. Peskin and D. V. Schroeder, *An Introduction to quantum field theory*, Addison-Wesley, 1995.

[13] C. S. Wu et al., *Experimental Test of Parity Conservation in Beta Decay*, Phys. Rev. **105** (1957), p. 1413, DOI: 10.1103/physrev.105.1413.

[14] H. Frauenfelder et al., *Parity and the Polarization of Electrons from* Co^{60}, Phys. Rev. **106** (1957), p. 386, DOI: 10.1103/physrev.106.386.

[15] E. C. G. Sudarshan and R. E. Marshak, *Chirality Invariance and the Universal Fermi Interaction*, Phys. Rev. **109** (1958), p. 1860, DOI: 10.1103/physrev.109.1860.2.

[16] R. P. Feynman and M. Gell-Mann, *Theory of the Fermi Interaction*, Phys. Rev. **109** (1958), p. 193, DOI: 10.1103/physrev.109.193.

[17] S. L. Glashow, *Partial-symmetries of weak interactions*, Nucl. Phys. **22** (1961), p. 579, DOI: 10.1016/0029-5582(61)90469-2.

[18] A. Salam and J. C. Ward, *On a gauge theory of elementary interactions*, Il Nuovo Cimento **19** (1961), p. 165, DOI: 10.1007/bf02812723.

[19] S. Weinberg, *A Model of Leptons*, Phys. Rev. Lett. **19** (1967), p. 1264, DOI: 10.1103/physrevlett.19.1264.

[20] G. Altarelli, *The Standard Model of Electroweak Interactions*, *Physics and Methods. Theory and Experiments*, ed. by H. Schopper, Springer, 2008, chap. 3, p. 19, DOI: 10.1007/978-3-540-74203-6_3.

[21] A. Pich, *The Standard Model of Electroweak Interactions*, *Lecture at the 6th Joint CERN-Fermilab Hadron Collider Physics Summer School, CERN 2011*, CERN, 2012, DOI: 10.5170/CERN-2012-001.1.

[22] M. Kobayashi and T. Maskawa, *CP-Violation in the Renormalizable Theory of Weak Interaction*, Prog. Theor. Phys. **49** (1973), p. 652, DOI: 10.1143/ptp.49.652.

[23] H. Fritzsch, M. Gell-Mann and H. Leutwyler, *Advantages of the color octet gluon picture*, Phys. Lett. B **47** (1973), p. 365, DOI: 10.1016/0370-2693(73)90625-4.

[24] R. K. Ellis, W. J. Stirling and B. R. Webber, *QCD and Collider Physics*, Cambridge University Press, 1996, DOI: 10.1017/cbo9780511628788.

[25] D. Buttazzo et al., *Investigating the near-criticality of the Higgs boson*, JHEP **12** (2013), p. 89, DOI: 10.1007/jhep12(2013)089.

[26] F. Bezrukov et al., *Higgs boson mass and new physics*, JHEP **10** (2012), p. 140, DOI: 10.1007/jhep10(2012)140.

[27] D. N. Spergel et al., *First-Year Wilkinson Microwave Anisotropy Probe (WMAP) Observations: Determination of Cosmological Parameters*, ApJS **148** (2003), p. 175, DOI: `10.1086/377226`.

[28] D. N. Spergel et al., *Three-Year Wilkinson Microwave Anisotropy Probe (WMAP) Observations: Implications for Cosmology*, ApJS **170** (2007), p. 377, DOI: `10.1086/513700`.

[29] R. Massey, T. Kitching and J. Richard, *The dark matter of gravitational lensing*, Rep. Prog. Phys. **73** (2010), p. 086901, DOI: `10.1088/0034-4885/73/8/086901`.

[30] E. Corbelli and P. Salucci, *The extended rotation curve and the dark matter halo of M33*, MNRAS **311** (2000), p. 441, DOI: `10.1046/j.1365-8711.2000.03075.x`.

[31] Planck collaboration, *Planck 2018 results*, Astron. Astrophys. **641** (2020), A6, DOI: `10.1051/0004-6361/201833910`.

[32] KATRIN collaboration, *Direct neutrino-mass measurement with sub-electronvolt sensitivity*, Nature Physics **18** (2022), p. 160, DOI: `10.1038/s41567-021-01463-1`.

[33] E. Majorana, *Teoria simmetrica dell'elettrone e del positrone*, Il Nuovo Cimento **14** (1937), reproduced and translated in *Ettore Majorana Scientific Papers: On occasion of the centenary of his birth*, Springer Berlin Heidelberg, 2006, p. 171, DOI: `10.1007/bf02961314`.

[34] P. Minkowski, *$\mu \to e\gamma$ at a rate of one out of 10^9 muon decays?*, Phys. Lett. B **67** (1977), p. 421, DOI: `10.1016/0370-2693(77)90435-x`.

[35] T. Yanagida, *Horizontal gauge symmetry and masses of neutrinos*, Conf. Proc. C **7902131** (1979), p. 95, URL: `https://neutrino.kek.jp/seesaw/KEK-79-18-Yanagida.pdf`.

[36] M. Gell-Mann, P. Ramond and R. Slansky, *Complex Spinors and Unified Theories*, Conf. Proc. C **790927** (1979), p. 315, DOI: `10.48550/arXiv.1306.4669`.

[37] R. L. Workman et al., *Review of Particle Physics*, Prog. Theor. Exp. Phys. **2022** (2022), DOI: `10.1093/ptep/ptac097`.

[38] A. D. Sakharov, *Violation of CP invariance, C asymmetry, and baryon asymmetry of the universe*, Pisma Zh. Eksp. Teor. Fiz. **5** (1967), p. 32, DOI: `10.1070/pu1991v034n05abeh002497`.

[39] A. Riotto and M. Trodden, *Recent Progress in Baryogenesis*, Annu. Rev. Nucl. Part. Sci. **49** (1999), p. 35, DOI: `10.1146/annurev.nucl.49.1.35`.

[40] B. Batell, M. Pospelov and A. Ritz, *Exploring portals to a hidden sector through fixed targets*, Phys. Rev. D **80** (2009), p. 095024, DOI: `10.1103/physrevd.80.095024`.

[41] ATLAS collaboration, *Search for high-mass dilepton resonances in pp collisions at* $\sqrt{s} = 8$ *TeV with the ATLAS detector*, Phys. Rev. D **90** (2014), p. 052005, DOI: `10.1103/physrevd.90.052005`.

[42] CMS collaboration, *Search for physics beyond the standard model in dilepton mass spectra in proton-proton collisions at* $\sqrt{s} = 8$ *TeV*, JHEP **4** (2015), p. 25, DOI: `10.1007/jhep04(2015)025`.

[43] SHiP collaboration, *Sensitivity of the SHiP experiment to light dark matter*, JHEP **4** (2021), p. 199, DOI: `10.1007/jhep04(2021)199`.

[44] M. Pospelov, A. Ritz and M. Voloshin, *Secluded WIMP dark matter*, Phys. Lett. B **662** (2008), p. 53, DOI: `10.1016/j.physletb.2008.02.052`.

[45] D. Gorbunov, A. Makarov and I. Timiryasov, *Decaying light particles in the SHiP experiment: Signal rate estimates for hidden photons*, Phys. Rev. D **91** (2015), p. 035027, DOI: `10.1103/physrevd.91.035027`.

[46] SHiP collaboration, *Sensitivity of the SHiP experiment to dark photons decaying to a pair of charged particles*, EPJC **81** (2021), p. 451, DOI: `10.1140/epjc/s10052-021-09224-3`.

[47] J. Blümlein and J. Brunner, *New exclusion limits on dark gauge forces from proton Bremsstrahlung in beam-dump data*, Phys. Lett. B **731** (2014), p. 320, DOI: `10.1016/j.physletb.2014.02.029`.

[48] A. Celentano et al., *New production channels for light dark matter in hadronic showers*, Phys. Rev. D **102** (2020), p. 075026, DOI: `10.1103/physrevd.102.075026`.

[49] C. Bird et al., *Dark Matter Particle Production in* $b \to s$ *Transitions with Missing Energy*, Phys. Rev. Lett. **93** (2004), p. 201803, DOI: `10.1103/physrevlett.93.201803`.

[50] G. Lanfranchi, *Sensitivity of the SHiP experiment to a light scalar particle mixing with the Higgs*, CERN note, 2017, URL: `https://cds.cern.ch/record/2243034`.

[51] G. Lanfranchi, M. Pospelov and P. Schuster, *The Search for Feebly Interacting Particles*, Annu. Rev. Nucl. Part. Sci. **71** (2021), p. 279, DOI: `10.1146/annurev-nucl-102419-055056`.

[52] J. D. Clarke, R. Foot and R. R. Volkas, *Phenomenology of a very light scalar* $(100\,\mathrm{MeV} < m_h < 10\,\mathrm{GeV})$ *mixing with the SM Higgs*, JHEP **02** (2014), p. 123, DOI: `10.1007/jhep02(2014)123`.

[53] T. Asaka, S. Blanchet and M. Shaposhnikov, *The* ν*MSM, dark matter and neutrino masses*, Phys. Lett. B **631** (2005), p. 151, DOI: `10.1016/j.physletb.2005.09.070`.

[54] T. Asaka and M. Shaposhnikov, *The νMSM, dark matter and baryon asymmetry of the universe*, Phys. Lett. B **620** (2005), p. 17, DOI: 10.1016/j.physletb.2005.06.020.

[55] L. Canetti and M. Shaposhnikov, *Baryon asymmetry of the Universe in the νMSM*, JCAP **2010** (2010), p. 1, DOI: 10.1088/1475-7516/2010/09/001.

[56] W. Bonivento et al., *Proposal to Search for Heavy Neutral Leptons at the SPS*, CERN, 2013, DOI: 10.48550/arXiv.1310.1762.

[57] K. Bondarenko et al., *Phenomenology of GeV-scale heavy neutral leptons*, JHEP **11** (2018), p. 032, DOI: 10.1007/jhep11(2018)032.

[58] S. Weinberg, *The U(1) problem*, Phys. Rev. D **11** (1975), p. 3583, DOI: 10.1103/physrevd.11.3583.

[59] G. 't Hooft, *Computation of the quantum effects due to a four-dimensional pseudoparticle*, Phys. Rev. D **14** (1976), p. 3432, DOI: 10.1103/physrevd.14.3432.

[60] R. D. Peccei, *The Strong CP Problem and Axions*, *Lecture Notes in Physics*, Springer Berlin Heidelberg, 2008, p. 3, DOI: 10.1007/978-3-540-73518-2_1.

[61] C. Abel et al., *Measurement of the Permanent Electric Dipole Moment of the Neutron*, Phys. Rev. Lett. **124** (2020), p. 081803, DOI: 10.1103/physrevlett.124.081803.

[62] R. D. Peccei and H. R. Quinn, *CP Conservation in the Presence of Pseudoparticles*, Phys. Rev. Lett. **38** (1977), p. 1440, DOI: 10.1103/physrevlett.38.1440.

[63] F. Wilczek, *Problem of Strong P and T Invariance in the Presence of Instantons*, Phys. Rev. Lett. **40** (1978), p. 279, DOI: 10.1103/physrevlett.40.279.

[64] M. Dine, W. Fischler and M. Srednicki, *A simple solution to the strong CP problem with a harmless axion*, Phys. Lett. B **104** (1981), p. 199, DOI: 10.1016/0370-2693(81)90590-6.

[65] J. Jaeckel and A. Ringwald, *The Low-Energy Frontier of Particle Physics*, Annu. Rev. Nucl. Part. Sci. **60** (2010), p. 405, DOI: 10.1146/annurev.nucl.012809.104433.

[66] A. Halprin, C. M. Andersen and H. Primakoff, *Photonic Decay Rates and Nuclear-Coulomb-Field Coherent Production Processes*, Phys. Rev. **152** (1966), p. 1295, DOI: 10.1103/physrev.152.1295.

[67] B. Döbrich et al., *ALPtraum: ALP production in proton beam dump experiments*, JHEP **02** (2016), p. 018, DOI: 10.1007/jhep02(2016)018.

[68] Z. Maki, M. Nakagawa and S. Sakata, *Remarks on the Unified Model of Elementary Particles*, Prog. Theor. Phys. **28** (1962), p. 870, DOI: 10.1143/ptp.28.870.

[69] B. Pontecorvo, *Inverse beta processes and nonconservation of lepton charge*, Zh. Eksp. Teor. Fiz. **34** (1957), reproduced and translated in *Sov. Phys. JETP* 7 (1958), p. 247, URL: `http://jetp.ras.ru/cgi-bin/e/index/e/7/1/p172?a=list`.

[70] C. L. Cowan et al., *Detection of the Free Neutrino: a Confirmation*, Science **124** (1956), p. 103, DOI: `10.1126/science.124.3212.103`.

[71] G. Danby et al., *Observation of High-Energy Neutrino Reactions and the Existence of Two Kinds of Neutrinos*, Phys. Rev. Lett. **9** (1962), p. 36, DOI: `10.1103/physrevlett.9.36`.

[72] DONuT collaboration, *Final tau-neutrino results from the DONuT experiment*, Phys. Rev. D **78** (2008), p. 052002, DOI: `10.1103/physrevd.78.052002`.

[73] Super-Kamiokande collaboration, *Measurement of the tau neutrino cross section in atmospheric neutrino oscillations with Super-Kamiokande*, Phys. Rev. D **98** (2018), p. 052006, DOI: `10.1103/physrevd.98.052006`.

[74] OPERA collaboration, *Final Results of the OPERA Experiment on ν_τ Appearance in the CNGS Neutrino Beam*, Phys. Rev. Lett. **120** (2018), p. 211801, DOI: `10.1103/physrevlett.120.211801`.

[75] R. Maciuła et al., *Production asymmetry of ν_τ neutrinos and $\overline{\nu}\tau$ antineutrinos from a fixed target experiment SHiP*, JHEP **01** (2020), p. 116, DOI: `10.1007/jhep01(2020)116`.

[76] SHiP Collaboration, *BDF / SHiP at the ECN3 high-intensity facility - Letter of Intent*, 2022, URL: `https://cds.cern.ch/record/2839677`.

[77] A. Benvenuti et al., *Observation of New-Particle Production by High-Energy Neutrinos and Antineutrinos*, Phys. Rev. Lett. **34** (1975), p. 419, DOI: `10.1103/physrevlett.34.419`.

[78] G. De Lellis, P. Migliozzi and P. Santorelli, *Charm physics with neutrinos*, Phys. Rep. **399** (2004), p. 227, DOI: `10.1016/j.physrep.2004.07.005`.

[79] SHiP collaboration, *A facility to Search for Hidden Particles (SHiP) at the CERN SPS*, 2015, DOI: `10.48550/ARXIV.1504.04956`.

[80] CCFR collaboration, *Determination of the strange quark content of the nucleon from a next-to-leading-order QCD analysis of neutrino charm production*, Z. Phys. C **65** (1995), p. 189, DOI: `10.1007/bf01571875`.

[81] N. Schmitz, *Neutrinophysik*, Vieweg+Teubner Verlag, 1997, DOI: `10.1007/978-3-322-80114-2`.

[82] G. De Lellis et al., *Search for charmed pentaquarks in high energy anti-neutrino interactions*, Nucl. Phys. B **763** (2007), p. 268, DOI: `10.1016/j.nuclphysb.2006.11.025`.

[83] LHCb collaboration, *Observation of a Narrow Pentaquark State, $P_c(4312)^+$, and of the Two-Peak Structure of the $P_c(4450)^+$*, Phys. Rev. Lett. **122** (2019), p. 222001, DOI: `10.1103/physrevlett.122.222001`.

[84] C. Ahdida et al., *CERN Yellow Reports: Monographs, Vol 2 (2020): SPS Beam Dump Facility: Comprehensive Design Study*, tech. rep., CERN, 2020, DOI: `10.23731/CYRM-2020-002`.

[85] SHiP collaboration, *The experimental facility for the Search for Hidden Particles at the CERN SPS*, JINST **14** (2019), P03025, DOI: `10.1088/1748-0221/14/03/p03025`.

[86] B. Goddard et al., *Extraction and beam transfer for the SHiP facility*, tech. rep., SHiP-TP-2015-A3, CERN, 2016, URL: `https://edms.cern.ch/document/1495859`.

[87] E. Lopez Sola et al., *Design of a high power production target for the beam dump facility at CERN*, Phys. Rev. Accel. Beams **22** (2019), p. 113001, DOI: `10.1103/physrevaccelbeams.22.113001`.

[88] E. Lopez Sola et al., *Beam impact tests of a prototype target for the beam dump facility at CERN: Experimental setup and preliminary analysis of the online results*, Phys. Rev. Accel. Beams **22** (2019), p. 123001, DOI: `10.1103/physrevaccelbeams.22.123001`.

[89] K. Kershaw et al., *Design Development for the Beam Dump Facility Target Complex at CERN*, JINST **13** (2018), P10011, DOI: `10.1088/1748-0221/13/10/p10011`.

[90] J. Steichen, *Tensile properties of neutron irradiated TZM and tungsten*, JNM **60** (1976), p. 13, DOI: `10.1016/0022-3115(76)90112-4`.

[91] SHiP collaboration, *The active muon shield in the SHiP experiment*, JINST **12** (2017), P05011, DOI: `10.1088/1748-0221/12/05/p05011`.

[92] SHiP collaboration, *Measurement of the muon flux from 400 GeV/c protons interacting in a thick molybdenum/tungsten target*, EPJC **80** (2020), p. 284, DOI: `10.1140/epjc/s10052-020-7788-y`.

[93] SHiP collaboration, *The SHiP experiment at the proposed CERN SPS Beam Dump Facility*, EPJC **82** (2022), p. 486, DOI: `10.1140/epjc/s10052-022-10346-5`.

[94] A. Buonaura, *Studiy of ν_τ properties with the SHiP experiment*, PhD thesis, Università degli studi di Napoli "Federico II", 2017, URL: https://cds.cern.ch/record/2268663.

[95] SHiP Collaboration, *Comprehensive design study report*, tech. rep., CERN, 2019, URL: https://cds.cern.ch/record/2704147.

[96] W. M. Bonivento, *Studies for the electro-magnetic calorimeter SplitCal for the SHiP experiment at CERN with shower direction reconstruction capability*, JINST **13** (2018), p. C02041, DOI: 10.1088/1748-0221/13/02/c02041.

[97] SHiP collaboration, *Measurement of associated charm production induced by 400 GeV/c protons*, tech. rep., CERN, 2017, URL: https://cds.cern.ch/record/2286844.

[98] ALICE collaboration, *D-meson production in p-Pb collisions at* $\sqrt{s_{NN}} = 5.02$ *TeV and in pp collisions at* $\sqrt{s} = 7$ *TeV*, Phys. Rev. C **94** (2016), p. 054908, DOI: 10.1103/physrevc.94.054908.

[99] M. V. Garzelli, S. Moch and G. Sigl, *Lepton fluxes from atmospheric charm revisited*, JHEP **10** (2015), p. 115, DOI: 10.1007/jhep10(2015)115.

[100] H. Dijkstra and T. Ruf, *Heavy Flavour Cascade Production in a Beam Dump*, tech. rep., CERN, 2015, URL: https://cds.cern.ch/record/2115534.

[101] SHiP collaboration, *Track reconstruction and matching for SHiP-charm*, tech. rep., CERN, 2021, URL: https://cds.cern.ch/record/2746408.

[102] Y. Gaillard, *Specification technique concernant la refection de l'electro-aimant Goliath*, tech. rep., CERN, 1969, URL: https://edms.cern.ch/document/1326984.

[103] M. Blau and H. Wambacher, *Disintegration Processes by Cosmic Rays with the Simultaneous Emission of Several Heavy Particles*, Nature **140** (1937), p. 585, DOI: 10.1038/140585a0.

[104] C. Powell, P. Fowler and D. Perkinset, *The study of elementary particles by the photographic method*, Pergamon Press, 1959.

[105] R. Acquafredda et al., *The OPERA experiment in the CERN to Gran Sasso neutrino beam*, JINST **4** (2009), P04018, DOI: 10.1088/1748-0221/4/04/p04018.

[106] SND@LHC Collaboration, *SND@LHC: The Scattering and Neutrino Detector at the LHC*, 2022, DOI: 10.48550/ARXIV.2210.02784.

[107] E. Zaffaroni, *SND@LHC - A new Scattering and Neutrino Detector at the LHC*, PoS **ICHEP2022** (2022), p. 1236, DOI: 10.22323/1.414.1236.

[108] T. Nakamura et al., *The OPERA film: New nuclear emulsion for large-scale, high-precision experiments*, Nucl. Instrum. Meth. A **556** (2006), p. 80, DOI: `10.1016/j.nima.2005.08.109`.

[109] C. W. Fabjan and H. Schopper, eds., *Particle Physics Reference Library*, vol. 2: Detectors for Particles and Radiation, Springer International Publishing, 2020, DOI: `10.1007/978-3-030-35318-6`.

[110] T. Tani, *Photographic Science: Advances in Nanoparticles, J-Aggregates, Dye Sensitization, and Organic Devices*, Oxford University Press, 2011, DOI: `10.1093/acprof:oso/9780198714606.001.0001`.

[111] T. Naka et al., *Fine grained nuclear emulsion for higher resolution tracking detector*, Nucl. Instrum. Meth. A **718** (2013), p. 519, DOI: `10.1016/j.nima.2012.11.106`.

[112] L. Arrabito et al., *Track reconstruction in the emulsion-lead target of the OPERA experiment using the ESS microscope*, JINST **2** (2007), P05004, DOI: `10.1088/1748-0221/2/05/p05004`.

[113] K. Morishima et al., *Development of nuclear emulsion for muography*, Annals of Geophysics **60** (2017), S0112, DOI: `10.4401/ag-7387`.

[114] M. Kaplon, B. Peters and D. M. Ritson, *Emulsion Cloud-Chamber Study of a High Energy Interaction in the Cosmic Radiation*, Phys. Rev. Lett. **85** (1952), p. 905, DOI: `10.1103/PhysRev.85.900`.

[115] A. Iuliano, *Event reconstruction and data analysis techniques for the SHiP experiment*, PhD thesis, Università degli studi di Napoli “Federico II", 2021, URL: `https://cds.cern.ch/record/2776128`.

[116] R. Zimmermann et al., *The precision tracker of the OPERA detector*, Nucl. Instrum. Meth. A **555** (2005), p. 435, DOI: `10.1016/j.nima.2005.09.003`.

[117] P. Gorbounov, *DAQ Framework for the 2018 combined beam tests*, tech. rep., CERN, 2017, URL: `https://cds.cern.ch/record/2290076`.

[118] H. Bethe, *Zur Theorie des Durchgangs schneller Korpuskularstrahlen durch Materie*, Ann. Phys. **397** (1930), p. 325, DOI: `10.1002/andp.19303970303`.

[119] F. Bloch, *Bremsvermögen von Atomen mit mehreren Elektronen*, Z. Phys. **81** (1933), p. 363, DOI: `10.1007/bf01344553`.

[120] F. Bloch, *Zur Bremsung rasch bewegter Teilchen beim Durchgang durch Materie*, Ann. Phys. **408** (1933), p. 285, DOI: `10.1002/andp.19334080303`.

[121] S. M. Seltzer and M. J. Berger, *Evaluation of the collision stopping power of elements and compounds for electrons and positrons*, Int. J. Appl. Radiat. Isot. **33** (1982), p. 1189, DOI: 10.1016/0020-708x(82)90244-7.

[122] H. Kolanoski and N. Wermes, *Particle Detectors - Fundamentals and Applications*, Oxford University Press, 2020, DOI: 10.1093/oso/9780198858362.001.0001.

[123] M. Berger et al., *ESTAR, PSTAR, and ASTAR: Computer Programs for Calculating Stopping-Power and Range Tables for Electrons, Protons, and Helium Ions*, online database, Version 2.0.1, 2005, URL: https://physics.nist.gov/PhysRefData/Star/Text/intro.html.

[124] D. E. Groom, N. V. Mokhov and S. I. Striganov, *MUON STOPPING POWER AND RANGE TABLES 10 MeV–100 TeV*, Atomic Data and Nuclear Data Tables **78** (2001), p. 183, DOI: 10.1006/adnd.2001.0861.

[125] Particle Data Group, *Atomic and Nuclear Properties of Materials*, 2021, URL: https://pdg.lbl.gov/2020/AtomicNuclearProperties/.

[126] H. Bichsel, *Straggling in thin silicon detectors*, Rev. Mod. Phys. **60** (1988), p. 663, DOI: 10.1103/revmodphys.60.663.

[127] G. Molière, *Theorie der Streuung schneller geladener Teilchen I Einzelstreuung am abgeschirmten Coulomb-Feld*, Z. Nat. A. **2.3** (1947), p. 134, DOI: 10.1515/zna-1947-0302.

[128] V. L. Highland, *Some practical remarks on multiple scattering*, Nucl. Instrum. Meth. **129** (1975), p. 497, DOI: 10.1016/0029-554x(75)90743-0.

[129] G. R. Lynch and O. I. Dahl, *Approximations to multiple Coulomb scattering*, Nucl. Instrum. Meth. B **58** (1991), p. 6, DOI: 10.1016/0168-583X(91)95671-Y.

[130] C. Leroy and P.-G. Rancoita, *Principles of Radiation Interaction in Matter and Detection*, World Scientific, 2009.

[131] M. J. Berger et al., *XCOM: Photon Cross Sections Database (interactive)*, online database, URL: http://physics.nist.gov/PhysRefData/Xcom/Text/XCOM.html.

[132] S. Sze and K. K. Ng, *Physics of Semiconductor Devices*, John Wiley & Sons, Inc., 2006, DOI: 10.1002/0470068329.

[133] K. Seeger, *Semiconductor Physics*, Springer Berlin Heidelberg, 2004, DOI: 10.1007/978-3-662-09855-4.

[134] Y. Dieter, *Development and Characterisation of Passive CMOS Sensors for Pixel Detectors in High Radiation Environments*, PhD thesis, Universität Bonn, 2022, URL: https://nbn-resolving.org/urn:nbn:de:hbz:5-67787.

[135] F. Scholze et al., *Determination of the electron–hole pair creation energy for semiconductors from the spectral responsivity of photodiodes*, Nucl. Instrum. Meth. A **439** (2000), p. 208, DOI: 10.1016/s0168-9002(99)00937-7.

[136] W. Shockley, *Currents to Conductors Induced by a Moving Point Charge*, J. Appl. Phys. **9** (1938), p. 635, DOI: 10.1063/1.1710367.

[137] S. Ramo, *Currents Induced by Electron Motion*, Proceedings of the IRE **27** (1939), p. 584, DOI: 10.1109/jrproc.1939.228757.

[138] D.-L. Pohl, *3D-Silicon and Passive CMOS Sensors for Pixel Detectors in High Radiation Environments*, PhD thesis, Universität Bonn, 2020, URL: https://nbn-resolving.org/urn:nbn:de:hbz:5-60007.

[139] A. Chilingarov, *Temperature dependence of the current generated in Si bulk*, JINST **8** (2013), P10003, DOI: 10.1088/1748-0221/8/10/p10003.

[140] J. Dingfelder et al., *Progress in DMAPS developments and first tests of the Monopix2 chips in 150 nm LFoundry and 180 nm TowerJazz technology*, Nucl. Instrum. Meth. A **1034** (2022), p. 166747, DOI: 10.1016/j.nima.2022.166747.

[141] ATLAS IBL collaboration, *Prototype ATLAS IBL modules using the FE-I4A front-end readout chip*, JINST **7** (2012), P11010, DOI: 10.1088/1748-0221/7/11/p11010.

[142] D.-L. Pohl, *Overview of the ATLAS Insertable B-Layer (IBL) Project*, PoS **RD13** (2015), p. 012, DOI: 10.22323/1.189.0012.

[143] D.-L. Pohl et al., *Obtaining spectroscopic information with the ATLAS FE-I4 pixel readout chip*, Nucl. Instrum. Meth. A **788** (2015), p. 49, DOI: 10.1016/j.nima.2015.03.067.

[144] P. Ahlburg, *Development of a FE-I4-based module for radiation monitoring with BEAST II during the commissioning phase of the Belle II detector*, masters' thesis, Universität Bonn, 2016, URL: https://docs.belle2.org/record/3256.

[145] M. Benoit et al., *The FE-I4 telescope for particle tracking in testbeam experiments*, JINST **11** (2016), P07003, DOI: 10.1088/1748-0221/11/07/p07003.

[146] I. Jaegle et al., *Compact, directional neutron detectors capable of high-resolution nuclear recoil imaging*, Nucl. Instrum. Meth. A **945** (2019), p. 162296, DOI: 10.1016/j.nima.2019.06.037.

[147] FE-I4 Collaboration, *The FE-I4B Integrated Circuit Guide*, 2012.

[148] L. Rossi et al., *Pixel Detectors From Fundamentals to Applications*, Springer, 2006.

[149] M. Barbero et al., *FE-I4 ATLAS Pixel Chip Design*, PoS **VERTEX 2009** (2010), p. 027, DOI: 10.22323/1.095.0027.

[150] M. Alam et al., *The ATLAS silicon pixel sensors*, Nucl. Instrum. Meth. A **456** (2001), p. 217, DOI: `10.1016/s0168-9002(00)00574-x`.

[151] J. Schwandt, *Design of a Radiation Hard Silicon Pixel Sensor for X-ray Science*, PhD thesis, Universität Hamburg, 2014, URL: `https://bib-pubdb1.desy.de/record/205852/files/desy-thesis-14-029.pdf`.

[152] ATLAS IBL collaboration, *Production and integration of the ATLAS Insertable B-Layer*, JINST **13** (2018), T05008, DOI: `10.1088/1748-0221/13/05/t05008`.

[153] J. Janssen, D.-L. Pohl et al., *pyBAR, versatile readout and test system for the ATLAS FE-I4(A/B) pixel readout chip*, URL: `https://github.com/SiLab-Bonn/pyBAR`.

[154] R. Gurin and A. Maslennikov, *ControlHost: Package for Distributed Data Handling*, URL: `https://www.nikhef.nl/pub/experiments/antares/software/Dispatcher/Marseille-Oct95.ps`.

[155] SiLab, *Software package basil, a modular data acquisition system and system testing framework in Python*, URL: `https://github.com/SiLab-Bonn/basil`.

[156] J. Janssen, N. Owtscharenko and D.-L. Pohl, *pyBAR for SHiP–charm*, URL: `https://github.com/SiLab-Bonn/pyBAR/tree/SHiP-testbeam`.

[157] N. Owtscharenko, *PyControlHost*, 2018, URL: `https://github.com/owtscharenko/PyControlHost`.

[158] SHiP collaboration, *Reconstruction of 400 GeV/c proton interactions with the SHiP-charm project*, CERN (2021), URL: `https://cds.cern.ch/record/2743204`.

[159] F. Wang, B. Nachman and M. Garcia-Sciveres, *Ultimate position resolution of pixel clusters with binary readout for particle tracking*, Nucl. Instrum. Meth. A **899** (2018), p. 10, DOI: `10.1016/j.nima.2018.04.053`.

[160] B. Cumer and K. Nikolitsas, *Measurement of the charm cross section setup on H4 beam line*, tech. rep., CERN, 2018, URL: `https://edms.cern.ch/ui/file/2010858/1/2018.07.27_H4_CHARM.pdf`.

[161] F. James and M. Roos, *Minuit - a system for function minimization and analysis of the parameter errors and correlations*, Comput. Phys. Commun. **10** (1975), p. 343, DOI: `10.1016/0010-4655(75)90039-9`.

[162] R. Brun and F. Rademakers, *ROOT — An object oriented data analysis framework*, Nucl. Instrum. Meth. A **389** (1997), p. 81, DOI: `10.1016/s0168-9002(97)00048-x`.

[163] H. Jansen et al., *Performance of the EUDET-type beam telescopes*, EPJ Techniques and Instrumentation **3** (2016), p. 7, DOI: `10.1140/epjti/s40485-016-0033-2`.

[164] M. Paterno, *Calculating Efficiencies and Their and Uncertainties*, tech. rep., Fermilab, 2004, URL: https://lss.fnal.gov/archive/test-tm/2000/fermilab-tm-2286-cd.pdf.

[165] D. Casadei, *Estimating the selection efficiency*, JINST **7** (2012), P08021, DOI: 10.1088/1748-0221/7/08/p08021.

[166] SHiP collaboration, *Track reconstruction and matching between emulsion and silicon pixel detectors for the SHiP-charm experiment*, JINST **17** (2022), P03013, DOI: 10.1088/1748-0221/17/03/p03013.

[167] A. Bocci and W. Hulsbergen, *TRT alignment for SR1 cosmics and beyond*, tech. rep., CERN, 2007, URL: https://cds.cern.ch/record/1039585/files/indet-pub-2007-009.pdf.

[168] J.-P. Dedieu, *Newton Raphson Method*, *Encyclopedia of Applied and Computational Mathematics*, Springer, 2015, p. 1023, DOI: 10.1007/978-3-540-70529-1_374.

[169] M. Rosenthal et al., *Magnetic Field Measurements of the GOLIATH Magnet in EHN1*, tech. rep., CERN, 2018, URL: https://cds.cern.ch/record/2310483.

[170] C. Bron and J. Kerbosch, *Algorithm 457: finding all cliques of an undirected graph*, Communications of the ACM **16** (1973), p. 575, DOI: 10.1145/362342.362367.

[171] J. Siek, L.-Q. Lee and A. Lumsdane, *The Boost Graph Library (BGL)*, 2001, URL: https://www.boost.org/doc/libs/1_81_0/libs/graph/doc/index.html.

Acknowledgements

Working on, and finally finishing this thesis was a journey which I would not have been able to complete on my own. And so, I would like to thank the people who accompanied me on this way.

First of all my gratitude goes to Markus Cristinziani, who not only asked me to join the SHiP−charm project, but understood asking the right questions at the right time and pushing me when it was necessary. I also would like to thank Markus Risse for approaching this rare topic as second referee.
A good part of the results in this thesis would not have been possible without the knowledge and advice Vadim Kostyukhin provided. Thank you for the enlightening discussions and the unique, very dry way of concluding our findings.
Furthermore, I would like to thank the SHiP−charm collaboration. In particular Antonia Di Crescenzo and Antonio Iuliano for their work on the emulsion detector, and Christopher Betancourt for his work on the track matching. Without your insights and results my work would not have been possible.
Starting my thesis in SiLab and then switching to Siegen, I owe quite some gratitude to both groups. I would like to thank Jochen Dingfelder and Fabian Hügging for keeping me as a guest in SiLab. At the same time I am grateful for the nice welcome I received in Siegen and the very enjoyable working atmosphere.
Without the soft- and firmware written by David and Jens a lot of theses would not have been realised, which is also true for mine. Thank you both for this legacy. I also would like to thank Wolfgang Dietsche for his expertise in module handling and mechanical design.
But working on this thesis was not only about content and results but a great deal about perseverance: In Patrick and Pascal I found true friends, thank you for the support and all the professional and unprofessional time and laughter spent, you kept me going and I could always rely on you. This gratitude extends to Botho, Bruno, Yannick, Jannes, Florian, Christian, Georgios, Lars, Snow, Ivan and the whole rest of the SiLab. The occasional ONE beer was much appreciated.

Aber nicht nur in meinen Arbeitsgruppen, auch privat habe ich viel Unterstützung erfahren, für die ich mindestens ebenso dankbar bin. Da ist zunächst Matek der mich auf seine unnachahmliche Weise motiviert hat und aus eigener Erfahrung weiß, wie anstrengend eine Promotion sein kann. Außerdem natürlich Theo mit seiner entspannten und stets positiven Sicht auf die Dinge. Auch Max und sein Abenteuerspielplatz auf dem ich gerne abschalte, haben mir sehr geholfen meine Gedanken zu ordnen. Und natürlich habe ich meinen Werdegang meiner Familie zu verdanken die mich nicht nur während der Promotion sondern auch sonst immer geduldig unterstützt hat.
Es gibt eine große Zahl an Menschen die hier nicht persönlich erwähnt sind, denen ich aber dennoch unfassbar dankbar bin für ein von Zeit zu Zeit offenes Ohr oder eine gelegentliche Ablenkung.

Zum Schluss möchte ich Chrissi danken, die mit mir auch durch die stressigsten Zeiten gegangen ist – ohne dich wäre ich sicher nicht so weit gekommen.